Linear and Nonlinear Optical Microscopy of Layered Materials at Nanoscale

Dissertation

der Mathematisch-Naturwissenschaftlichen Fakultät

der Eberhard Karls Universität Tübingen

zur Erlangung des Grades eines

Doktors der Naturwissenschaften

(Dr. rer. nat.)

vorgelegt von

Lin Pan

aus Fujian/China

Tübingen

2022

Gedruckt mit Genehmigung der Mathematisch-Naturwissenschaftlichen Fakultät der Eberhard Karls Universität Tübingen.

Tag der mündlichen Qualifikation:	14.03.2023
Dekan:	Prof. Dr. Thilo Stehle
1. Berichterstatterin:	Assoc. Prof. Dr. Elizabeth Boer-Duchemin
2. Berichterstatter:	Prof. Dr. Christoph J. Brabec

Abstract

Optical characterization techniques as ultrasensitive and nondestructive tools, in revealing the influence of local structure on optical properties of two-dimensional semiconducting layers, have emerged widespread attention. In this thesis, nonlinear optical microscopy accompanied by Raman microscopy are used to characterize and understand the structural properties of layered materials, such as structural irregularities, crystalline orientation, and structural symmetry as well as molecular orientation.

Initially, by using confocal scanning optical microscopy coupled with a femtosecond pulsed laser, an efficient second-harmonic generation (SHG) emission at the flake edges of monolayer tungsten disulfide (WS_2) is clearly observed, which is due to the presence of broken translational symmetry and more structural defects at the edges. Interestingly, the room-temperature two-photon induced photoluminescence (2PPL) response shows as the weakest at the flake edges, which exhibits an anticorrelation with SHG signal in the monolayer WS_2. The obtained results are likely due to the presence of mid-gap electronic states between the valence and conduction bands at the flake edges. In addition, the SHG intensity increases with increasing flake thickness; whilst the 2PPL optical signal is only visible in monolayer WS_2. The polarization-dependent SHG signal exhibits a six-fold rotational pattern, indicating the three-fold rotational symmetry of WS_2 flake.

Subsequently, the structural irregularities properties of atomically thin molybdenum diselenide ($MoSe_2$) flakes are further investigated by SHG and 2PPL signals. The 2PPL peaks located at ~2.30 eV and ~2.38 eV could be assigned to the A’ exciton and B’ exciton transitions of $MoSe_2$ flake, respectively.

The crystal orientations of discrete $MoSe_2$ flakes are determined by using the polarized SHG imaging and the angular-dependent SHG spectroscopy. We observed the differences in the angle 3θ which is defined as the angle between the generated SH electric field and the laser electric field, which experimentally indicates the different crystal orientations of discrete $MoSe_2$ flakes. Moreover, the bright SHG signal at the grain boundaries and edges is clearly visualized within an individual $MoSe_2$ flake.

The utilization of confocal microscopy combined with higher order laser modes, Raman enhancement on $MoSe_2$ flake by using copper phthalocyanine (CuPc) molecules as Raman probe, is demonstrated. Both the photoluminescence and SHG spectroscopies are used to reveal the local structural properties of the $MoSe_2$ flake. The Raman enhancement on $MoSe_2$ monolayer at an azimuthally polarized excitation is stronger than the enhancement at a radially polarized excitation. This result indicates that the face-on oriented CuPc molecules can strongly interact with the $MoSe_2$ monolayer through the ground-state charge-transfer process and the dipole-dipole interaction. Furthermore, the Raman scattering maps on the irregular $MoSe_2$ surface show a good correlation with the SHG and PL images, suggesting the relationship between local structure and optical properties of $MoSe_2$ flake.

Eventually, k-space imaging microscopy, in probing the angular emission patterns is implemented based on the confocal microscopy coupled with a femtosecond pulsed laser. The sample location- and thickness-dependent emission patterns of 2PPL signals emanating from single-crystal DH-P-TTA molecule films are demonstrated. Combined with calculated emission pattern, the possible molecular orientation within DH-P-TTA film has been discussed. Two 2PPL peak maxima located at ~516 nm and ~552 nm are distinguished on the film. We observe the anisotropic emission pattern on the ultrathin film, which suggests the molecules adopt a tilt angle and show a high degree of ordering

within one domain. Moreover, close correlation between the generated 2PPL signal and the layer thickness of DH-P-TTA film is also demonstrated. The almost isotropic radiative patterns are visualized on the thick films with a thickness of ~33.0 nm and ~58.18 nm, which is attributed to the vertical orientation of DH-P-TTA molecules in the films.

Content

General introduction

Two-dimensional semiconducting layers, *i.e.,* transition metal dichalcogenides (TMDCs) and organic molecule films have drawn increasing attention for the next generation optoelectronic and electrochemical devices.[1, 2] Many interesting phenomena can be observed in the semiconducting layers, mainly due to the presence of their structure properties such as structural defects, molecular orientation, and structural ordering.[3-7] These structural effects have been considered as the crucial parameters influencing their optical and electrical properties. For example, mirror twin boundaries in monolayer TMDCs induce the photoluminescence quenching and increase the in-plane electrical conductivity, whereas tilt boundaries lead to strong photoluminescence enhancement and decrease the conductivity.[8] In addition, due to the high structural ordering and the vertical molecular orientation with respect to the substrate plane, the single-crystal organic films can offer the advantage of enhanced charge carrier transport in the field-effect transistors, which was proved to be an excellent candidate in these applications.[9] Considerable works have been done to develop characterization methods in order to investigate the structural properties, including transmission electron microscopy, scanning probe microscopies, and X-ray techniques.[8, 10-14] However, these techniques have been limited by the potential damage on the samples, mainly due to the physical contact and the strong radiation of probe beams.[15]

Optical characterization techniques have become the sophisticated, ultrasensitive, and nondestructive tools applied in the field of nanoscience and nanotechnology,[16] thanks to the development of the laser technology and photon detector.[17] An abundant set of information such as structural defect, structural symmetry, crystal orientation, and molecular orientation, can be

provided by using optical spectroscopic and microscopic characterizations.[18-20] Linear optical characterization techniques such as photoluminescence (PL) and Raman microscopies have intensively been used to investigate the structural defect-related properties of TMDCs materials.[21-26] More recently, the observations of nonlinear optical effects such as second harmonic generation (SHG),[27-29] two-photon induced photoluminescence (2PPL),[30-32] and third harmonic generation,[33] in the semiconducting layers start to garner increasing attention. In particular, SHG process is sensitive to the structural symmetry of materials, which is forbidden in a material with inversion symmetry.[34] Thereby, SHG microscopy becomes a powerful method in characterizing the structural irregularities properties of TMDCs materials.[18, 27] In addition, k-space imaging microscopy is a class of optical microscopy, which is able to understand the emissive transition dipole orientation by probing the angular emission patterns from optical materials.[35-39]

In this thesis the home-built confocal scanning optical microscopy assisted with a parabolic mirror is used to characterize and understand the structural properties dependency of linear and nonlinear optical properties of two-dimensional semiconducting layers. The layered materials contain TMDCs flakes, and ultrathin molecule films. The structural characterizations of layered materials are preliminarily conducted with bright-field optical microscope together with atomic force microscopy (AFM). Firstly, by using the confocal microscopy coupled with a femtosecond pulsed laser, we are allowed to unravel the structure properties, *i.e.,* structural irregularities, structural symmetry, and crystal orientation, of TMDCs flakes by nonlinear optics. Subsequently, combined with higher-order laser modes, the influence of local structural properties at the surface of TMDCs flake on Raman enhancement using copper phthalocyanines (CuPc) as the probe molecule is revealed. Finally, k-space imaging microscopy is implemented based on the confocal microscopy for understanding the sample location- and film thickness-dependent angular

emission patterns on thin molecule films.

The thesis contains six chapters as follows:

Chapter 1 presents the basic theory. Theoretical foundations of nonlinear optical processes of SHG and 2PPL in two-dimensional semiconducting materials, surface-enhanced Raman scattering (SERS), and radiation properties of single dipole will be briefly given in this chapter.

Chapter 2 describes the relevant optical techniques. The details of home-built confocal scanning optical microscopy used in SHG, 2PPL, PL, Raman, and angular emission pattern measurements will be presented. In addition, the optical characterizations of several plasmonic systems are presented here. The layered materials and general sample characterization methods are introduced as well.

Chapter 3 reveals the edge defect on tungsten disulfide (WS_2) flake by SHG and 2PPL emissions. The nature of WS_2 monolayer is determined by AFM technique and Raman spectroscopy. The structural inhomogeneities on WS_2 monolayer are probed by SHG and 2PPL microscopies. The dependency of SHG and 2PPL responses on the layer thickness of WS_2 flake is also represented.

Chapter 4 describes the crystal orientation and grain boundaries on molybdenum diselenide ($MoSe_2$) flake. Performing polarized SHG imaging and spectroscopy measurements, the crystal orientations of discrete $MoSe_2$ flakes are determined. Grain boundaries and edges with an individual $MoSe_2$ flake are revealed by SHG emission.

Chapter 5 demonstrates the local structural properties at the surface of $MoSe_2$ flake. The triangular $MoSe_2$ flake in this chapter is used as an active SERS platform. The dependency of the Raman enhancement on laser beam

polarization and local structure using CuPc molecule as Raman probe is demonstrated.

Chapter 6 shows the results of directional emission on DH-P-TTA thin molecule film. The sample location- and layer thickness-dependent 2PPL emissive directionality are presented in this chapter. Combined with the calculated emission pattern, the molecular orientation within DH-P-TTA thin film will be proposed.

Chapter 1 Theoretical foundations

Theoretical foundations of nonlinear optical processes in two-dimensional semiconducting materials, Raman scattering and related enhancement mechanisms, and radiation properties of a single dipole are briefly given.

1.1 Nonlinear optical processes

For understanding the linear and nonlinear optical processes, the interaction between an electromagnetic wave and matter should be considered. In the linear regime, the interaction of the electric field E of laser light with matter is described by the equation as follows:

$$P_l = \varepsilon_0 \chi^{(1)} E \tag{1.1}$$

Here, the induced polarization is described by P_l. The permittivity of free space is represented by ε_0. The quantity $\chi^{(1)}$ represents the linear susceptibility.

When the intense light interacts with the medium, the optical nonlinearity effect can be triggered. The intense light source can be provided by an ultrafast pulsed laser. To precisely describe the optical nonlinearity, the induced polarization P_{nl} of medium depends on the applied electric field E that is expressed by the relationship as follows:[40]

$$P_{nl} = \varepsilon_0 \left(\chi^{(2)} E^2 + \chi^{(3)} E^3 + \cdots \right) \tag{1.2}$$

Here, the quantities $\chi^{(2)}$ and $\chi^{(3)}$ are the second- and third-order nonlinear optical susceptibilities, respectively. The most effects come from second- and third-order interactions. The quantity $\chi^{(2)}$ leads to the investigation studied involving second-harmonic generation (SHG), sum-frequency generation, and

difference-frequency generation. Even more possibilities are due to third-order. The quantity $\chi^{(3)}$ is responsible for the third-harmonic generation, and two-photon induced photoluminescence (2PPL). In addition, Kerr effect arises from third-order effect as well, which is described in the equation as follows:[41]

$$\varepsilon = \varepsilon_0\left[\chi^{(1)} + 3\chi^{(3)}|E|^2\right] \tag{1.3}$$

which shows that the permittivity of material ε is dependent on the electric field intensity $|E|$.

Because of the invention of laser technology and photon detector, the nonlinear optical effects involving SHG and 2PPL processes were experimentally observed. In later sections, the theoretical foundations of SHG and 2PPL in transition metal dichalcogenides (TMDCs) materials will be introduced.

1.1.1 Second-harmonic generation

The SHG microscopy and spectroscopy techniques have become a considerable subject in the structural characterizations of TMDCs materials. The SHG process was first demonstrated by Franken et al in 1961.[42] Figure 1.1 exhibits an SHG process, where two incident photons at the optical frequency ω provided by an ultrafast pulsed laser are mediated by the two virtual states, and then two photons are converted into one emitted photon at the optical frequency of $\omega_{SHG} = 2\omega$.[43] SHG belongs to a second-order nonlinear coherent scattering process, which originates from the induced polarization instead of photons absorption. The second-order nonlinear induced polarization $P_{SHG}^{(2)}(2\omega_1)$ is written as follows:[44]

$$P_{SHG}^{(2)}(2\omega_1) = \varepsilon_0\chi^{(2)}E_1E_1 \tag{1.4}$$

Here, the second-order susceptibility tensor is represented by $\chi^{(2)}$, which is responsible for SHG process.

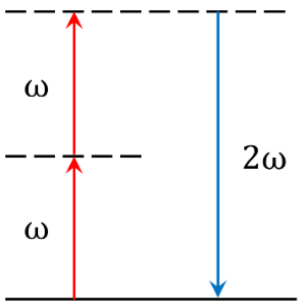

Figure 1.1: Energy level diagram of second-harmonic generation (SHG) process.

The black solid line denotes the ground state, and the dashed line represents the virtual state. The red arrow denotes the incident excitation light at frequency ω, and the blue arrow represents the radiation at the second-harmonic frequency 2ω.

The nonlinear susceptibilities are tensorial quantities, which are sensitive to the material symmetry, leading to the structural investigations by nonlinear optics.[41] We consider the special case of SHG process in a medium with inversion symmetry. In this case the sign of the induced polarization $P_{SHG}^{(2)}(2\omega_1)$ must change when we change the sign of the electric field E_1 of laser light. Here the equation (1.4) can be replaced as follows:

$$-P_{SHG}^{(2)}(2\omega_1) = \varepsilon_0 \chi^{(2)}[-E_1][-E_1] \tag{1.5}$$

which exhibits that

$$-P_{SHG}^{(2)}(2\omega_1) = \varepsilon_0 \chi^{(2)} E_1 E_1 \tag{1.6}$$

With a comparison of the equation (1.6) with the equation (1.4), it is found that $P_{SHG}^{(2)}(2\omega_1) = -P_{SHG}^{(2)}(2\omega_1)$ is required, which suggests the second-order susceptibility must be $\chi^{(2)} = 0$. Consequently, the generation of SHG signal is forbidden in materials with inversion symmetry. Nevertheless, SHG process can occur as well at the surface or edges of the centrosymmetric material such as gold, and aluminum nanoparticles, because the presence of an interface can break the inversion symmetry at the region.[40]

In addition, it is essential to satisfy the phase-matching condition $\Delta k = k_{2\omega} - 2k_{\omega} = 0$ for the generation of SHG, as illustrated in Figure 1.2. Otherwise, the SHG signals would be weak or even vanish. Herein the wave vector is represented by k. According to quantum mechanics, the phase-matching condition requires that the energy and momentum of the photon should be simultaneously conserved in the nonlinear optical process.[45] However, the phase-matching condition is not important when the size of the nonlinear source is shorter than the wavelength. Due to the atomic thin feature, the phase-matching condition can be ignored in TMDCs materials.

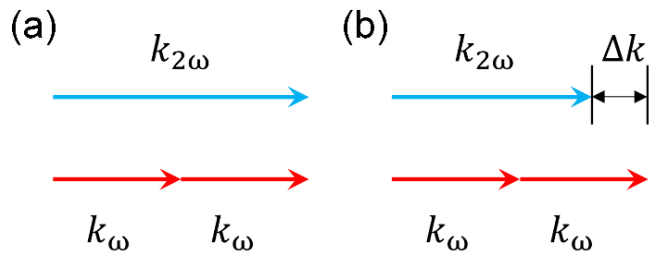

Figure 1.2: Schematic drawing of phase-matching condition.
(a) Perfect phase matching. (b) Wave-vector mismatch.

TMDCs materials with general formula MX_2, where M represents the transition metals (*e.g.,* W, and Mo), and X is the chalcogen atom (*e.g.,* S, and Se), which are representative systems of two-dimensional semiconductors.[46, 47] The structure of MX_2 is illustrated in Figure 1.3, a metal atom M is coordinated with six chalcogen atoms via a covalent bond. Within a monolayer MX_2, metal atom M is arranged in a hexagonal order to form a metal layer that is sandwiched by two chalcogen layers. Through the van der Waals force between the neighboring monolayers, the multilayers or bulk crystal MX_2 can be formed. The crystal lattice of TMDCs monolayer in the hexagonal 2H-phase belongs to the trigonal prismatic (D_{3h}) point group, which means that it is a non-centrosymmetric material.[18] The SHG process is the lowest-order nonlinear optical process for TMDCs monolayer.

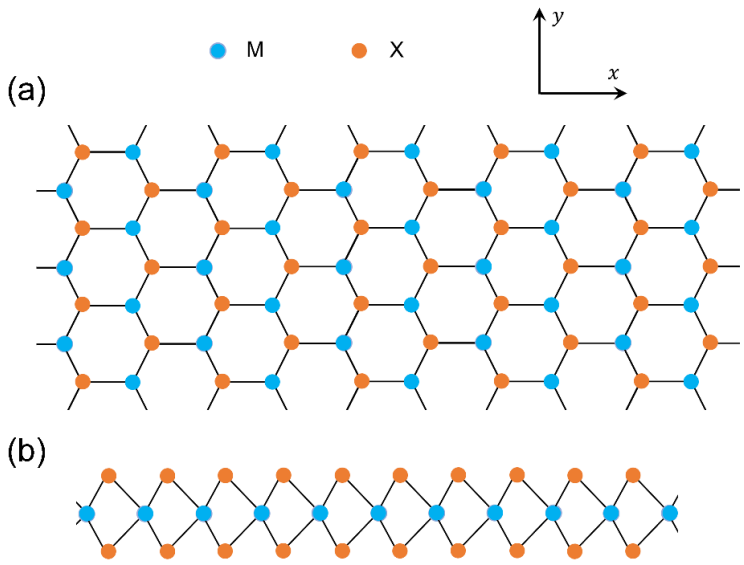

Figure 1.3: Schematic representation of atomic structure of MX_2 monolayer. (a) Top view. (b) Side view. M represents a metal atom, and X denotes a chalcogen atom.

Considering the MX_2 monolayer with the D_{3h} point group symmetry, the second-order susceptibility tensor has only four nonvanishing elements with one free parameter as follows:[48]

$$\chi^{(2)} = \chi^{(2)}_{xxx} = -\chi^{(2)}_{xyy} = -\chi^{(2)}_{yxy} = -\chi^{(2)}_{yyx} \tag{1.7}$$

Here, x is the armchair direction, and y is the zigzag direction, as shown in Figure 1.3.

In the case of an incident light polarization parallel (vertical) to the transmission direction of analyzer, the dependency of generated SHG electric field $E(2\omega)$ as a function of the sample orientation can be written as follows:[49]

$$E_{\parallel}(2\omega) = C\chi^{(2)}\cos(3\theta) \tag{1.8}$$

$$E_{\perp}(2\omega) = C\chi^{(2)}\sin(3\theta) \tag{1.9}$$

Here, C is a proportionality constant, θ denote the angle between the armchair direction in the crystal structure and the polarization direction of incident light.

Based on the equations (1.8) and (1.9), the SHG intensity as a function of the sample orientation can be written as follows:[28]

$$I_{\parallel} = I_0 \cos^2(3\theta) \tag{1.10}$$

$$I_{\perp} = I_0 \sin^2(3\theta) \tag{1.11}$$

Here, I_0 denotes the maximum intensity of generated SHG. From the expression (1.10), the maxima of the observed SHG intensity coincide with the armchair directions in the crystal structure, which allows to determine the crystal orientation of TMDCs materials.

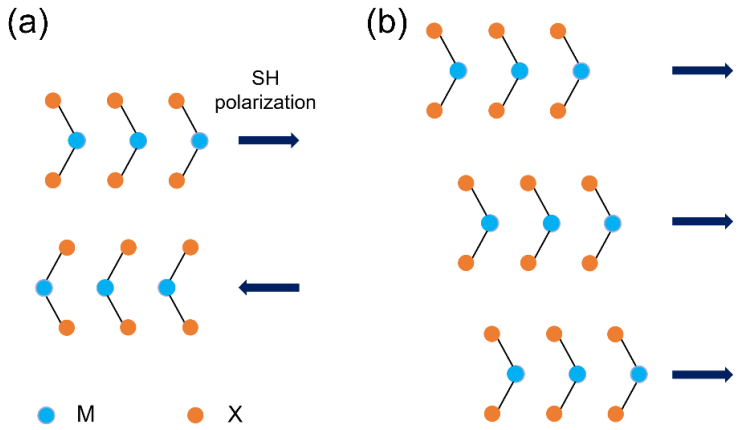

Figure 1.4: The side view of crystal structure of the hexagonal 2H-phase and the rhombohedral 3R-phase MX_2.

(a) exhibits the mirrored orientation of each layer and anti-parallel orientation of second-harmonic (SH) dipole. (b) shows the same orientation of neighboring layers and parallel orientation of SH dipole. M represents a metal atom, and X denotes a chalcogen atom.

TMDCs materials normally have two polytypes, *i.e.,* hexagonal 2H-phase, and rhombohedral 3R-phase.[50] The schematic diagrams of crystal structures of 2H-phase and 3R-phase TMDCs materials are illustrated in Figure 1.4(a) and (b), respectively. For the 2H-phase TMDCs multilayer or bulk, the flakes with even-numbered layers are centrosymmetric, where the neighboring layers show the flipped orientation and anti-parallel second-harmonic (SH) dipoles. On the

contrary, the 3R-phase TMDCs multilayer or bulk belong to the C_{3v} point group symmetry, and individual layer is determined to be the 2H-phase.[51] The adjacent layers of 3R-phase flakes are oriented in parallel but shift along the in-plane direction, which leads to the constructive interference of the SH polarization.

1.1.2 Two-photon induced photoluminescence

2PPL signal from Eu(Ⅱ) ions in CaF_2:Eu excited by Maiman's ruby laser was first experimentally observed by Kaiser and Garret in 1961, and the 2PPL intensity is proportional to the square of the laser intensity.[52] Figure 1.5 exhibits a schematic drawing of the 2PPL process, a third-order nonlinear optical phenomenon that contains the simultaneous absorption of two photons at the same frequency ω via a virtual state (called two-photon absorption), the fast relaxation of the excited electron to the thermal equilibrium stage, and finally the radiative recombination of an electron in the emitting state with a hole in the ground state in terms of photoluminescence (PL).

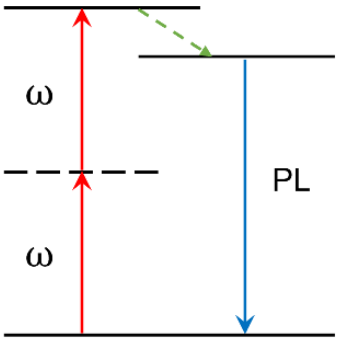

Figure 1.5: Energy level diagram of two-photon induced photoluminescence (2PPL) process.

The black solid line denotes the ground or excited states, and the dashed line represents the virtual states. The red arrow denotes the two-photon absorption process, the green arrow shows the fast relaxation process, and the blue arrow represents the radiative emission (photoluminescence, PL).

Two-photon absorption process is described by using two-photon absorption coefficient α_2. The relationship between the irradiance I of the applied laser and the absorption coefficient is expressed as follows:[53]

$$\frac{dI}{dz} = -\alpha_1 I - \alpha_2 I^2 - \alpha_3 I^3 \cdots \quad (1.12)$$

Here, $\frac{dI}{dz}$ represents the attenuation of the irradiance I through an isotropic matter in the z axis. One-photon (linear) and three-photon absorption coefficients are represented by α_1 and α_3, respectively. If only nonlinear absorption process occurs under the irradiation of a very intense light that can be provided by a femtosecond pulsed laser, the equation (1.12) can be approximated to the second term, which demonstrates that the two-photon absorption process is proportional to the square of the irradiance I.

TMDCs semiconductors, as potential optoelectronic devices, exhibit an interesting transformation from indirect band gap to direct band gap when scaled down to the monolayer limit.[47] Recently, two-photon effects, *e.g.,* two-photon absorption saturable, and 2PPL emission, in TMDCs semiconductors have been experimentally observed.[29-32, 54] Ye et al reported that the 2PPL spectroscopic technique is used for revealing the excitonic dark states in tungsten disulfide (WS_2) monolayer in 2014, which is not able to be determined through the single-photon photoluminescence spectroscopy.[55] Under two-photon excitation, electrons can migrate from the valence band maximum (VBM) to the excitonic dark states with odd parity, as illustrated in the two-photon absorption process of Figure 1.6(a). One-photon absorption in WS_2 monolayer, however, only can reach the excitonic states with even parity. They performed the optical measurement of 2PPL and PL signals as a function of the excitation laser energy ranging from 2.05 eV to 2.6 eV in WS_2 monolayer at a sample temperature of 10 K, as shown in Figure 1.6(b). Regarding the 2PPL curve, two excitonic dark states at 2.28 eV and 2.48 eV are labeled respectively as the $2p$ and $3p$ states. The A exciton ($1s$ state) and its trion in WS_2 monolayer induce

two one-photon absorptions at 2.04 eV and 2 eV, respectively, as shown in the green curve of Figure 1.6(b).

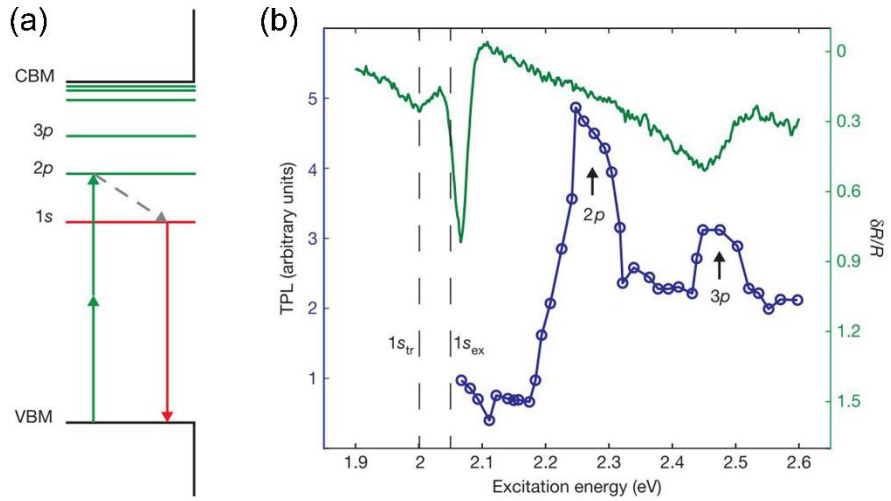

Figure 1.6: Revealing the dark exciton states of tungsten disulfide (WS_2) monolayer by 2PPL process. Adapted from Ye et al.[55]

(a) Schematic drawing of the 2PPL process in WS_2 monolayer. CBM and VBM denote the conduction band minimum and the valence band maximum, respectively. (b) The blue and green curves represent respectively the two-photon absorption and one-photon absorption spectra obtained from WS_2 monolayer at a sample temperature of 10 K.

1.2 Surface-enhanced Raman scattering

In 1928, the experimental observation of Raman scattering coming from molecules was first found by Raman and Krishnan.[56] After that, the Raman spectroscopies have attracted extensive attention, mainly thanks to a variety of their applications in chemical sensing, materials characterization, and medical imaging.[57] However, the spontaneous Raman scattering is extremely weak because one Raman photon is generated for every $10^6 - 10^8$ incident photons, which becomes the main obstacle against the practical applications of Raman spectroscopies.[58, 59] To overcome this issue, much effort has been paid attention to develop the enhanced Raman spectroscopic techniques. These techniques contain resonance Raman scattering, coherent anti-Stokes Raman

scattering, surface-enhanced hyper Raman scattering, and surface- and tip-enhanced Raman scattering spectroscopies.[57, 60-62] The phenomenon of surface-enhanced Raman scattering (SERS) was first observed and interpreted in 1974 by Fleischmann et al, who experimentally investigated the two possible types of pyridine adsorption on the surface of a roughened silver electrode.[63] In general, the SERS effect is about the amplification of Raman signals coming from molecules by many orders of magnitude. In later sections, the theoretical foundations of Raman scattering and Raman enhancement mechanism in terms of electromagnetic enhancement and chemical enhancement will be briefly introduced.

1.2.1 Raman scattering

The various optical events can be triggered when the laser light interacts with matter. These events contain absorption, emission, and scattering, which are related to the transitions with the electronic, vibrational, and rotational states of the medium. The scattering processes are in terms of elastic scattering and inelastic scattering. The vibrational Raman scattering originally comes from the inelastic light scattering by molecules or materials, where the scattered photon energy E_S is not equal to the incident photon energy E_I.[64] The insight of chemical structure of molecules can be provided by investigating the Raman spectrum. Figure 1.7(a) shows an energy level diagram illustrating the Stokes Raman scattering, which requires the relationship as follows:

$$E_S = E_I - \hbar\omega_{vib} \tag{1.13}$$

The anti-Stokes Raman scattering processes, as shown in Figure 1.7(b), requires the relationship as follows:

$$E_S = E_I + \hbar\omega_{vib} \tag{1.14}$$

The Raman shifts are expressed in wave-numbers and denoted by $\Delta\bar{\nu}_R$, which

is calculated by $\Delta\bar{\nu}_R = \hbar\omega_{vib}/hc$, where h is Planck's constant, and c is the speed of light. Furthermore, the effect of Raman scattering becomes intense when the incident photon energy matches with the electronic energy of the molecule, which is called resonance Raman scattering (RRS) as illustrated in Figure 1.7(c).

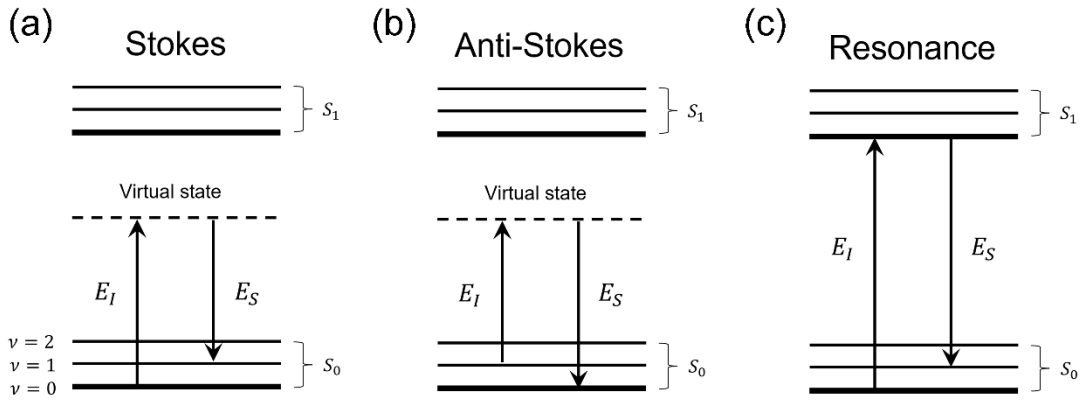

Figure 1.7: Energy level diagrams of (a) Stokes Raman, (b) anti-Stokes Raman, and (c) resonance Raman scattering processes.

The incident photon energy and scattered photon energy are represented by E_I and E_S, respectively. The dashed line denotes the virtual state, and the black solid line denotes the real electronic state.

1.2.2 Enhancement mechanism

In general, the SERS effect results from the enhancement of Raman scattering from molecules adsorbed at the surface of SERS substrates such as metal nanoparticles, rough metal surfaces, graphene, and TMDCs materials.[65-71] Two main effects including electromagnetic mechanism and chemical mechanism, give rise to the SERS effect. Electromagnetic mechanism is usually linked to the localized surface plasmon resonance (LSPR) effect that is driven by the interaction of light with metal nanoparticles, and chemical mechanism relates to the so-called charge-transfer process between the SERS substrates and the adsorbed molecules.

Figure 1.8 shows a schematic diagram of localized surface plasmons. Light interacts with metal nanospheres, where the size of metal nanosphere is much smaller than the wavelength of incident light. This leads to that the conduction electrons of a metal nanosphere are in collective oscillations, which is known as LSPR.[72]

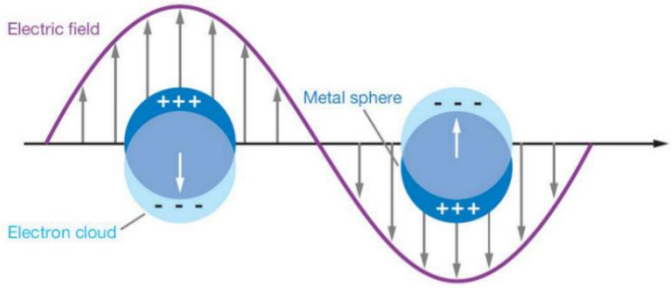

Figure 1.8: Schematic diagram of localized surface plasmons. Adapted from Willets et al.[72]

Due to the metal nanospheres to concentrate light into small volumes, the electric field in these volumes can become very strong, which leads to the formation of hot spots in the vicinity of the metal nanospheres. Thereby, by placing a molecule in the hot spots, the SERS enhancement factor in terms of electromagnetic mechanism is expressed as follows:[73]

$$G_{SERS} = \sigma(\omega_{inc})\sigma(\omega_{inc} - \omega_{vib}) \quad (1.15)$$

Here, the local electric field enhancement is represented by $\sigma = |E_{loc}|^2/|E_{inc}|^2$ at the incident frequency ω_{inc}, and at the Stokes Raman-shifted frequency $\omega_{inc} - \omega_{vib}$. If ω_{inc} and $\omega_{inc} - \omega_{vib}$ are close to each other, the SERS enhancement factor G_{SERS} can show a fourth dependence on the local electric field E_{loc}. In addition, when both the incident radiation at ω_{inc} and the Stokes Raman-shifted radiation at $\omega_{inc} - \omega_{vib}$ are in good resonance with the plasmon peak of the metal nanosphere, the optimal SERS enhancement can be obtained.[74]

In terms of the chemical enhancement mechanism, it corresponds to any modification of the Raman polarizability of the adsorbed molecules onto the SERS substrates.[75] At the beginning of 1980s, two distinct charge-transfer processes including the excited-state charge-transfer and ground-state charge-transfer processes, were pointed out by Frank J. Adrian[76] and Max E. Lippitsch.[77] The main difference between two charge-transfer processes is the excitation wavelength dependence.

Figure 1.9(a) shows a schematic diagram of excited-state charge-transfer process, where the electrons can migrate from the metal conduction bands to the LUMO of the molecule. The charge-transfer process is mainly due to the formation of a complex between the metal and the molecule via chemical bonding, where the electronic structure of the whole system is changed.[64] The optimal Raman enhancement is obtained when the difference between the Fermi level of the metal and the LUMO energy of the molecule matched the laser excitation wavelength.

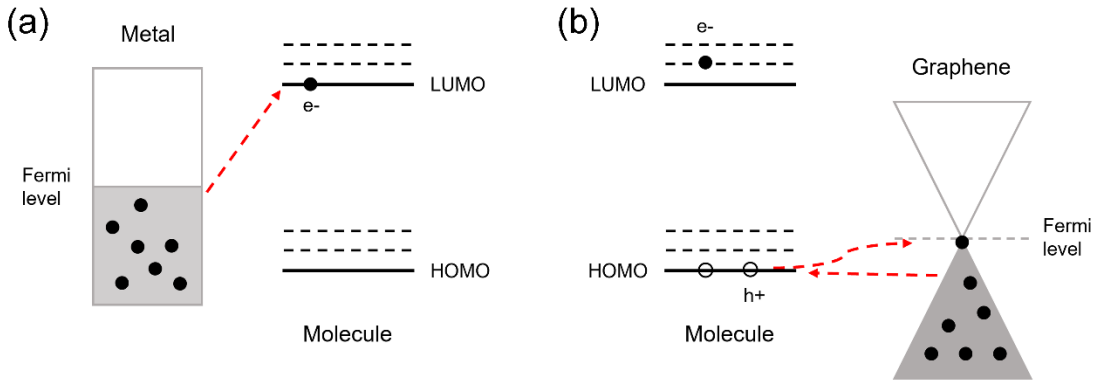

Figure 1.9: Schematic diagrams of two distinct charge-transfer process models. Inspired by Frank J. Adrian and Ling et al.[66, 76]

(a) Excited-state charge-transfer process between metal nanostructure and molecule; (b) Ground-state charge-transfer process between graphene and molecule. The dashed red arrows indicate the charge-transfer process. LUMO and HOMO denote the lowest unoccupied molecular orbital and highest occupied molecular orbital, respectively.

Figure 1.9(b) exhibits a schematic diagram of ground-state charge-transfer process which occurs between the graphene and the molecule in the ground state. The charge-transfer complex between the graphene and the molecule is not required for the Raman enhancement. When the laser excitation wavelength matches the electronic bandgap of the molecule, the maximum Raman enhancement is obtained.[77] Due to the abundant π electrons on the graphene surface and the continuous energy band of graphene, the charge-transfer process can easily occur between the graphene and molecule, where the electrons of graphene can be involved in the Raman scattering process of molecules, further leading to the Raman enhancement of molecules.[66]

The important feature of the chemical enhancement mechanism is the short-range effect. To predict the distance dependence of Raman enhancement factor $G(d)$, a simple model based on spherical-particle resonance is expressed as follows:[78, 79]

$$G(d) = G(d = 0) * (a/(a + d))^{10} \quad (1.16)$$

Here, the local radius curvature is represented by a. The quantity d denotes the distance of the Raman probe from the surface of metal particle. From the expression it is concluded that Raman enhancement factor $G(d)$ shows a decay as d^{10}.

In 1981, the concept of first-layer effect was proposed by Moskovits,[80] who points out that the Raman signals of the first adsorbed monolayer on colloidal silver particles are more enhanced when compared to the subsequent monolayers. The Raman enhancement is due to the coupling of molecular vibration with the surface plasma mode via the charge-transfer process from the adsorbed molecule to the metal nanoparticle. After that, much attention was paid to investigate the first-layer effect.[78, 81-83] For example, Eesley investigated the coverage dependence of Raman enhancement of pyridine molecule on Ag,

where the Raman scattering exhibits the saturation after the first adsorbed layer.[81] In addition, the probe molecule-silver separation dependence of Raman enhancement was studied by Murray et al,[82] who figured out that a giant Raman enhancement factor up to 10^6 is obtained when the Raman scatters contact the rough silver with no polymer spacer. In a nutshell, Raman enhancement through the chemical mechanism can be pronounced when the molecules directly contact the substrate surface.

1.3 Radiation properties of a single dipole

The various photophysical properties, *e.g.,* emission intensity, and lifetime of emitting state, of an individual molecule are sensitively dependent on the orientation of emission-dipole moment of the molecule.[84] In the past, the three-dimensional orientation of the emission-dipole moment had been determined by several methods such as the polarization analysis of the fluorescence signals, and visualization of the defocused fluorescence image.[36, 85, 86] Recently, a promising approach, by placing a photon detector at the back focal plane of the objective for imaging the angular emission pattern, has become an interesting hot spot for determining the emission-dipole orientation.[87]

In a free space, a single dipole shows a non-isotropic radiation pattern. The three-dimensional patterns of an individual dipole with three different orientations are shown in Figure 1.10. The orientation of an individual dipole is expressed by a spherical coordinates $P(\Phi, \Theta)$, as illustrated in Figure 1.10(b). The optical axis is defined along the direction of z-axis. According to the model of a Hertzian dipole, single dipole in a free space can emit the highest intensity into the angles perpendicular to the dipole moment, as shown in Figure 1.10.

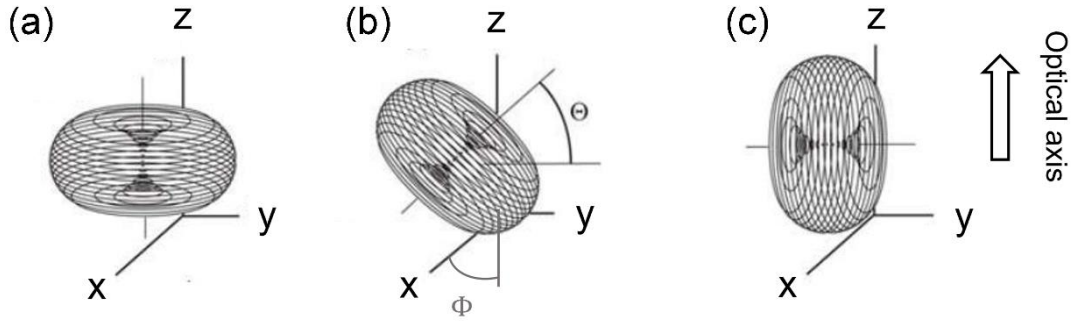

Figure 1.10: Three-dimensional radiation pattern of a single dipole. The optical axis is defined along z-axis. Adapted from Brokmann et al.[88]

(a) $\Phi = 0°$, $\Theta = 90°$ (out-of-plane dipole). (b) $\Phi = 0°$, $\Theta = 45°$. (c) $\Phi = 0°$, $\Theta = 0°$ (in-plane dipole).

To calculate the distribution of optical intensities $I(r, \phi, \Phi, \Theta)$ of a single molecule on the surface of glass substrate in the back focal plane of the objective, Lieb et al pointed out an approach based on the Weyl representation as follows:[87, 89]

$$I(r, \phi, \Phi, \Theta) \propto \frac{1}{\cos\theta}\left(E_p E_p^* + E_s E_s^*\right) \tag{1.17}$$

Figure 1.11 exhibits the schematic drawing for the calculation of the intensities distribution of a single dipole. The r represents the radial distance from the optical axis, and the angle ϕ is the in-plane angle in the back focal plane. The angle θ represents the emitting photon at the angle with respect to the optical axis. It should be noted that $r/f = \sin\theta$, where f is the focal length. The dipole orientation is defined by one in-plane angle Φ, and another out-of-plane angle Θ. The E_p, and E_p^* represent the p-polarized components of the electric field and the corresponding complex conjugate; whilst the E_s, and E_s^* denote the s-polarized components of the electric field and the corresponding complex conjugate.

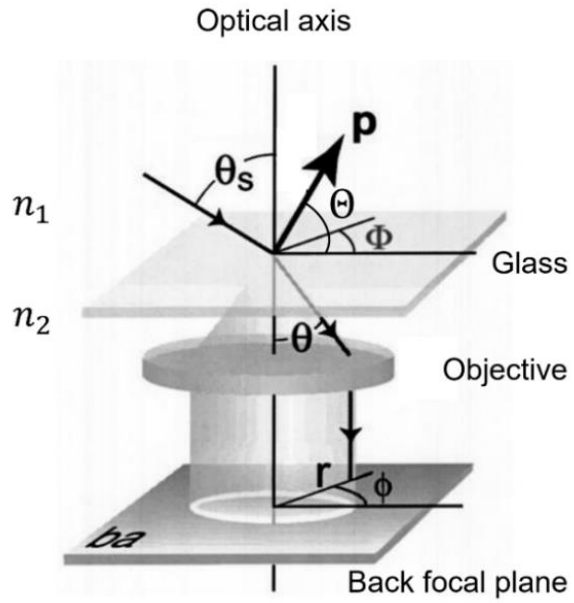

Figure 1.11: Schematic drawing for the calculation of the intensities distribution. Adapted from Lieb et al.[87]

P: dipole moment. The emitting dipole is placed above the interface with the refractive indices n_1 and n_2. The dipole orientation is expressed by one in-plane angle Φ and another out-of-plane angle Θ.

The complete expressions for E_p, and E_s are given as follows:

$$E_p = [c_1(\theta)\sin\Theta\sin\theta + c_2(\theta)\cos\Theta\cos\theta\cos(\phi - \Phi)] \quad (1.18)$$

$$E_s = c_3(\theta)\cos\Theta\sin(\phi - \Phi) \quad (1.19)$$

The expressions of $c_1(\theta)$, $c_2(\theta)$, and $c_3(\theta)$ are written as below:

$$c_1(\theta) = n^2\frac{\cos\theta}{\cos\theta_s}t^p(\theta_s)\prod(\theta_s) \quad (1.20)$$

$$c_2(\theta) = nt^p(\theta_s)\prod(\theta_s) \quad (1.21)$$

$$c_3(\theta) = -n\frac{\cos\theta}{\cos\theta_s}t^s(\theta_s)\prod(\theta_s) \quad (1.22)$$

with $$\prod(\theta_s) = \exp[ikn_1\cos(\theta_s)\delta]$$

Here, the relative index n is calculated by comparing the refractive index n_2 with the refractive index n_1. k denotes the wave vector in a vacuum. δ

represents the distance between the location of emitting dipole and the interface.

The t^p, and t^s are the Fresnel transmission coefficients for respective p- and s-polarized light, which can be expressed by:[90]

$$t^p(\theta_s) = \frac{2n_1 \cos\theta_s}{n_1 \cos\theta + n_2 \cos\theta_s} \tag{1.23}$$

$$t^s(\theta_s) = \frac{2n_1 \cos\theta_s}{n_1 \cos\theta_s + n_2 \cos\theta} \tag{1.24}$$

According to Snell's law, the relationship between the incident angle θ_s and the emission angle θ is written as below:[91]

$$\theta_s = \arcsin\left(\frac{n_2 \sin\theta}{n_1}\right) \tag{1.25}$$

The calculated emission patterns of a dipole emitter with three different orientations are exhibited in Figure 1.12. The emitter is placed at the interface with the refractive indices n_{air} and n_{glass}. The distinct differences in the three emission patterns allow us to easily distinguish the dipole orientation. Specifically, Figure 1.12(a) shows the emission pattern of a dipole emitter that is vertically oriented to the substrate plane, where a homogeneous distribution of radiative intensity is observed. In Figure 1.12(b), when the dipole is tilted $45°$ with respect to the substrate plane, the emission pattern is clearly anisotropic. Figure 1.12(c) displays the emission pattern of a dipole that is oriented in-plane of the substrate surface, where two lopes is clearly observed. The emission pattern is separated by an outer region and an inner region. The boundary between the two regions is defined to be the critical angle $\theta_{cri} = \arcsin(1/n_{glass})$ at the air-glass interface, which is due to the effect of total internal reflection. The inner region is called as the forbidden region. The maximum collected angle is limited by the numerical aperture $\mathrm{NA} = n \sin\theta_{max}$ of the objective lens.

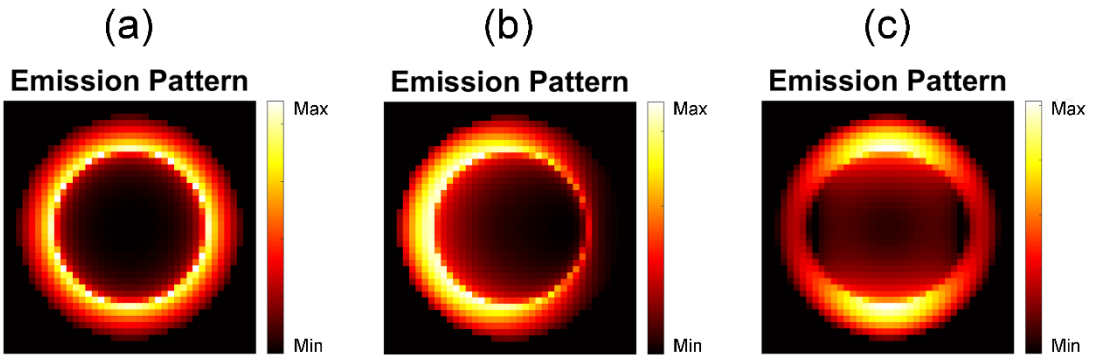

Figure 1.12: Calculated emission patterns of a single dipole with three different orientations. The dipole is placed at the air-glass interface ($n_{air} = 1.0,\ n_{glass} = 1.52$) in the back focal plane of objective lens with a numerical aperture (NA) up to 1.46. The color bars represent the optical intensity.

(a) $\Phi = 0°,\ \Theta = 90°$ (out-of-plane dipole). (b) $\Phi = 0°,\ \Theta = 45°$. (c) $\Phi = 0°,\ \Theta = 0°$ (in-plane dipole).

Chapter 2 Methods and materials

In this chapter the confocal scanning optical microscopies used for the SHG, 2PPL, Raman, and PL as well as angular emission pattern measurements, are introduced in detail. In addition, the optical characterizations of several plasmonic systems are presented here. The layered materials and general sample characterization methods are introduced as well.

2.1 Confocal scanning optical microscopy

All of the optical measurements in this work are performed at a home-built confocal scanning optical microscopy. Benefitting from no chromatic aberration and high numerical aperture (NA) up to 0.9986 in air,[92-94] a parabolic mirror is used as the optical element for a tight laser focusing and efficient emission signal collection. The optical SHG and 2PPL measurements are conducted with a 780 nm femtosecond pulsed laser. The Raman scattering and PL signals are measured with either a 532 nm or a 636 nm continuous-wave (CW) laser. Furthermore, to investigate the directional emission properties of optical materials, k-space (momentum-space) imaging microscopy has been implemented into the confocal microscopy.

2.1.1 SHG and 2PPL measurements

The schematic drawing of the confocal microscopy is illustrated in Figure 2.1. In the excitation beam path, a new laser, an ultrafast erbium fiber laser (pro NIR_02508, Toptica Photonic) with an excitation wavelength of 780 nm (repetition frequency of 40 MHz, and pulse duration of 89.9 fs), is integrated into the microscopy. The laser beam is purified via a 650 nm long pass filter and

expanded via two telescopes (T1 and T2). The size of the expanded laser beam should match the dimension of the parabolic mirror (diameter: 2 cm). To obtain a homogeneous Gaussian mode, undesired polarization and scattered light are filtered out by using a 15 µm spatial filter positioned at the focus of the telescope 2 (T2). The laser beam is reflected via a 50:50 non-polarizing multiphoton short-pass dichroic beam splitter towards the parabolic mirror. Then, the laser beam is focused down to a diffraction-limited light spot onto the sample by the parabolic mirror. The sample is fixed on the home-built sample holder that is placed on a XYZ piezo scanner (P-517K008, Physik Instrumente). The optical signals are collimated and collected by the parabolic mirror and then pass through the beam splitter.

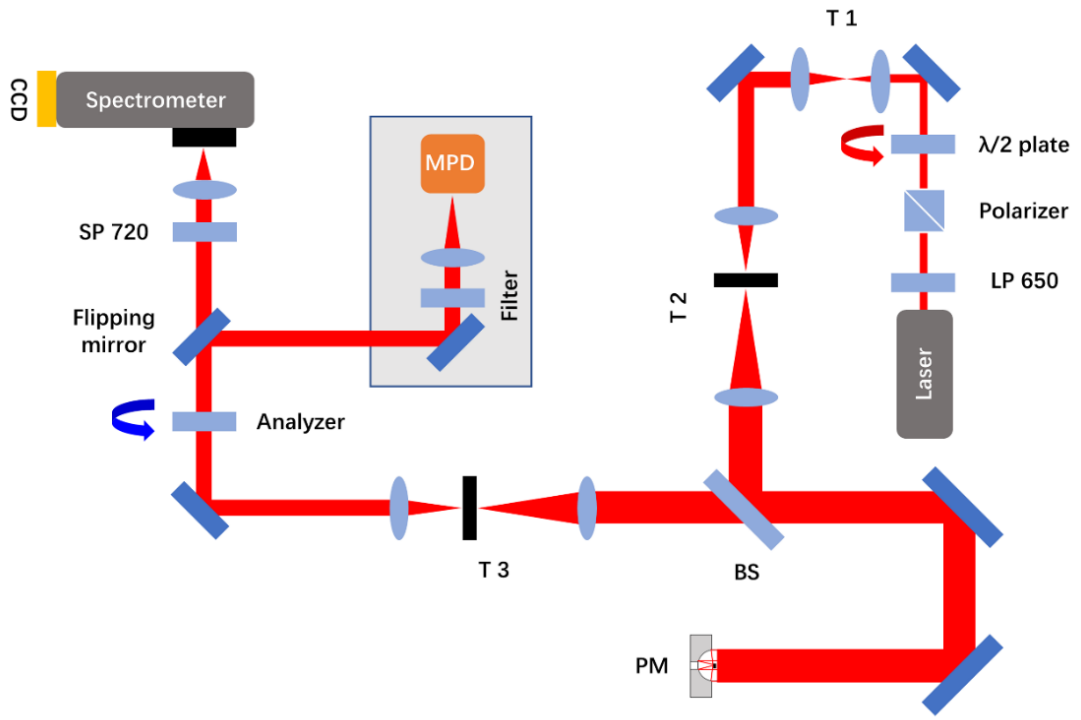

Figure 2.1: Schematic drawing of home-built parabolic mirror-assisted confocal scanning optical microscopy.

PM: Parabolic mirror; λ/2 plate: Lambda half-wave plate; BS: 50:50 Non-polarizing beam splitter; T 1, 2 and 3: Telescope 1, 2 and 3; LP 650: Long pass filter 650 nm; SP 720: Short pass filter 720 nm; MPD: Micro-photon diodes; CCD: Charge-coupled device. A femtosecond pulsed laser with an excitation wavelength of 780 nm is integrated into the confocal microscopy.

In the detection beam path, the size of laser beam is decreased by the telescope 3 (T3). A spatial filter in T3 is used to filter out the scattered light. With a flipping mirror, the optical signals can be directed towards either a spectrometer coupled with a thermoelectrically cooled charge coupled device (CCD) camera (Acton SP 2500, Princeton Instruments) or a micro-photon diodes (MPD, MPD-PD-100-CTD, Micro Photon Diodes Srl). The detection window is ranging from 375 nm to 700 nm. The optical signals are purified by a 720 nm short-pass filter before entering the spectrometer for spectral collection. To obtain the SHG image, a 10 nm band pass filter is placed in front of MPD (seen in Figure 2.1). To obtain the 2PPL image, a 488 nm long pass filter and a 680 nm short pass filter are used to filter out the SHG signal and elastic scattered light.

To perform the polarization-dependent optical measurements, three polarization optics elements are integrated into the optical beam path. In the excitation beam path, a Glan-Taylor polarizer is directly mounted after the laser source to obtain a high-quality linearly polarized laser mode. The laser beam then passes through a lambda half-wave plate, where the linear polarization can be freely turned by 360° by rotating the half-wave plate. In the detection beam path, another Glan-Taylor analyzer is integrated into the beam path, which is able to analyze the polarization of the emission signal. Figure 2.2(a) shows the optical spectrum of the pulsed laser with the peak maximum at ~780 nm. The polar plot of polarization dependency of the laser intensity spectrally integrated from 750 nm to 800 nm is shown in Figure 2.2(b), which is analyzed by rotating the Glan-Taylor analyzer. The polar plot of laser intensity clearly indicates the incident laser is indeed linearly polarized.

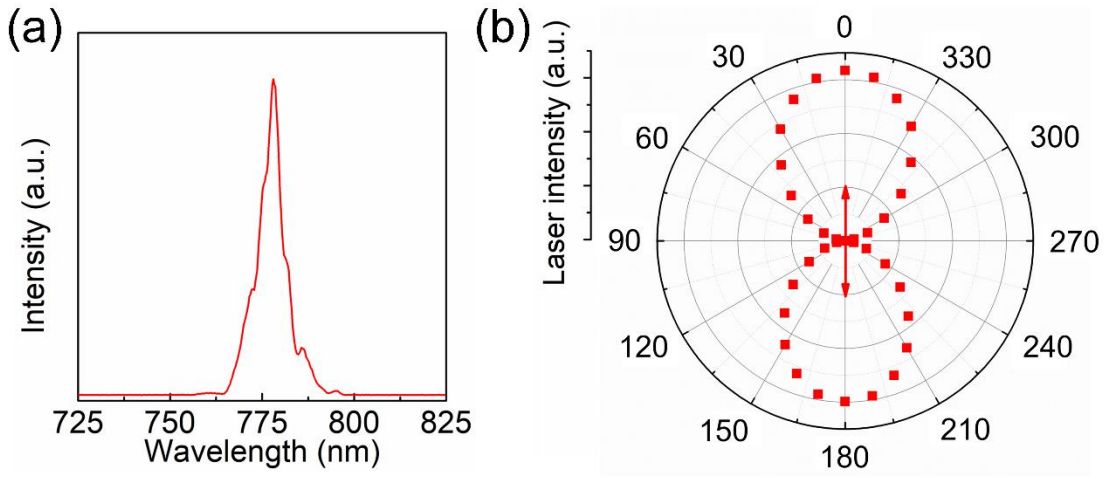

Figure 2.2: (a) The laser light spectrum. The maximum of the peak locates at ~780 nm. (b) The polar plot for the polarization-dependent laser intensity spectrally integrated from 750 nm to 800 nm. The double-ended red arrow in (b) indicates the polarization direction of the laser light.

In the following optical experiment, two polarization optical elements involving a half-wave plate and an analyzer are used simultaneously in the polarization-dependent optical measurements as shown in Figure 2.1. The sample orientation is fixed on the sample holder during the optical measurements. In the measurements, the polarization of incident light is altered as a step of $10°$ by rotating a half-wave plate as a step of $5°$, and the emitting signal of the parallel component is collected, where the transmission axis of the analyzer is oriented parallel to the polarization direction of the incoming light.

To characterize the function of the rebuilt microscopy, well-defined silicon nanorings are measured by using a linearly polarized laser beam. The silicon substrate is exposed under the helium ion beam, where the silicon nanorings can be created. The sample fabrication and scanning electron microscope (SEM) characterization of silicon nanorings is done by the former master student Tim Parker. Figure 2.3(a) shows the nonlinear optical image of six silicon nanorings. The distance between the silicon nanorings can be well resolved. The SEM image of six silicon nanorings is exhibited in the inset of Figure 2.3(d). As the size of silicon nanoring is smaller than the diffraction limit,

an Airy disc can be clearly seen in Figure 2.3(b). Notably, the Airy rings are not visible due to the two-photon induced nonlinear optical process. Shown in Figure 2.3(c), the experimental data is the average of eight cross sections taken from the optical image of Figure 2.3(b). The red curve in Figure 2.3(c) represents the Gaussian fit. The full width at half maximum (FWHM) is roughly 300 nm. The optical spectrum of a single silicon nanoring is shown in Figure 2.3(d). It is clearly observed a broad 2PPL signal and also a narrow SHG peak located at 390 nm.

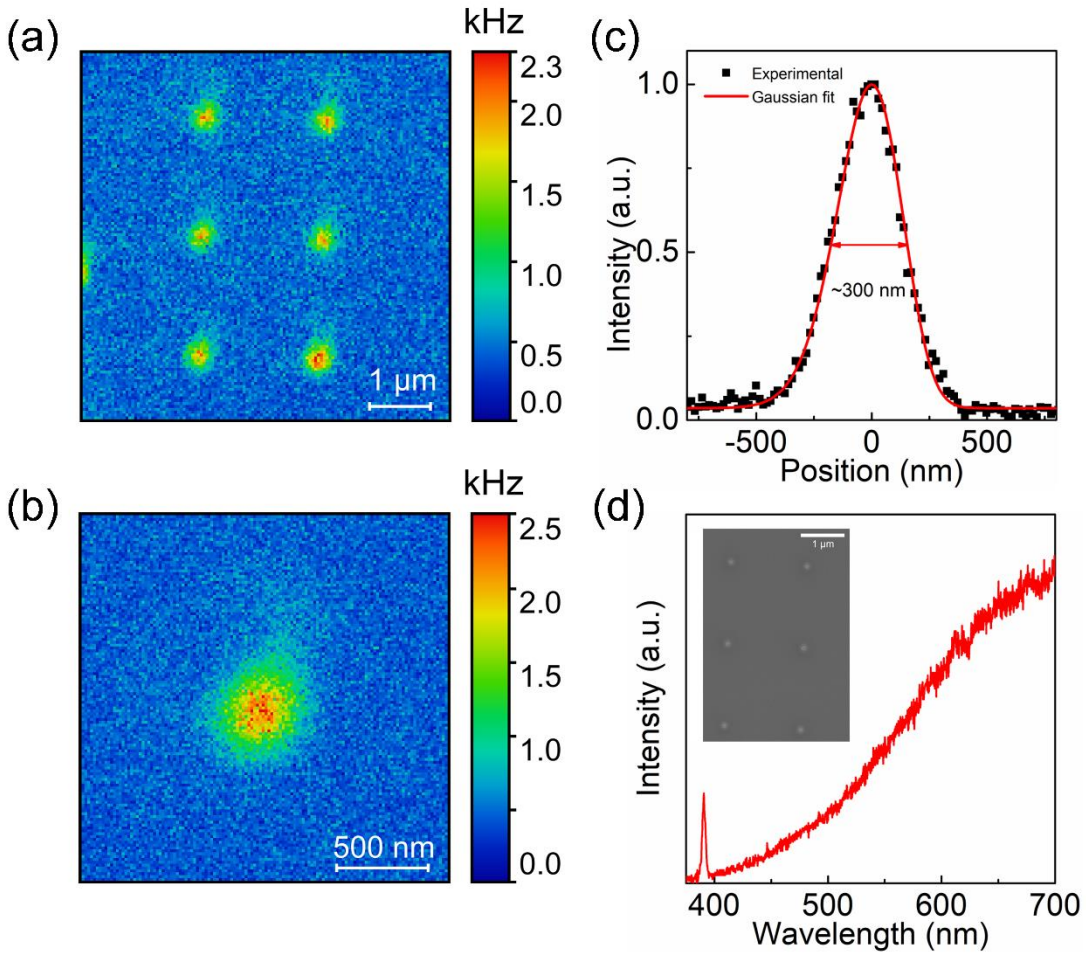

Figure 2.3: (a) Nonlinear optical image of six silicon nanorings excited by a gaussian laser mode. (b) Nonlinear optical image of single silicon nanoring. (c) The intensity distribution across the optical pattern from a single silicon nanoring shown in (b). The experimental data (black points) are averaged from eight cross sections. (d) The optical spectrum obtained from the silicon nanoring. The inset in (d) is the SEM image of the six silicon nanorings.

In addition, single Au nano-discs are measured by using a linearly polarized laser beam. Arrays of Au nano-discs are prepared on an ITO-covered glass substrate using electron-beam lithography, which is fabricated by Dr. Anne-Laure Baudrion from Laboratory Light, Nanomaterials, and Nanotechnology of University of Technology of Troyes. Figure 2.4(a) shows the nonlinear optical image of a single Au nano-disc with a diameter of 80 nm and a height of 50 nm. An Airy disc can be clearly observed, which is due to the size of Au nano-disc being smaller than the diffraction limit. Figure 2.4(b) shows the optical spectra of single Au nano-discs with different diameters. The sharp peaks at 390 nm are the SHG signals, which are dominantly due to the broken centrosymmetry at the Au nano-disc surface, further leading to the surface SHG. Notably, the metallic photoluminescence (MPL) property of single Au nano-disc is sensitively related to its dimension, as shown in Figure 2.4(b). It was reported that MPL contains two emission channels: the electron-hole pair recombination and the plasmons.[95] The plasmons are generated by the d-hole Auger scattering in the nonradiative decay of electron-hole recombination.[96] In this work, the shift in MPL peak is attributed to the radiative decay through the plasmons channel.

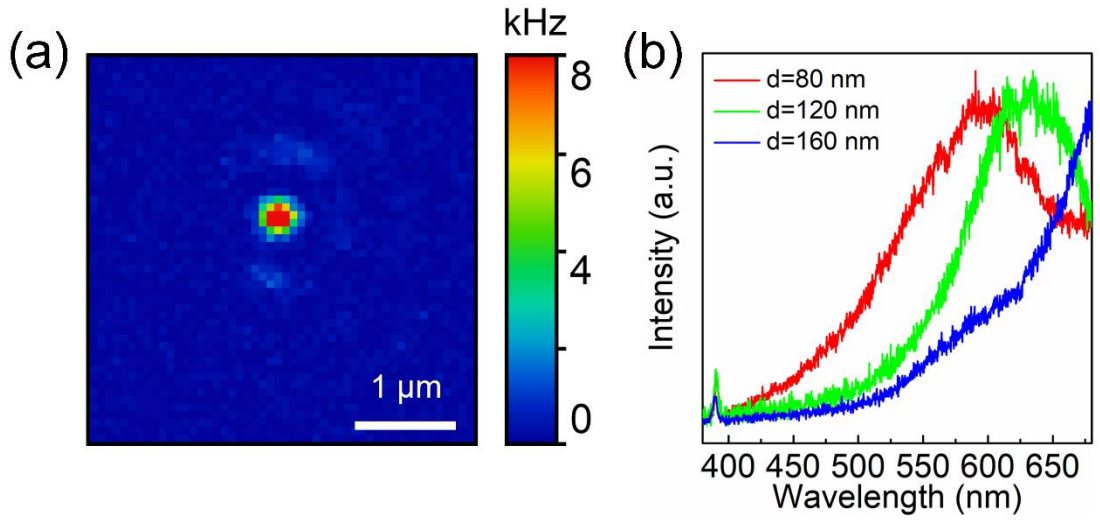

Figure 2.4: (a) Nonlinear optical image of a single Au nano-disc with a diameter of 80 nm. (b) The optical spectra obtained from single Au nano-discs with different diameters (80 nm, 120 nm, and 160 nm).

2.1.2 Raman and PL measurements

The Raman and PL measurements are also conducted with the parabolic mirror-assisted confocal scanning optical microscopy. The optical configuration of this microscopy is similar to the one shown in Figure 2.1. In this microscope, either a 532 nm diode laser (NANO 250-532 max, QIOPTIQ) or a 636 nm diode laser (PDL 800-D, Picoquant) operated under a CW mode is coupled to the microscopy. The laser beam is purified via a band pass filter which is directly placed after the output of the laser. The elastically scattered light is filtered out by using a combination of two notch filters that are positioned in front of the detectors. With a remote flipping mirror, the optical signals can be detected by either an avalanche photodiode (APD, SPCM-AQR-14, Perkin Elmer) for obtaining the optical image or a spectrometer coupled with a liquid nitrogen cooled CCD camera (Acton Research, SpectraPro 300i, Perkin Elmer) for the collection of optical spectra.

Higher-order laser modes namely azimuthally, and radially polarized doughnut modes are used in the excitation polarization dependence measurements. The sketch of the mode conversion is illustrated in Figure 2.5(a). The dashed line represents the optical axis of the beam path. The Gaussian mode laser beam can be converted to either azimuthally or radially polarized modes via the mode converter. The laser beam is expanded with one telescope involving two achromatic doublet lenses. The magnification of laser beam should be considered in order to fulfill the aperture of the parabolic mirror. To ideally generate an azimuthal or a radial mode, other undesired modes and scattering light will be removed by positioning a pinhole at the position of light focus. Figure 2.5(b) shows the mode conversion with a home-made mode converter (MC). The white arrows labeled in azimuthal, radial, and Gaussian modes indicate the light polarization direction. The mode converter contains four quarters of half-wave plates. The fast axis (white line) is differently arranged,[97] as shown in

Figure 2.5(b). The randomly scattered light from the borders of half-wave plates can be filtered out by the pinhole. Rotating the mode converter by $90°$, the generated laser mode can be switched from the radial mode to azimuthal mode. The program “PMCalc” by M. Sackrow, a modified program “Focused Fields” developed by M. A. Lieb and A. J. Meixner, is used to calculate the electric field intensity distribution in the laser focus.

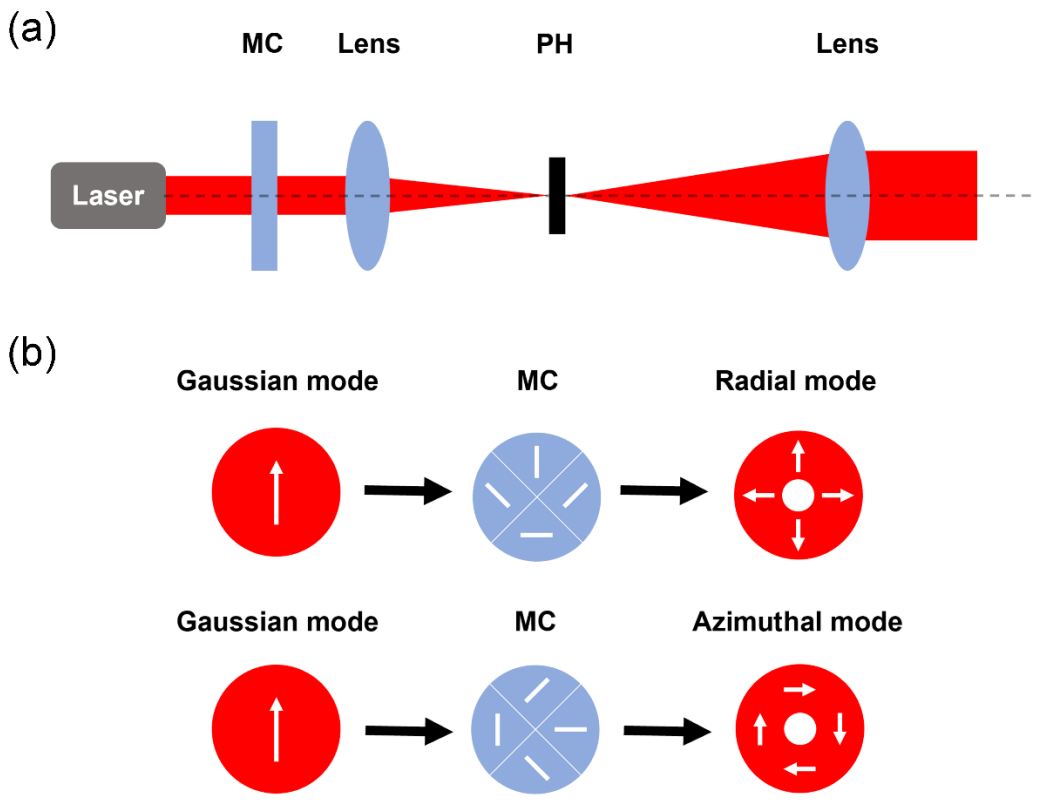

Figure 2.5: (a) Schematic drawing of the optical beam path for a mode conversion from the Gaussian mode to the higher-order laser mode. MC: Mode converter; PH: Pinhole. The dashed line in (a) indicates the optical axis of the beam path. (b) Radial and azimuthal modes generated from the Gaussian mode with a mode converter. The mode converter is made of four quarters of half-wave plates. The white lines marked in the MC represent the fast axis of half-wave plate. The white arrows indicate the light polarization direction.

Using a nanostructured Au on Si substrate as an SERS platform, the dependency of the Raman enhancement on laser beam polarization and excitation wavelength using cobalt phthalocyanine (CoPc) film as a probe are

investigated. Arrays of Au nano-discs are fabricated on the top of Au film with a thickness of 50 nm using electron-beam lithography. The single nano-disc is 80 nm in diameter and 20 nm in height, and the center-to-center interparticle distance is 200 nm. A CoPc thin film with a thickness of 2 nm is deposited on the nanostructured Au through thermal vapor deposition. The used sample is provided by Dr. Diana Davila Pineda, and Prof. Raul D. Rodriguez from IBM Research Nanocenter Operations, IBM Research, Switzerland, and Tomsk Polytechnic University, Russia, respectively. Figure 2.6(a) and (b) show the confocal optical images of CoPc on nanostructured Au excited by a 532 nm diode laser that is radially and azimuthally polarized, respectively. The rectangular bright areas (size: 30 μm × 30 μm) can be seen in Figure 2.6(a) and (b), which are the arrays of Au nano-discs. The Au nano-disc array and the Au film can be distinguished by the clear optical contrast. Individual Au nano-discs with an interparticle distance of 200 nm are not resolved, which is due to the diffraction-limited optical resolution. Moreover, the optical response obtained with the radial polarization is stronger than that with the azimuthal polarization. Figure 2.6(c) and (d) show the Raman spectra of CoPc on nanostructured Au with 532 nm excitation and 636 nm excitation, respectively. The symbol “on” indicates the Raman spectra collected at the rectangular areas (Au nano-disc array); whilst “off” denotes the positions outside the rectangular areas (Au film). It is seen that the Raman intensity at the “on” positions is stronger than that at the “off” positions, which agrees with the optical contrast as shown in Figure 2.6(a) and (b). The Raman scattering of CoPc on nanostructured Au depends on the excitation wavelength, where the Raman signal at 636 nm excitation is higher than that at 532 nm excitation, which is due to the CoPc molecular absorption in good resonance with the laser excitation at a wavelength of 636 nm. Furthermore, we also observed that the Raman signal obtained with the radial polarization is stronger than that with the azimuthal polarization, which is independent of the excitation wavelength.

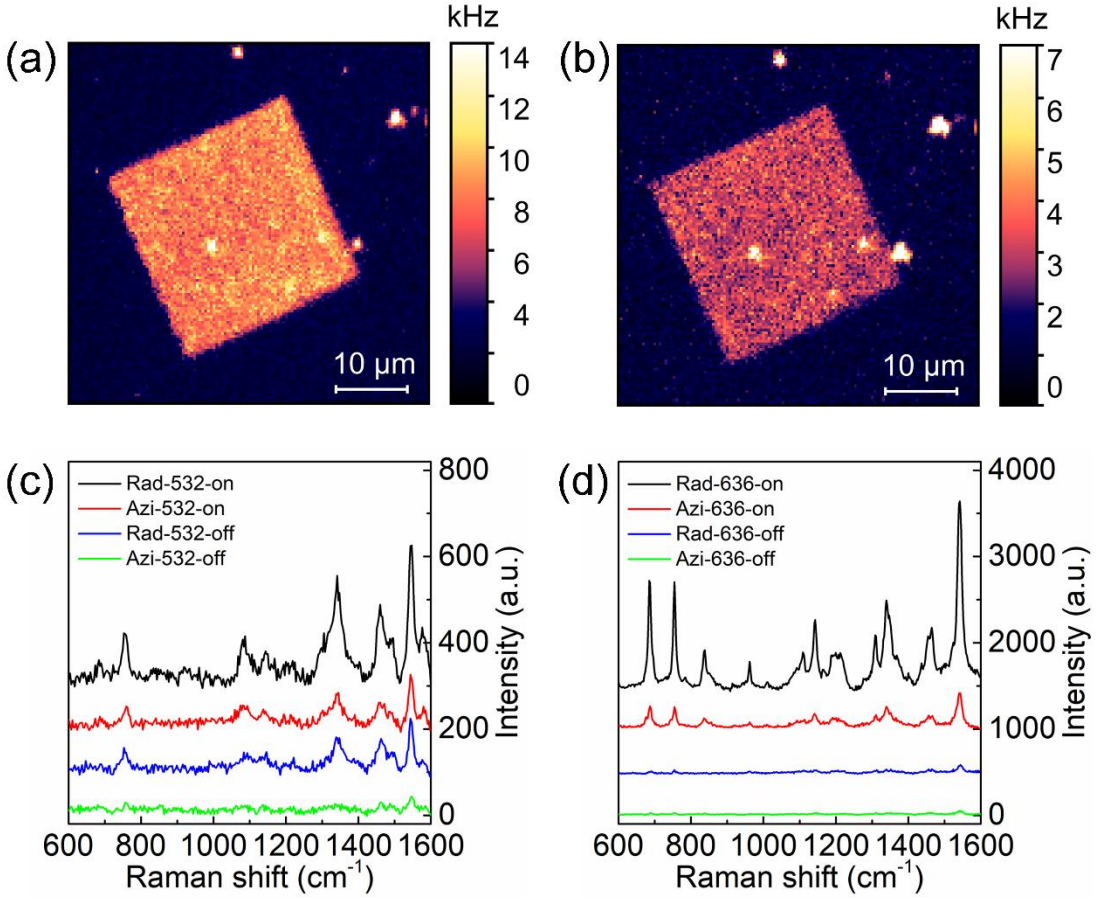

Figure 2.6: (a) and (b) show the confocal optical images of CoPc on nanostructured Au obtained with the radial and azimuthal polarizations, respectively. The confocal optical images are obtained using 532 nm excitation. (c) and (d) show the Raman spectra of CoPc on nanostructured Au using 532 nm and 636 nm excitation, respectively. “Rad” and “Azi” denote the radial and azimuthal polarizations, respectively. “on” and “off” indicate the spectra measured from the rectangular bright areas and outside, respectively. The background of each Raman spectrum was subtracted.

The results have been published:

Yu-Ting Chen, Lin Pan, Anke Horneber, Marius van den Berg, Peng Miao, Ping Xu, Pierre-Michel Adam, Alfred J. Meixner, Dai Zhang. Charge transfer and electromagnetic enhancement processes revealed in the SERS and TERS of a CoPc thin film. *Nanophotonics* **2019,** 8, 1533-1546.

2.1.3 Emission pattern measurements

The schematic drawing for the angular emission pattern imaging is illustrated in Figure 2.7. The k-space imaging microscopy is implemented into the confocal scanning optical microscopy that has been introduced in section 2.1.1. The incoming laser beam (780 nm, fs-pulsed laser) is focused onto the sample by the parabolic mirror and emissions (marked by red and blue lines) are collected and also collimated by the same parabolic mirror, as shown in Figure 2.7. The collimated beam is focused by the lens 1, and the image plane (IP) is created at the distance of f1 (the focal length of lens 1). The emission pattern can be generated with the lens 2, which projects the Fourier transform of the IP. The electron-multiplying charge-coupled device (EMCCD, Andor, iXon Ultra 888) is placed at the position of the focal plane of lens 2. The short pass filter is directly mounted in front of the detector for removing the laser scattered light. Thus, directional inelastic pattern can be projected through the relay of lens 1 and lens 2 at the EMCCD.

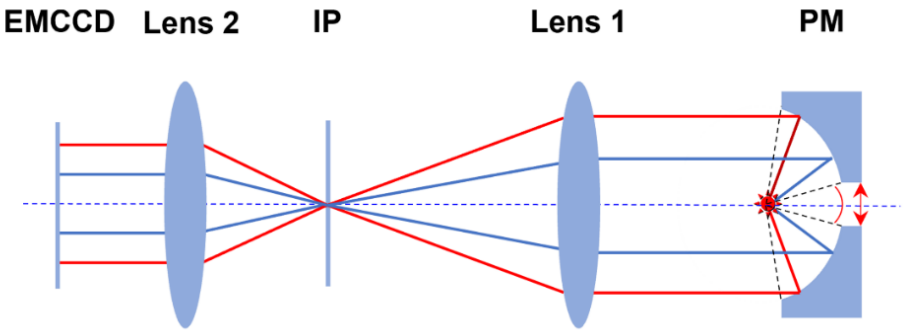

Figure 2.7: Schematic drawing for imaging the emission patterns by using the parabolic mirror (PM) as a laser focusing and signal collecting element.

The emission patterns are imaged with an electron-multiplying charge-coupled device (EMCCD). The red and blue lines represent the rays emitted from the sample. The dashed blue line indicates the optical axis of the imaging microscopy. The double-ended red arrow represents the PM forbidden region.

The maximum of collected out-of-plane angle θ with respect to the optical axis is calculated up to $\sim 87°$ due to a NA of 0.9986 in air. The presence of a forbidden region in PM is marked by double-ended red arrow in Figure 2.7. The losing of signal collection is due to the one-arm sample holder and the hole at the center of the PM. The minimum angle θ is calculated to be $\sim 27°$. Thus, the allowed collection angle θ is from $\sim 27°$ to $\sim 87°$. The used programs for emission pattern processing and simulation are developed by Dr. Quan Liu from Institute of Theoretical and Physical Chemistry of Eberhard Karls University of Tübingen.

The nonlinear optical properties of Yagi-Uda (YU) antennas are measured at the k-space imaging microscopy using a linearly polarized laser beam. Arrays of YU antennas are fabricated on a glass substrate by using electron-beam lithography, which is provided by the research group of Prof. Monika Fleischer from Institute of Applied Physics of Eberhard Karls University of Tübingen. Figure 2.8(a) shows the nonlinear optical image of an array of YU antennas, where the spacing distance of 1 μm between the adjacent YU antenna is well observed. The inset in Figure 2.8(a) shows the structural configuration of single YU antenna. The antenna comprises three elements (one reflector with a length of 110 nm, one feed with a length of 70 nm, and three directors with a length of 50 nm). Figure 2.8(b) shows the color-coded optical intensity map, where the polarization-dependent optical measurements are conducted by rotating the polarization direction of the laser light using a half-wave plate. The maxima of optical intensity are obtained when the laser light is polarized along the long axis of the element (e.g. reflector in YU antenna). Figure 2.8(c) shows the optical spectra of YU antenna under two experimental configurations as illustrated in the inset. The optical response is barely seen when the laser light is polarized along the short axis of the reflector in YU antenna; whilst both an intense metallic photoluminescence and a weak SHG peak are observed when the laser light polarization is oriented along the long axis of the reflector in YU

antenna. Considering the effect of polarization-dependent optical intensity, the emission pattern measurements are performed when the laser light is polarized along the long axis of the reflector in YU antenna. The emission pattern obtained from single YU antenna is nearly isotropic as shown in Figure 2.8(d). Moreover, the signal-to-noise ratio is adequate to visualize the emission directionality from single YU antenna. In summary, k-space imaging microscopy has been implemented into the confocal microscopy, which is sensitive to detect the optical image, spectral response, and angular emission pattern at the single-emitter level.

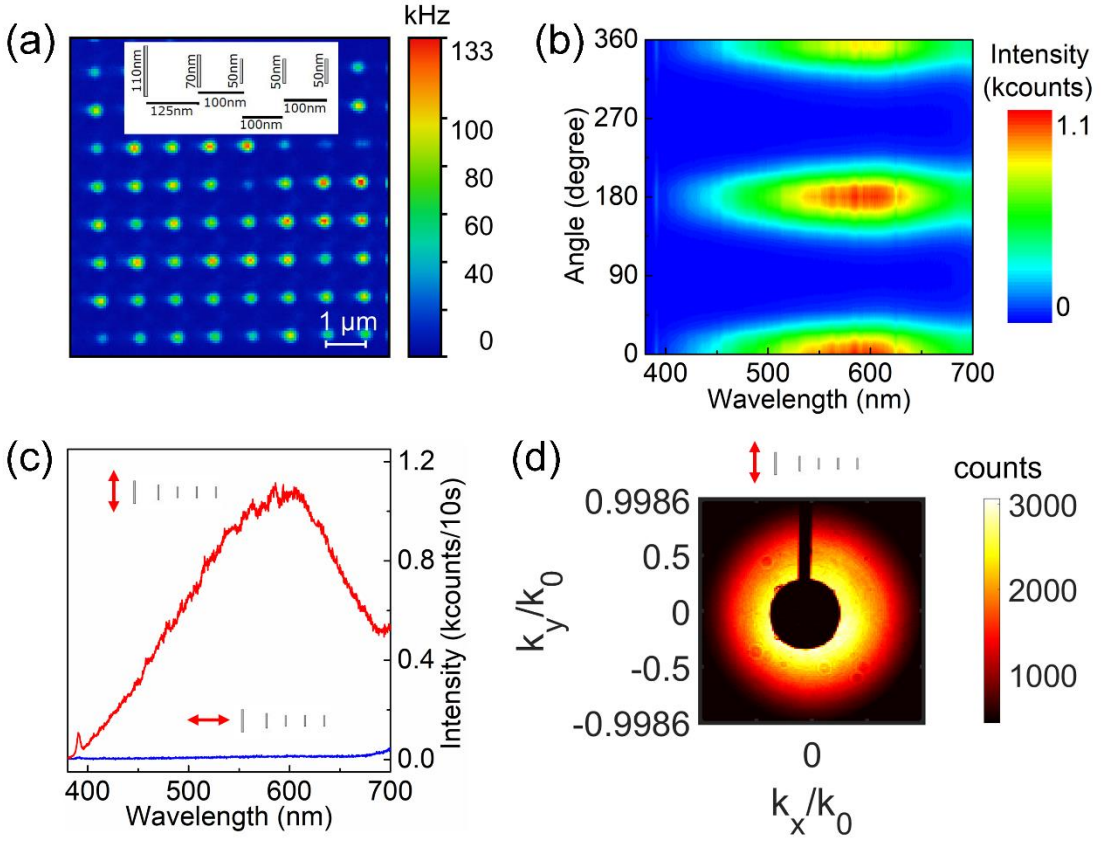

Figure 2.8: (a) Nonlinear optical image of an array of YU antennas. The inset is the structural configuration of a YU antenna. (b) The dependency of the optical intensity on laser beam polarization of YU antenna. (c) The optical spectra obtained from YU antenna. (d) The experimental emission pattern collected from YU antenna. The double-ended red arrow in (c) and (d) represents the polarization direction of the laser light.

2.2 Materials and characterization

2.2.1 Layered materials

All of the layered materials in this work are provided by our collaborators. The metal dichalcogenides containing single- and few-layered tungsten disulfide (WS_2) and molybdenum diselenide ($MoSe_2$) flakes are synthesized via chemical vapor deposition (CVD) method. As the substrates, precleaned silicon wafers with thermally grown silicon dioxide (thickness: 300 nm) are used. The flakes are provided by the former member Dr. Peng Miao from Institute of Theoretical and Physical Chemistry of Eberhard Karls University of Tübingen. The ultrathin film of copper phthalocyanine (CuPc) molecules with a thickness of 5 nm is deposited on the surface of $MoSe_2$ flake by vacuum thermal deposition. This deposition process is done by the research group of Prof. Dr. Heiko Peisert from Institute of Theoretical and Physical Chemistry of Eberhard Karls University of Tübingen. The ultrathin films of DH-P-TTA molecule (tetrathienoacene as the central core end-capped with 4-hexyl-1-(4,4,5,5-tetramethyl-1,3,2-dioxaborolan-2-yl) benzene) in this work are prepared on a precleaned silicon substrate covered with a thermally grown 300 nm layer of silicon dioxide via a solution-processed method combined with a slow solvent evaporation, which is provided by the research group of Prof. Dmitry Yu. Paraschuk from Enikolopov Institute of Synthetic Polymetric Materials of Russian Academy of Science.

2.2.2 General sample characterization

The bright-field optical images of the layered materials are conducted by using a commercially optical microscope (MX50, Olympus). The topographic information of the layered materials is characterized by atomic force microscopy (AFM, Multimode 8-HR, Bruker). The measurements are operated in a Peak

Force tapping mode by using a SCANASYST-AIR probe (Silicon Tip on Nitride Lever, Bruker). The optical absorption spectrum of CuPc molecule film on glass are conducted in the transmission mode using a confocal UV-visible-NIR system. The optical system involves one illumination optical fiber with a diameter of 600 μm and a collection fiber with a diameter of 150 μm.

Chapter 3 Edge-enhanced SHG emission in WS_2 monolayer

3.1 Introduction

The structural defects in two-dimensional transition metal dichalcogenides (TMDCs) materials including point-defects, edges, and boundaries have been identified by using conventional fluorescence, and Raman microscopies as well as tip-enhanced fluorescence/Raman spectroscopies.[7, 21, 98-100] For example, recently photoluminescence spectroscopy has been used to unravel the point defect induced trions in monolayer WS_2 with carrier screening engineering.[98] Tip-enhanced Raman spectroscopy is used to identify the types of edges, *i.e.,* zigzag edge, and armchair edge, in molybdenum disulfide (MoS_2) flakes based on close correlations between the electronic and structural properties.[99] In the last few years, the nonlinear optical properties of TMDCs materials have attracted intensive attention.[48] The SHG process is highly sensitive to the structural properties of nonlinear optical materials, which makes it a promising tool for characterizing the structural irregularities in TMDCs materials.[33, 101, 102] Two-photon photoluminescence spectroscopy can be also used to investigate the energy and symmetry of electronic states of TMDCs materials.[30, 32, 54] For WS_2 flake, one-photon excitation can reach excitonic states with even parity, while two-photon excitation will reach the so-called dark state with odd parity under an excitation of femtosecond laser at 10 K.[29, 55] Only recently, room-temperature 2PPL from WS_2 flake is reported, which is due to the suppressed nonradiative recombination by treating them with bis-(trifluoromethane) sulfonimide in order to repair S vacancies.[30]

In this chapter, the local structural properties of atomically thin WS_2 flake are explored by using SHG and 2PPL spectroscopy and microscopy. The SHG and 2PPL signals emitting from WS_2 flakes of different shapes and flake thicknesses are measured and discussed. The structural inhomogeneities within an individual WS_2 flake are revealed by both SHG and 2PPL microscopies. In addition, the structural symmetry of WS_2 flake is determined by the polarized SHG signal measurement. Our results could contribute to understand the influence of edge-defect on the nonlinear optical properties of WS_2 flakes.

The result of this chapter has been published:

Lin Pan, Peng Miao, Anke Horneber, Alfred J. Meixner, Pierre-Michel Adam, and Dai Zhang. Nanometer-scale structure property of WS_2 flakes by nonlinear optical microscopy: Implications for optical frequency converted signals. *ACS Applied Nano Materials* **2023**. https://doi.org/10.1021/acsanm.3c00804

3.2 Optical characterization of WS_2 monolayer

An AFM image of a triangle-shaped monolayer WS_2 flake on SiO_2 (thickness: 300 nm)/Si substrate is shown in Figure 3.1(a). The inset in Figure 3.1(a) depicts the topographic height profile which is taken from the position marked by the dashed white line in Figure 3.1(a). The thickness of 0.75 nm suggests that the measured WS_2 flake is indeed a monolayer.[103] Aligned particles along the edges of flake are observable, which have been determined to be the intermediate products (WO_xS_y) during the WS_2 chemical growth.[104] Figure 3.1(b) shows the PL spectrum obtained from the WS_2 monolayer, which is excited by a 532 nm CW laser. The emission at 640 nm dominantly originates from the direct excitonic transition between the lowest conduction band and the highest valence band.[105]

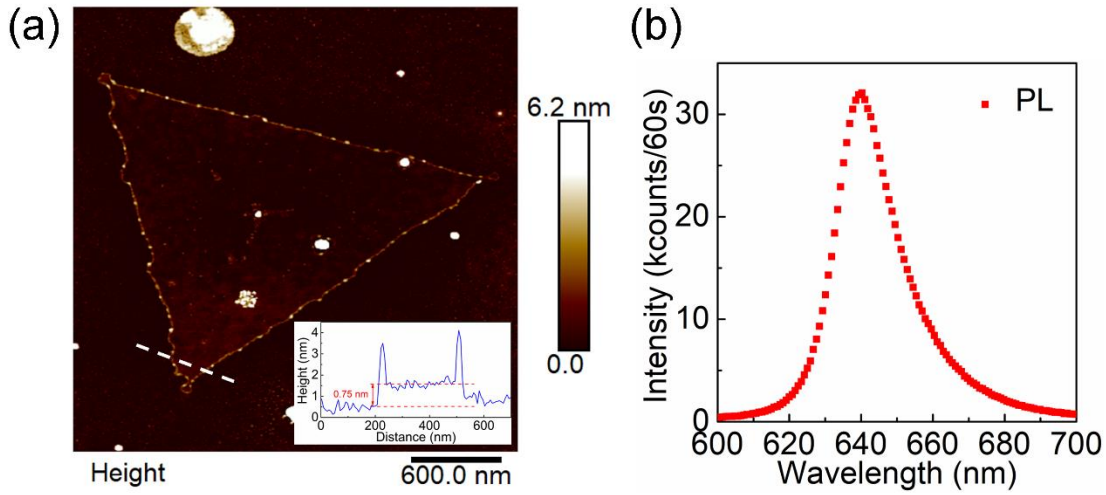

Figure 3.1: The characterizations of a monolayer WS_2 flake.

(a) The topographical image of a triangular WS_2 monolayer. The dashed white line indicates the position where the height profile (inset) is taken. (b) A single-photon PL spectrum measured from a WS_2 monolayer under the excitation of a 532 nm CW laser.

The Raman spectrum of the WS_2 monolayer is exhibited in Figure 3.2. The strongest Raman peak at 350 cm^{-1} contains three subpeaks (344 cm^{-1}, 350 cm^{-1}, and 354 cm^{-1}), which are resolved by using multipeak Lorentzian fitting. The flake exhibits that four Raman modes at 344 cm^{-1}, 350 cm^{-1}, 354 cm^{-1}, and 417 cm^{-1} are assigned to the in-plane mode ($E^1_{2g}(\mathrm{M})$), the second-order peak of the longitudinal acoustic mode ($2LA(\mathrm{M})$), the in-plane mode ($E^1_{2g}(\Gamma)$), and the out-of-plane mode ($A_{1g}(\Gamma)$), which is in good agreement with the reported vibrational modes of the monolayer WS_2.[106-108] The symbols "M" and "Γ" denote that the phonon dispersion (frequency and momentum) appear at the center of an edge (M-point) and the center (Γ-point) of the Brillouin zone, respectively. In addition, the schematic drawing of two first-order Raman modes ($E^1_{2g}(\Gamma)$ and $A_{1g}(\Gamma)$) of WS_2 flake are illustrated in the right panel of Figure 3.2.

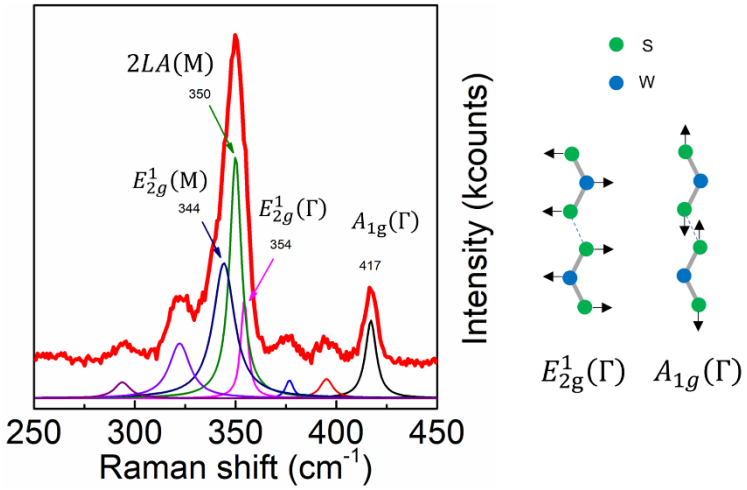

Figure 3.2: The Raman spectrum obtained from the same WS_2 monolayer that is investigated in Figure 3.1.

The Raman spectrum is fitted by the multipeak Lorentzian function. The schematic drawing (right panel) represents the two Raman active modes of monolayer WS_2. The Raman spectra are obtained using a confocal microscopy coupled with a 532 nm CW laser.

3.3 Efficient SHG emission at the edges of WS_2 monolayer

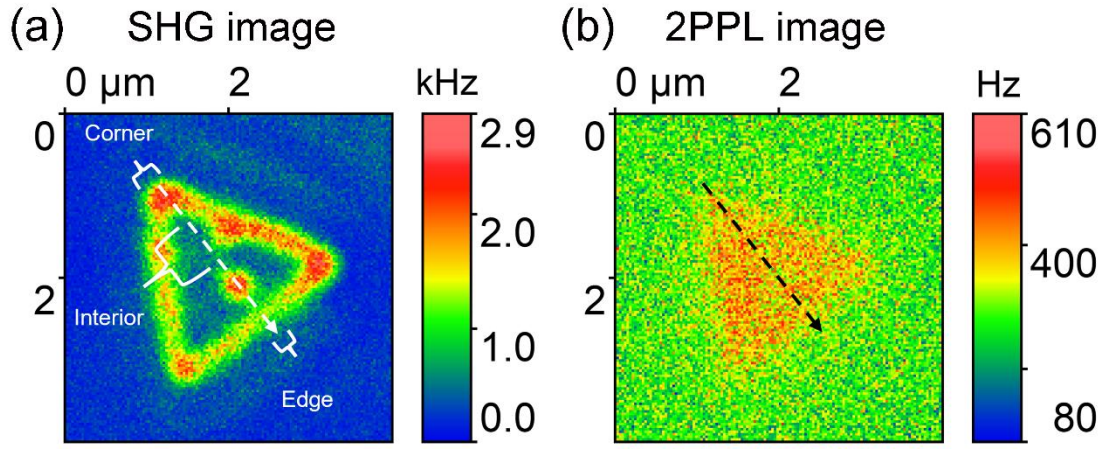

Figure 3.3: Nonlinear optical properties for the monolayer WS_2 flake.

The SHG image of the WS_2 monolayer (a) and the 2PPL image (b). The dashed white line in (a) and the dashed black line in (b) denote the positions and directions where a series of SHG and 2PPL spectra are collected, respectively. The samples are excited with a 780 nm femtosecond pulsed laser.

To investigate the nonlinear optical properties of WS_2 flakes, the samples are excited by a femtosecond pulsed laser with a wavelength of 780 nm. Figure 3.3(a) and (b) show the SHG and 2PPL optical images (scan size: 4 μm × 4 μm) of the same triangular WS_2 monolayer that is investigated in Figure 3.1, respectively. It is obvious that the SHG intensities are the strongest at the edges, while the 2PPL signal is the highest at the interior of the WS_2 monolayer.

To precisely compare the SHG and 2PPL optical intensities at the same position of the WS_2 monolayer, SHG and 2PPL optical spectra are measured along the dashed white and black lines labeled in Figure 3.3(a) and (b), respectively. The color-coded SHG and 2PPL spectral intensity are exhibited in the left and right panels of Figure 3.4(a), respectively. In Figure 3.4(b) the spectrally integrated SHG and 2PPL intensity as a function of the spectral sequence are also exhibited as the blue and red curves, respectively. The correlation between integrated SHG and 2PPL intensities is visualized. The comparisons in (a) and (b) clearly show that the strongest SHG intensity appears at the corner of WS_2 flake is observable, where the weakest 2PPL signal locates. In particular, we show the anticorrelation between the SHG and 2PPL optical signals at the location marked by the green rectangle in Figure 3.4(b).

In addition, three SHG and 2PPL spectra recorded at the corner, interior, and edge of the WS_2 monolayer are exhibited in Figure 3.4(c). The corner, interior, and edge positions are marked by the orange arrows in Figure 3.4(b). The SHG intensity at the corner is up to two times stronger than that at the interior; whilst the 2PPL intensity at the corner is weaker than that at the interior region. The excitation power-dependent plots of the intensities spectrally integrated from 380 nm to 400 nm (SHG, blue squares) and from 600 nm to 680 nm (2PPL, red circles) are shown in Figure 3.4(d). It can be seen that both SHG and 2PPL signals show quadratic power dependences, which suggests that both signals originated from two-photon induced nonlinear optical processes.

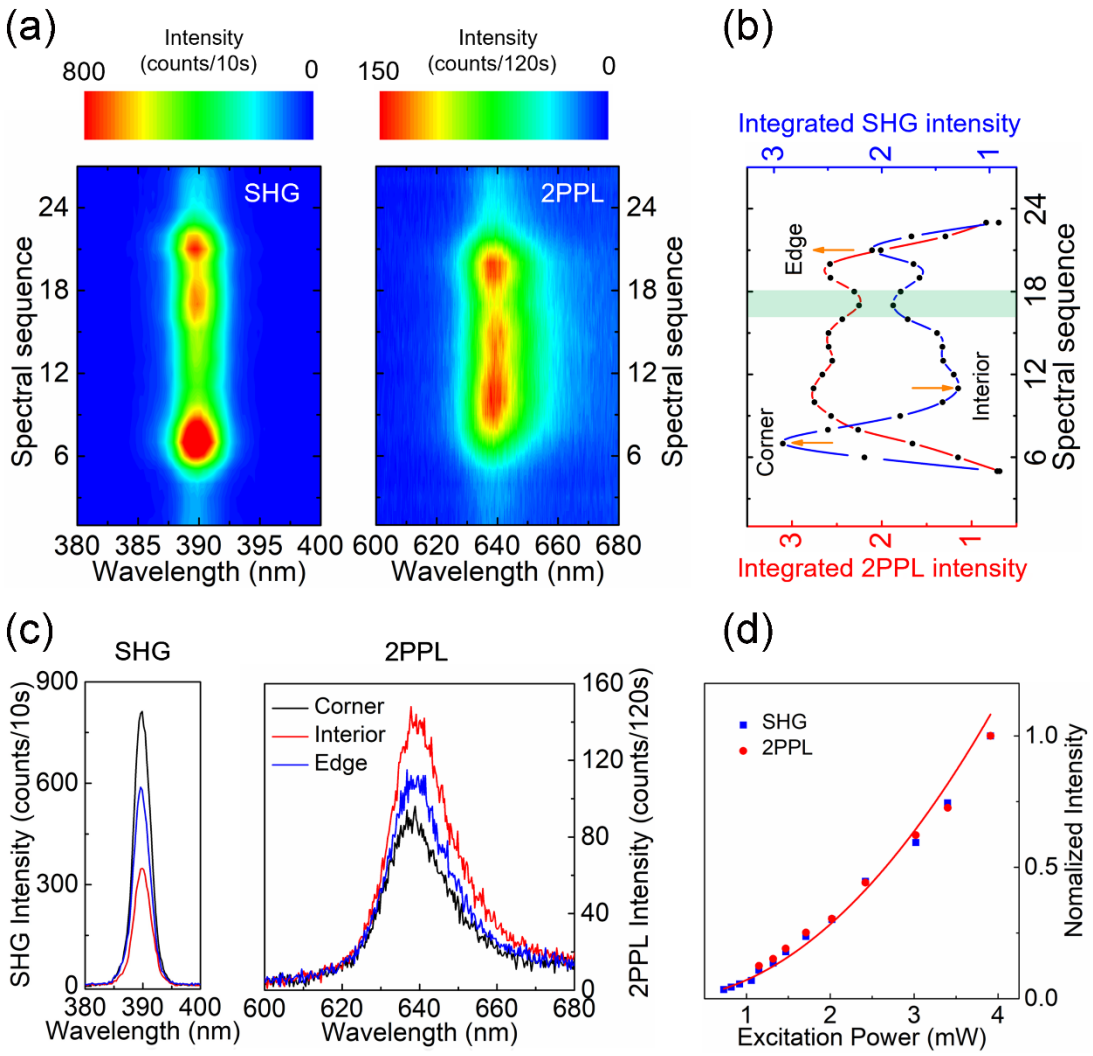

Figure 3.4: The correlation between the SHG and 2PPL intensities of the same monolayer WS_2 flake.

(a) The SHG (left) and 2PPL (right) color-coded intensity maps. The maps are based on the raw experimental spectra. (b) The correlation between the integrated SHG and 2PPL intensity obtained from the WS_2 monolayer. (c) The SHG (left) and 2PPL (right) spectra obtained at three positions of the WS_2 monolayer. The three positions are marked by the orange arrows in (b). (d) SHG (blue squares, spectrally integrated from 380 nm to 400 nm) and 2PPL (red circles, spectrally integrated from 600 nm to 680 nm) intensities as a function of the excitation power.

Only recently, the edge-enhanced SHG emission on MoS_2 monolayer was reported by Yin et al and Lin et al.[109, 110] They attributed the observed edge-enhanced SHG to the presence of localized mid-gap electronic states that was calculated by using density function theory (DFT). The SHG enhancement was

highly sensitive to the excitation wavelength and also the type of edge, *i.e.,* S-zigzag edge and S-Mo Klein edge. Here we follow the same consideration to address our results. In our work, we clearly observe an efficient edge SHG emission on WS_2 flakes when the excitation wavelength of 780 nm is used. This phenomenon demonstrates that new mid-gap energy states between the valence band and conduction band likely formed, due to the translational symmetry breaking and structural defects at the edges of WS_2 monolayer. The new mid-gap energy states could be nearly coincident with one of the virtual states of the SHG process, therefore second-order nonlinear susceptibility $\chi^{(2)}$ at the edges of WS_2 flake becomes large according to quantum mechanics.[110]

The room-temperature 2PPL spectroscopy is also used to characterize the structural properties of WS_2 flakes. Due to the third-order nonlinear optical process of 2PPL, the 2PPL intensities are extremely weaker as compared to that of PL response, as shown in Figure 3.1(b) and Figure 3.4(c). Usually, the PL spectroscopy is a reliable and quick method for the structural properties identification.[7, 111, 112] The structural defects in materials act as nonradiative recombination channels to quench the PL intensities.[113] In the previous results of CVD-grown WS_2 monolayer, the inhomogeneous PL features, *i.e.,* peak shift and darkening in certain regions are attributed to more structural defects (e.g., S vacancies).[25, 27, 108] In our study, we observe a 2PPL quenching at the edge and corner of WS_2 monolayer. These phenomena are probably driven by the as-grown structural defects, *i.e.,* edge and point defects.[108] The decreases in 2PPL intensities are mainly due to the electronic structure transition from direct to indirect bandgap and the defect-bound-excitons effect.[27]

3.4 Dependency of SHG and 2PPL properties on thickness

In this section, the nonlinear optical properties of the WS_2 flakes with different shapes, and layer thicknesses are measured and compared.

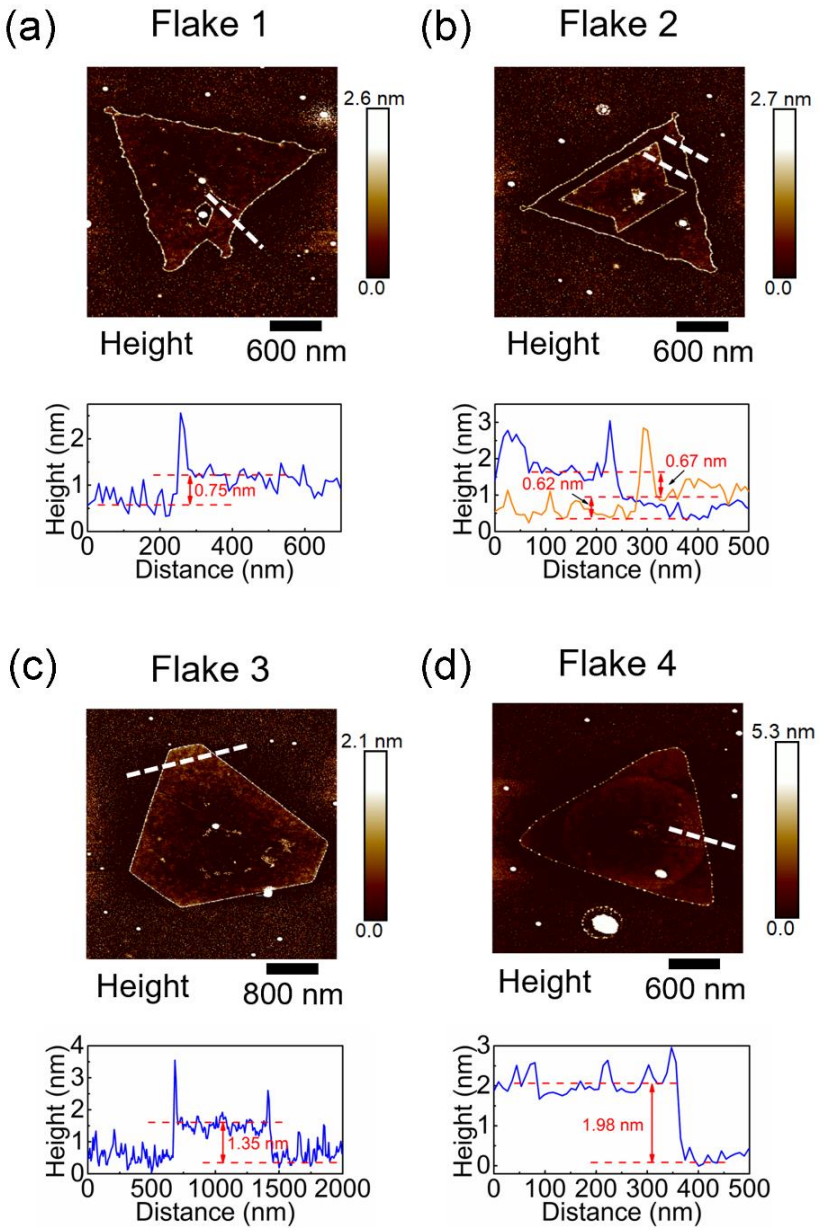

Figure 3.5: The AFM images and the height profiles of four WS_2 flakes (flake 1-4). The dashed lines denote the positions where the height profiles are taken.

The AFM images (upper panel) and corresponding height profiles (lower panel) of the WS_2 flake 1-4 are shown in Figure 3.5. The edges of all the measured flakes are aligned with nanoparticles that are likely the intermediate products from the CVD growth procedure.[114] The layer thickness of flake 1, 3, and 4 is ~0.75 nm, ~1.35 nm, and 1.98 nm, respectively, which suggests that flake 1, 3, and 4 is monolayer, bilayer, and three layers. Flake 2 contains one layer on the bottom with ~0.62 nm thick and a second layer on the top with ~0.67 nm thick.

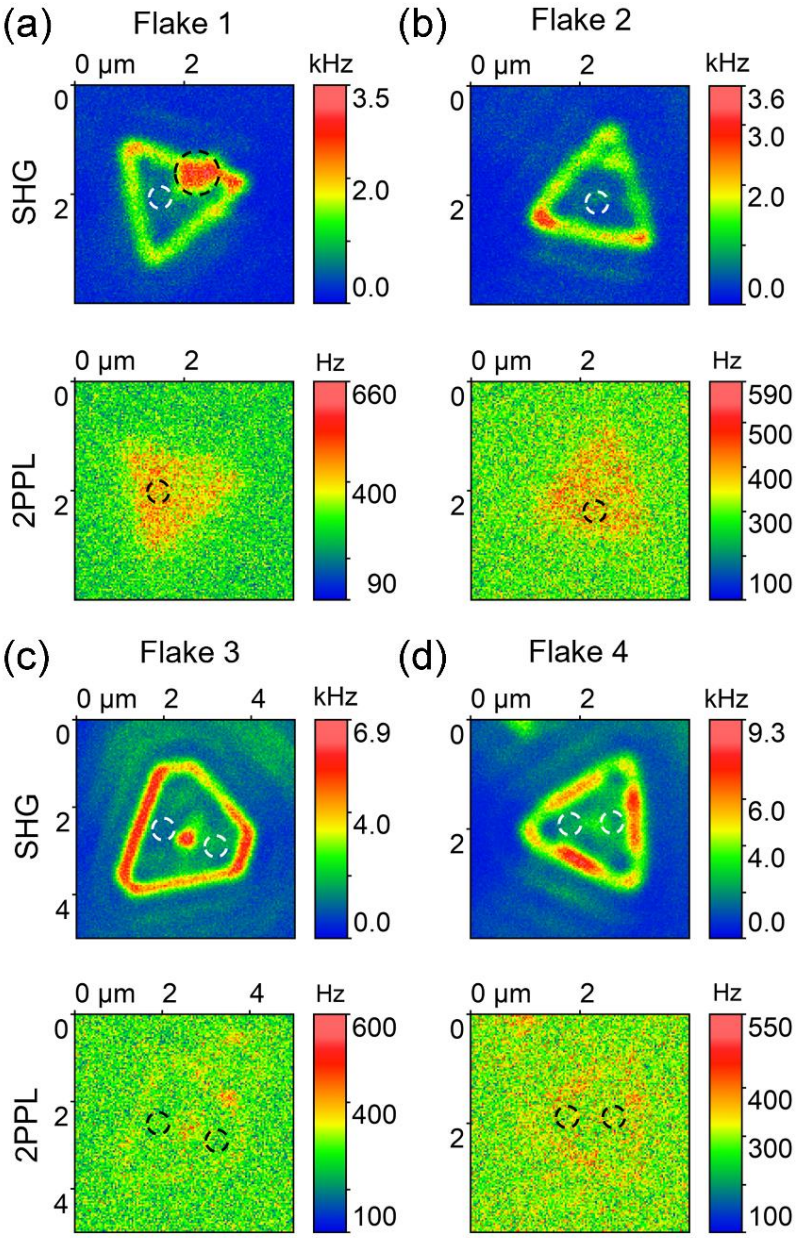

Figure 3.6: The SHG and 2PPL images of the same WS_2 flakes that are investigated in Figure 3.5. The optical intensities of flake 3 and 4 are the leftover of SHG signals that are not fully blocked by the filter.

Shown in Figure 3.6, all the WS_2 flakes show stronger SHG intensity at the edges when compared to that at the interior region. Both the flake 1 and flake 2 display the 2PPL emission, while no 2PPL signal can be observed for the flake 3 and flake 4. On flake 1 at the region where a strong SHG emission is shown marked by the dashed black line, almost no 2PPL signal can be observed, indicating the presence of more structural irregularities in this region.

These irregularities can be well seen in the corresponding AFM image in Figure 3.5(a). For flake 2, the 2PPL response observed in the bilayer region is likely owing to the 2PPL from the monolayer region. It should be mentioned that the 2PPL optical images of the flake 3 and flake 4 show extremely weak optical intensities. This optical signal is the SHG intensities emitting from the WS_2 flakes that can't be completely filtered out by the optical filter.

The thickness-dependent spectrally integrated SHG and 2PPL intensities are exhibited as shown in Figure 3.7. It can be seen that the SHG intensity increases as increasing of the flake thickness, and 2PPL signal is invisible in the flake 3 and flake 4.

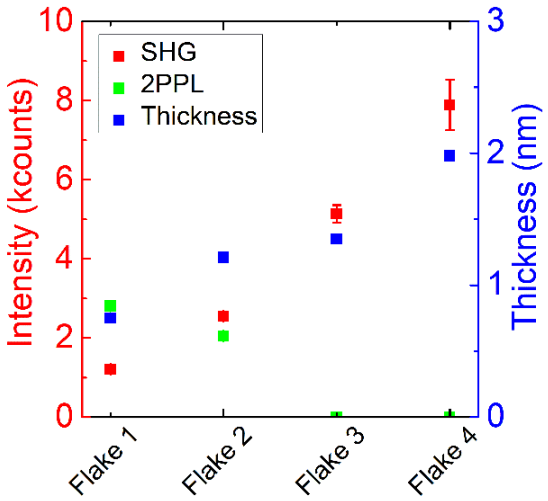

Figure 3.7: The thickness-dependent SHG (red squares, spectrally integrated from 380 nm to 400 nm) and 2PPL (green squares, spectrally integrated from 600 nm to 680 nm) intensities.

The dashed white and black circles in Figure 3.6 denote the positions where the SHG and 2PPL optical spectra are taken, respectively. The flake thicknesses are taken from the height profiles in Figure 3.5.

It has been reported that dependency of SHG optical signal on layer-number is related to the crystal stacking of WS_2 flake. Monolayer WS_2 has a large second-order nonlinear susceptibility $\chi^{(2)}$ because of the breaking of inversion symmetry.[35] For the rhombohedral 3R-phase WS_2 flake, the SHG intensity

shows a quadratic dependence on the layer number. Due to the same orientations of neighboring layers, the in-plane nonlinear dipoles of each 3R layer are well aligned for an atomic phase match, which induces a constructive superposition of second harmonic polarization between adjacent layers.[115] However, the orientations of adjacent layers are mirrored on the even-numbered hexagonal 2H-phase WS_2 flake, leading to a recovered inversion symmetry and then a cancellation of the nonlinear dipole, which induces no SHG signal on the even-numbered WS_2 flake.[35] Therefore, the measured WS_2 flakes are the 3R phase structure because its SHG intensity increases with increasing of layer thickness seen in Figure 3.7.

The layer thickness also has an apparent impact on the electronic band structure of WS_2 flake.[25, 116] The bulk and multilayer WS_2 flakes are indirect bandgap semiconductors; whilst the WS_2 flakes turn to be direct bandgap semiconductors when the layer numbers scale down to the monolayer limit. Therefore, with the increasing layer thicknesses, the photoluminescence quantum efficiencies of WS_2 flakes are suppressed.[116] This structure-related electronic property is well represented in Figure 3.7, where 2PPL emission is observed in monolayer flake 1, while 2PPL signal vanishes in bi/multilayer flakes (flake 3 and flake 4).

To probe the structural symmetry of the WS_2 flake using SHG signal, we perform the polarization dependence optical measurements by using a combination of a lambda half-wave plate and a Glan-Taylor prism analyzer. The half-wave plate is used to manipulate the polarization direction of the linearly polarized laser, and the parallel component of the SHG signal is selected by the Glan-Taylor prim analyzer that is positioned in front of the spectrometer entrance slit. Figure 3.8 shows the polar plot (left panel) of the polarization-dependent spectrally integrated SHG intensity. The polar plot of SHG signal

displays a six-fold rotational pattern. According to the reported literature,[18, 28, 35, 117] the parallel component of the SHG signal of WS_2 flake is expressed as:

$$I_{\parallel} = I_0 \cos^2(3\theta) \tag{3.1}$$

where θ indicates the angle between the direction of fundamental polarization (FP) and the armchair (AC) direction, and I_0 represents the maximum intensity of SHG signal as shown in the right panel of Figure 3.8. The measured SHG pattern is in good agreement with the above equation. The six-fold rotational pattern of SHG signal can be ascribed to the three-fold rotational symmetry of WS_2 flake.

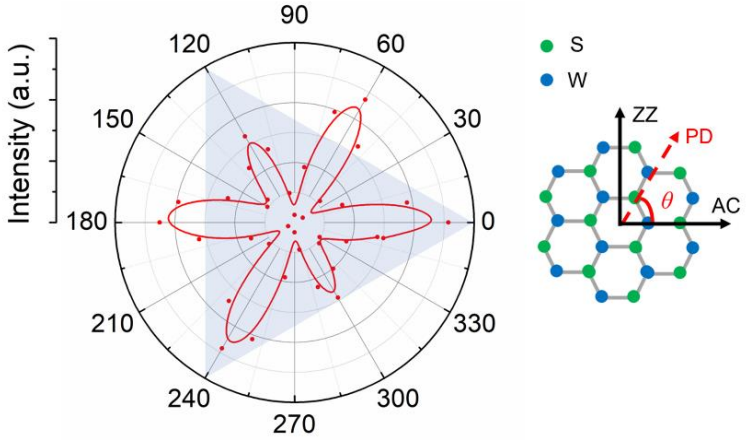

Figure 3.8: Left panel: polar plot using the polarization-dependent spectrally integrated SHG intensity. The parallel component of the SHG signal is collected in the optical measurement. The transmission axis of analyzer is kept parallel to the polarization direction of the excitation laser. The polar plot of SHG signal displays a six-fold rotational pattern. The red dots are the experimental data, which is fitted (red line) using the equation (3.1). Right panel: top view of the WS_2 crystallographic orientation with respect to the polarization direction of the laser light. The red arrow is the polarization direction (PD) of the laser light. The zigzag (ZZ) and armchair (AC) directions are also represented by the black arrow. The green and blue circles indicate the sulfur and tungsten atoms, respectively.

3.5 Conclusion

In conclusion, the structural properties of WS_2 flakes can be well-revealed by SHG and 2PPL microscopies and spectroscopies as well as AFM technique. We observe the edge-enhanced SHG response in the single-layered and few-layered WS_2 flakes, which is due to the translational symmetry breaking and more structural defects at the edges of WS_2 flakes. Notably, room-temperature 2PPL signal is anticorrelated with the SHG signal in a WS_2 monolayer. The observed results are due to the presence of new mid-gap electronic states between the valence and conduction bands at the flake edges. The SHG intensity increases with increasing flake thickness; whilst the 2PPL optical signal is only visible in monolayer WS_2. The polarization-dependent SHG signal exhibits a six-fold rotational pattern, indicating the three-fold rotational symmetry of WS_2 flake.

Chapter 4 Crystal orientation and grain boundaries in $MoSe_2$ flake

4.1 Introduction

Characterizing the structural properties of TMDCs materials has become a critical hot topic for understanding and controlling their electronic and optical properties.[8, 50, 103, 118, 119] Recently, SHG microscopy has been established as an ultrasensitive and nondestructive probe for determining the structural properties in TMDCs materials.[48, 51, 120, 121] The presence of mid-gap states in the electronic band of monolayer WS_2 flake, which is induced by the sulfur vacancies in the structure, has been studied by the SHG microscopy combined with PL microscopy.[27] In addition to the point defect, the edge-induced SHG enhancement has been also reported, which has been attributed to the enhancement of second-order nonlinear susceptibility induced by the structural termination at the edges of MoS_2 monolayer.[110] Due to the strong correlation between the structural symmetry and SHG optical process, polarization-resolved SHG spectroscopy has been employed for revealing the structural orientation and structural symmetry as well as the strain applied in TMDCs materials.[18, 28, 122] Usually, the SHG response vanishes at the grain boundaries of monolayer MoS_2 flake due to the mirrored crystal symmetry in the neighboring grains.[123, 124] Only recently, the grain boundaries and edges appear bright in the SHG image of TMDCs materials via the dark-field SHG microscopy. This observation has been made possible since this kind of SHG microscopy can boost the contrast of optical images by suppressing light scattered from the homogeneous areas.[125]

In this chapter, the structural irregularities properties on atomically thin $MoSe_2$ flakes are further investigated by SHG combined with 2PPL emissions. Firstly, the local structure properties of triangle-shaped $MoSe_2$ flakes are explored using their SHG and 2PPL images. Subsequently, polarized SHG optical measurements are performed to determine the crystal orientation of discrete $MoSe_2$ flakes. More importantly, grain boundaries and structural orientations within a single six-pointed star $MoSe_2$ flake are revealed using SHG microscopy. The observations contribute to an in-depth understanding of the correlation between the structural properties and nonlinear optical signals in TMDCs materials.

4.2 SHG and 2PPL emissions in $MoSe_2$ flake

The nonlinear optical properties of triangle-shaped $MoSe_2$ flakes grown on a 300 nm-thick SiO_2 layer coated Si substrate are performed by using a confocal microscopy coupled with a 780 nm femtosecond pulsed laser. The nonlinear optical image of a triangular $MoSe_2$ flake is exhibited in Figure 4.1(a). The optical intensities shown in Figure 4.1(a) are the sum of SHG and 2PPL optical intensities. The AFM topographical image of the corresponding $MoSe_2$ flake is shown in Figure 4.1(b). The height profile is shown in the inset of Figure 4.1(b), where the thickness of 1.425 nm indicates that the $MoSe_2$ flake is bilayer. The thickness of the central region marked by the dashed red circle is up to 4.444 nm, which suggests that the central region of the flake is multilayer. Moreover, we find that some nanoparticles are aligned along the flake edge, especially the region marked by the dashed yellow circle. The nanoparticles have been reported to be the intermediate byproducts of $MoSe_2$. The intermediate byproducts could be the oxidation products (MoO_xSe_y or MoO_3) either through the CVD growth process, or through the aging effect in air.[114, 126] By comparing the nonlinear optical image and the AFM image, one can see that the nonlinear optical properties are sensitively correlated to the topography of the $MoSe_2$

flake, which is visualized by the regions marked by the dashed red and yellow circles in Figure 4.1(a) and (b).

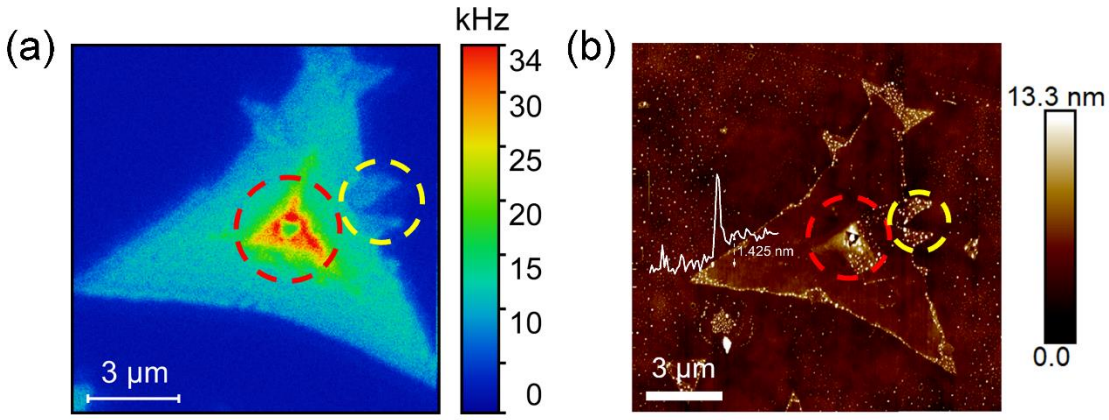

Figure 4.1: (a) Nonlinear optical image of a triangular $MoSe_2$ flake. SHG and 2PPL signals are simultaneously collected in the nonlinear optical image. (b) The AFM topographical image of the corresponding $MoSe_2$ flake. The inset in (b) is the height profile of the flake.

To reveal the local structure dependency of the SHG and 2PPL signals, they are spectrally selected by using optical filter (a 10 nm band pass filter is used for SHG imaging; whilst a 488 nm long pass filter together with a 680 nm short pass filter are used for 2PPL imaging). The SHG and 2PPL images of the $MoSe_2$ flake that are investigated in Figure 4.1, are shown in Figure 4.2(a) and (b), respectively. In Figure 4.2(a), the central region (marked by the dashed red circle) shows a strong SHG intensity; whilst in the area covered by nanoparticles (dashed yellow circle) the SHG signal is almost nonvisible. The results suggest that the SHG response is highly sensitive to the local structure of the $MoSe_2$ flake. In Figure 4.2(b), the flake central region shows a higher 2PPL intensity than that in other regions, indicating the correlation between 2PPL optical property and flake thickness.

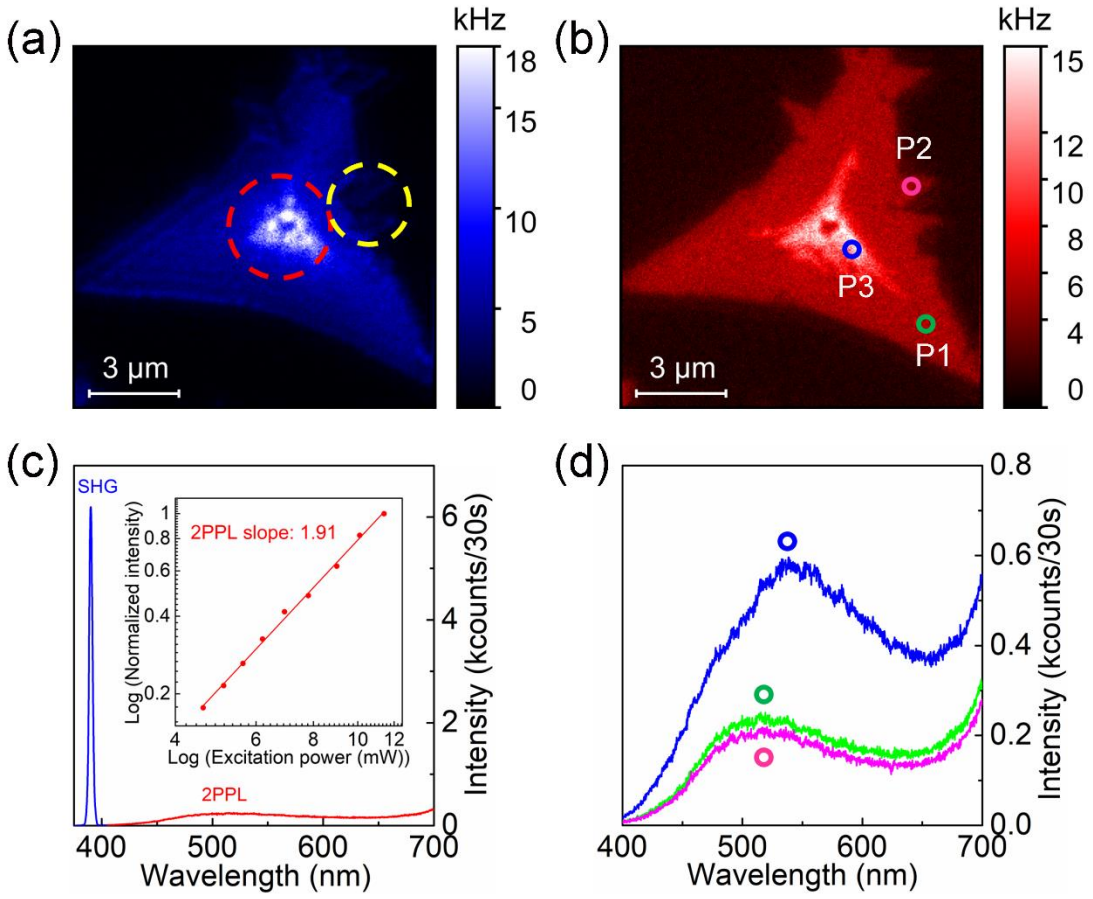

Figure 4.2: SHG and 2PPL characterizations of the triangular $MoSe_2$ flake.

(a) and (b) show the SHG and 2PPL images of the flake, respectively. The blue, green, and pink circles in (b) indicate the positions where the 2PPL spectra are measured. (c) Optical spectrum collected from the $MoSe_2$ flake. The blue and red curves indicate the SHG and 2PPL signals, respectively. The inset in (c) shows the double logarithmic plot of the excitation power-dependent integrated intensity. (d) 2PPL spectra obtained from three positions (P1, P2, and P3) on the $MoSe_2$ flake.

Figure 4.2(c) shows an optical spectrum obtained from the $MoSe_2$ flake. The sharp and intensive peak at 390 nm is the SHG signal, which is highlighted in blue. The 2PPL signal is highlighted in red, and its peak maximum is roughly at ~520 nm. The double logarithmic plot for the 2PPL intensity spectrally integrated from 400 nm to 700 nm as a function of excitation power is exhibited in the inset of Figure 4.2(c). The slope value of 1.91 confirms the two-photon induced nonlinear optical process. The 2PPL spectra obtained at three different positions of the $MoSe_2$ flake are exhibited in Figure 4.2(d). The green (P1), pink

(P2), and blue (P3) circles marked in Figure 4.2(b) denote the positions where the optical spectra are taken. Both 2PPL peak maxima at the position P1 and P2 locate at ~520 nm, and the 2PPL intensity at the position P2 is slightly weaker than that at the position P1. Interestingly, the 2PPL property at the position P3 is quite different, which can be proved by a giant 2PPL optical intensity and its peak maximum that is shifted to ~540 nm.

The 2PPL peak maxima observed from the $MoSe_2$ bilayer (position P1 and P2) and multilayer (position P3) are totally different from the PL peak at ~819 nm excited with a 532 nm CW laser that was reported in the literatures.[100, 127-129] The PL peak of the $MoSe_2$ flake is mainly due to the direct excitonic transition, namely A exciton.[130] To understand the origin of these extraordinary 2PPL properties, the absorption properties of the $MoSe_2$ flake need to be fully considered. It was reported that the $MoSe_2$ flakes exhibit strong absorption in the spectral range of 1.50 eV to 3.50 eV.[131] In particular, the absorption in the spectral range of 1.50 eV to 2.50 eV is dominated by four prominent transitions, namely A exciton (~1.57 eV), B exciton (~1.82 eV), A' exciton (~2.30 eV), and B' exciton (~2.38 eV), which are due to the direct-gap transitions between the maxima of split valence bands and the minimum of conduction band.[130, 132, 133] Here in this work, the energy of two-photon excitation is ~3.18 eV, in good resonance with the reported absorption range of the $MoSe_2$ flake. The 2PPL peak maxima of the $MoSe_2$ multilayer at ~540 nm (~2.30 eV) and bilayer at ~520 nm (~2.38 eV) match the A' exciton and B' exciton transitions, respectively. Therefore, we attribute the observed 2PPL of the $MoSe_2$ flake to the direct-gap luminescence.

4.3 Determining crystal orientations in $MoSe_2$ flakes

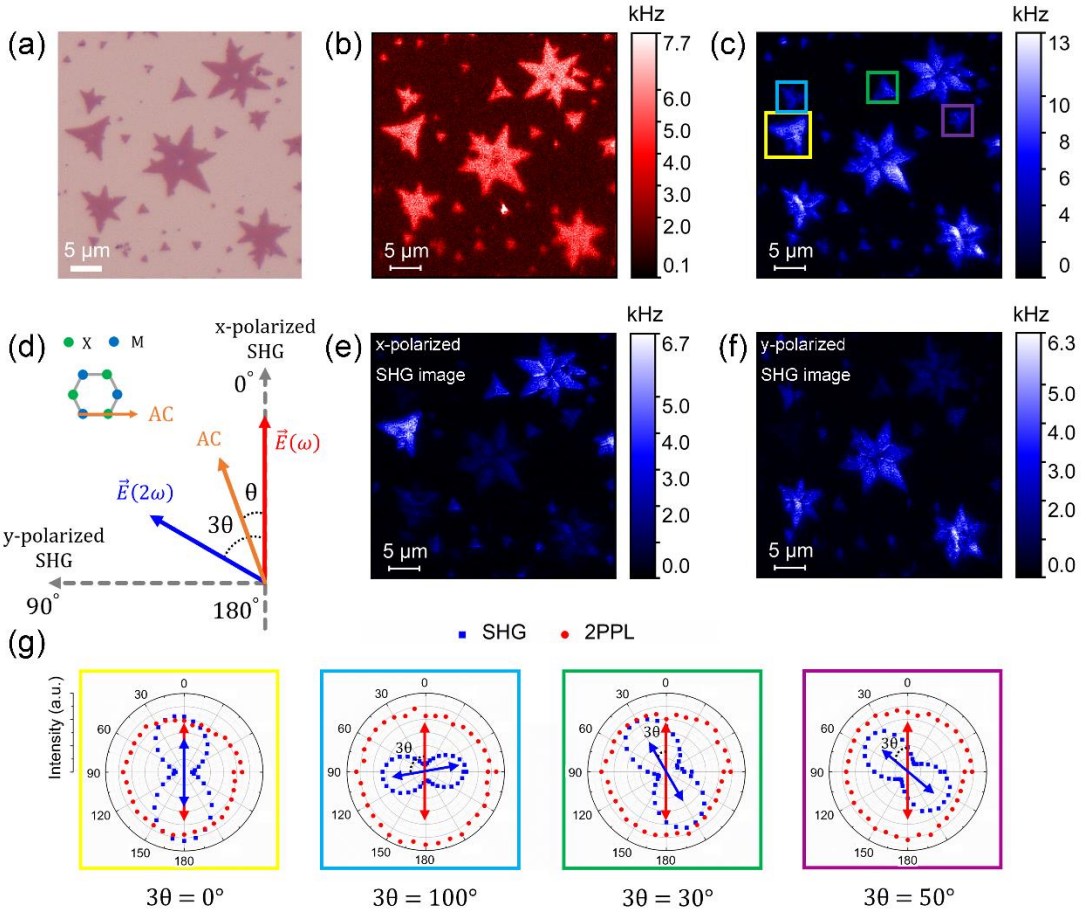

Figure 4.3: Crystal orientation determined by polarized SHG imaging and angular dependence of SHG intensities.

(a) Bright-field optical image, (b) 2PPL image, and (c) SHG image of the $MoSe_2$ flakes. The 2PPL signals in (b) and SHG signals in (c) are collected without an analyzer placed in front of the detector. (d) A schematic for illustrating the relative orientation between the generated SH electric field (blue arrow) with the fundamental excitation (red arrow) and the armchair direction (AC, orange arrow) in a $MoSe_2$ flake. The x- and y-components of the SHG signals are indicated as dashed arrows. (e) The x-polarized SHG image and (f) y-polarized SHG image of the $MoSe_2$ flakes. The x-polarized (y-polarized) SHG image is measured under the experimental configuration, where the transition axis of analyzer is parallel (vertical) to the laser polarization direction. (g) The polar plots of SHG (spectrally integrated from 380 nm to 400 nm) and 2PPL (spectrally integrated from 400 nm to 700 nm) intensities obtained from four $MoSe_2$ flakes. The four $MoSe_2$ flakes are marked by blue, green, yellow, and purple squares shown in (c). The double-ended red arrow, and double-ended blue arrow in (g) represent the laser polarization direction, and generated SHG polarization direction, respectively.

To demonstrate the crystal orientation of $MoSe_2$ flakes, we focus on the region, where the individual $MoSe_2$ flakes with different geometries can be seen. In Figure 4.3(a), both triangular and six-pointed star $MoSe_2$ flakes can be clearly observed. As the 2PPL properties are highly sensitive to the flake thickness, we first perform the 2PPL imaging measurement. In Figure 4.3(b), these $MoSe_2$ flakes show a homogeneous 2PPL intensity, which indicates the $MoSe_2$ flakes in the area likely have the same thicknesses. Figure 4.3(c) shows the SHG image of the same $MoSe_2$ flakes, where the SHG signals are collected without an analyzer placed in front of the detector when the $MoSe_2$ flakes are excited with a linearly polarized pulse laser.

To illustrate the correlation between the SHG response and the crystal orientation of $MoSe_2$ flake, a schematic is exhibited in Figure 4.3(d). The armchair direction (AC, orange arrow) of $MoSe_2$ flake is at an angle θ versus the laser electric field $\vec{E}(\omega)$ (red arrow). Here, the angle θ represents the crystal orientation with respect to the laser polarization direction. As the monolayer $MoSe_2$ flake belongs to the D_{3h} point group,[28] the angle θ range is from $0°$ to $60°$. It is reported that the generated SH electric field $\vec{E}(2\omega)$ (blue arrow) is at an angle 3θ (from $0°$ to $180°$) with respect to the laser electric field $\vec{E}(\omega)$,[33, 134] as shown in Figure 4.3(d). In the polarized SHG imaging measurements, the laser polarization direction and the flake orientation are fixed; whilst the polarization direction of the generated SHG signal is analyzed by a linear polarizer. In Figure 4.3(d), x-polarized (y-polarized) SHG component (dashed grey arrow) is obtained under the experimental configuration, where the transmission axis of the polarizer is positioned parallel (perpendicular) to the polarization direction of the laser light. Figure 4.3(e) and (f) represent the SHG images using the x-polarized and y-polarized components of SHG signals of the $MoSe_2$ flake, respectively. It is clearly observed that some bright $MoSe_2$ flakes in the x-polarized SHG image (Figure

4.3(e)) appear dark in the y-polarized SHG image (Figure 4.3(f)). The generated SH field $\vec{E}(2\omega)$ can be estimated through the SHG signal of $MoSe_2$ flake in the polarized SHG images. When the angle 3θ is in the range of either $0°$ to $45°$ or $135°$ to $180°$, the $MoSe_2$ flakes can be bright in the x-polarized SHG image; whilst the angle 3θ is within the range of $45°$ to $135°$, the $MoSe_2$ flakes show bright in the y-polarized SHG image.

To further explore the underlying crystal orientations of individual $MoSe_2$ flakes, polarization-dependent SHG optical spectroscopy is performed. The measured $MoSe_2$ flakes are marked by blue, green, yellow, and purple squares shown in Figure 4.3(c), and the SHG intensities (spectrally integrated from 380 nm to 400 nm) collected at varying angles of the linear polarizer are shown as the polar plots in Figure 4.3(g). The laser polarization direction and generated SHG polarization direction are represented by the double-ended red arrow and blue arrow, respectively. It is clearly observed that the measured $MoSe_2$ flakes exhibit linearly polarized SHG. The polarization direction of the generated SHG is not identical with that of the laser light. From the experimental results shown in Figure 4.3(g), it is found that the four measured $MoSe_2$ flakes exhibit distinct differences in the angle 3θ between the generated SH field $\vec{E}(2\omega)$ and the laser electric field $\vec{E}(\omega)$, which suggests the differences in the angle θ for the four measured flakes. The results are attributed to the different crystal orientations of $MoSe_2$ flakes with respect to the polarization direction of the laser light. However, the exact crystal orientation (Mo-Se or Se-Mo) could not be successfully determined, which is ascribed to the loss of phase information in the polarization-dependent SHG measurements.[124] In addition, the angle-dependent 2PPL intensities spectrally integrated from 400 nm to 700 nm of the four $MoSe_2$ flakes are also plotted, as shown in Figure 4.3(g) as red dots. The 2PPL signals show an almost perfectly circular emission pattern, which clearly demonstrates that 2PPL signal emitting from the $MoSe_2$ flake is non-polarized.

The observed isotropic 2PPL pattern is due to the high in-plane structure symmetry of the $MoSe_2$ flake, which leads to an isotropic in-plane response to the polarization direction of the laser light.[135]

4.4 Revealing grain boundaries by SHG emission

The crystal orientation of neighboring grains within a $MoSe_2$ flake is also investigated by the polarization dependence of SHG spectroscopy. The SHG image of a $MoSe_2$ flake is exhibited in Figure 4.4(a), which contains six jointed grains. Interestingly, brighter SHG signals along the boundaries between the grains are observed as compared to that inside the individual grains. Three SHG polar plots measured on the three neighboring grains of the $MoSe_2$ flake are exhibited in Figure 4.4(b). The exactly measured positions labeled by P1, P2, and P3 are shown in Figure 4.4(a). The double-ended red and blue arrows in Figure 4.4(b) represents the laser polarization direction and generated SHG polarization direction, respectively. Linear polarization direction of the generated SHG can be clearly seen from the three adjacent grains of the $MoSe_2$ flake. Notably, the SH fields $\vec{E}(2\omega)$ generated from the three neighboring grains (P1, P2, and P3) all have nearly the same angle 3θ (definition seen in Figure 4.3(d)) vs. the laser electric field $\vec{E}(\omega)$ that is about $30°$. Interestingly, no such kind of intensity variation can be seen at these adjoint lines in the 2PPL image of this $MoSe_2$ flake, as shown in Figure 4.4(c). These different phenomena can be well-visualized by SHG and 2PPL spectra collected along the dashed white line that is marked in Figure 4.4(c). Both SHG and 2PPL color-coded intensity maps are shown in Figure 4.4(d). Whilst the SHG signals show clear variations at the adjunctions between two grains, the 2PPL intensity is homogeneous in these regions.

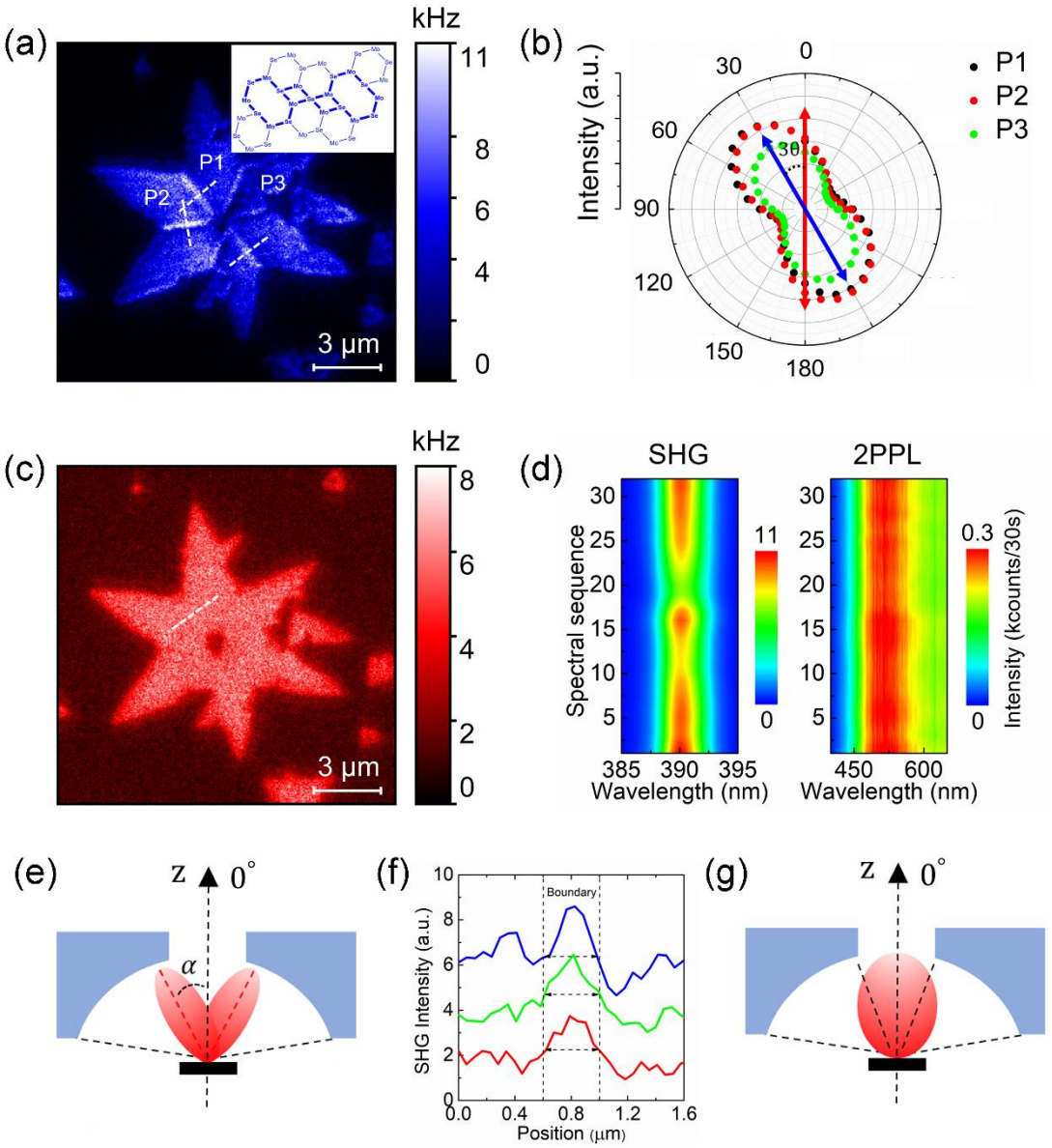

Figure 4.4: Characterization of grain boundaries and crystal orientation within a symmetric, six-pointed star $MoSe_2$ flake by SHG signal.

(a) SHG image of a $MoSe_2$ flake. The inset shows the top view of crystal structure for mirror twin boundaries. (b) SHG polar plots from three different positions of the $MoSe_2$ flake. The positions are labeled by P1-3 shown in (a). The double-ended red and blue arrows in (b) denote the laser polarization direction and generated SHG polarization direction, respectively. (c) 2PPL image of the corresponding $MoSe_2$ flake. (d) SHG and 2PPL color-coded intensity maps. The white dashed arrow in (c) denotes the position where the line-trace SHG and 2PPL spectra are obtained. (e) and (g) show the schematic drawings of SHG radiation patterns from the mirror twin boundaries and inside the individual grains, respectively. The angle α represents the SHG emission direction with respect to z-axis. (f) Cross sections of SHG intensity from three locations marked by the dashed white lines in (a).

From Figure 4.4(b), one can be concluded that the crystal orientations of neighboring grains rotate with a relative in-plane angle of either $0°$ or $180°$, which is due to the loss of phase information in the SHG measurements. According to the previous dark-field transmission electron microscopy studies,[8] the six-pointed star TMDCs flake usually contains mirror twin boundaries. The mirror twin boundary belongs to the line defect involving 8-4-4 motif that is shown in the inset of Figure 4.4(a), which is formed by two grains with a relative in-plane rotation of $180°$. Due to the destructive interference of the SHG signals at the mirror twin boundaries, the SHG intensity is considerably suppressed at the grain boundaries,[123, 124, 134] which is different from our observation shown in Figure 4.4(a).

In general, the structural discontinuities appear bright by dark-field (DF) linear optical microscopy, which is due to the suppression of the light scattered from the homogeneous areas. Only recently, by using a DF-SHG microscopy, such the bright grain boundary effect on monolayer TMDCs flakes was visualized.[125] Using a two-dipole model, they pointed out that the out-of-phase SH electric fields generated from the mirror twin boundaries can create a constructive interference at a large out-of-plane angle (with respect to the normal of the sample plane), which can be detected by a DF-SHG microscopy. The SHG emissions from the homogeneous regions, however, can be blocked due to the DF filter. Thus, the grain boundaries of TMDCs can be visualized by suppressing the SHG emissions from the homogenous regions. Here we follow the same considerations to understand our observation that is shown in Figure 4.4(a). Figure 4.4(e) shows the schematic drawing of SHG radiation pattern from the mirror twin boundaries. The angle α allowing a constructive interference of the two SH radiation dipole moments is calculated by:[125]

$$d \sin \alpha = \lambda/2 \tag{4.1}$$

where the λ is the SHG wavelength, and the d denotes the mean distance

between the two neighboring grains. In our work, the SHG wavelength λ situates at 390 nm, and the distance d is analyzed up to ~400 nm by considering a Gaussian profile as shown in the cross sections of SHG intensity in Figure 4.4(f). Thus, the angle α of allowing a SHG constructive interference is estimated as $\sim 29.5°$. It lies in the collection angle range ($\sim 27°$ to $\sim 87°$) of the parabolic mirror; hence the SHG signal generated from the boundary can be still measured. On the other hand, since the in-sample-plane SH radiation dipole moments are generated inside the individual grains, the SHG radiation direction at an out-of-plane angle α of $0°$ cannot be efficiently collected by the parabolic mirror, which is due to the presence of a forbidden collection region ($0°$ to $\sim 27°$), as shown in Figure 4.4(g). Therefore, the brighter grain boundaries can be observed when compared to that inside the individual grains of the $MoSe_2$ flake.

In addition, the local structure-related SHG and 2PPL properties of $MoSe_2$ flakes of different shapes are investigated. The SHG and 2PPL images of flake 1 and flake 2 are illustrated in Figure 4.5. Interestingly, we clearly observe the variations in the SHG intensity of the measured $MoSe_2$ flakes. The insets in Figure 4.5(a) and (c) represent SHG intensity profiles of flake 1 and flake 2 which are taken along the dashed white lines marked in Figure 4.5(a) and (c), respectively. The bright grain boundary and slight edge enhancement of SHG response are clearly observable on both flake 1 and flake 2; whilst the homogeneous distribution of the 2PPL signals at the corresponding region of $MoSe_2$ flakes are shown in the insets of Figure 4.5(b) and (d). It is well-known that the SHG radiations are highly dependent on the second-order nonlinear susceptibility $\chi^{(2)}$. When the grain boundaries of the $MoSe_2$ flakes are formed by the two mirror grains, the boundaries require a transition from $\chi^{(2)}$ to $-\chi^{(2)}$; whilst the flake edges exhibit a transition from $\chi^{(2)}$ to 0, which is due to the structural terminations at the edges. It has been reported that any nonlinear materials with the discontinuity in $\chi^{(2)}$ can lead to the effect of so-called

Čerenkov SHG process, where the SH radiation direction at a large out-of-plane angle (with respect to the normal of the sample plane) is observed at the boundaries formed by two mirror domains in nonlinear bulk media.[136, 137] Here in our work, both grain boundaries and edges of the $MoSe_2$ flakes experience the discontinuity in $\chi^{(2)}$, then leading to the SH radiation direction with a large out-of-plane angle α, as shown in Figure 4.4(e), which can be efficiently collected by the parabolic mirror. Therefore, we observed the bright SHG signals at the grain boundaries and edges of the $MoSe_2$ flakes.

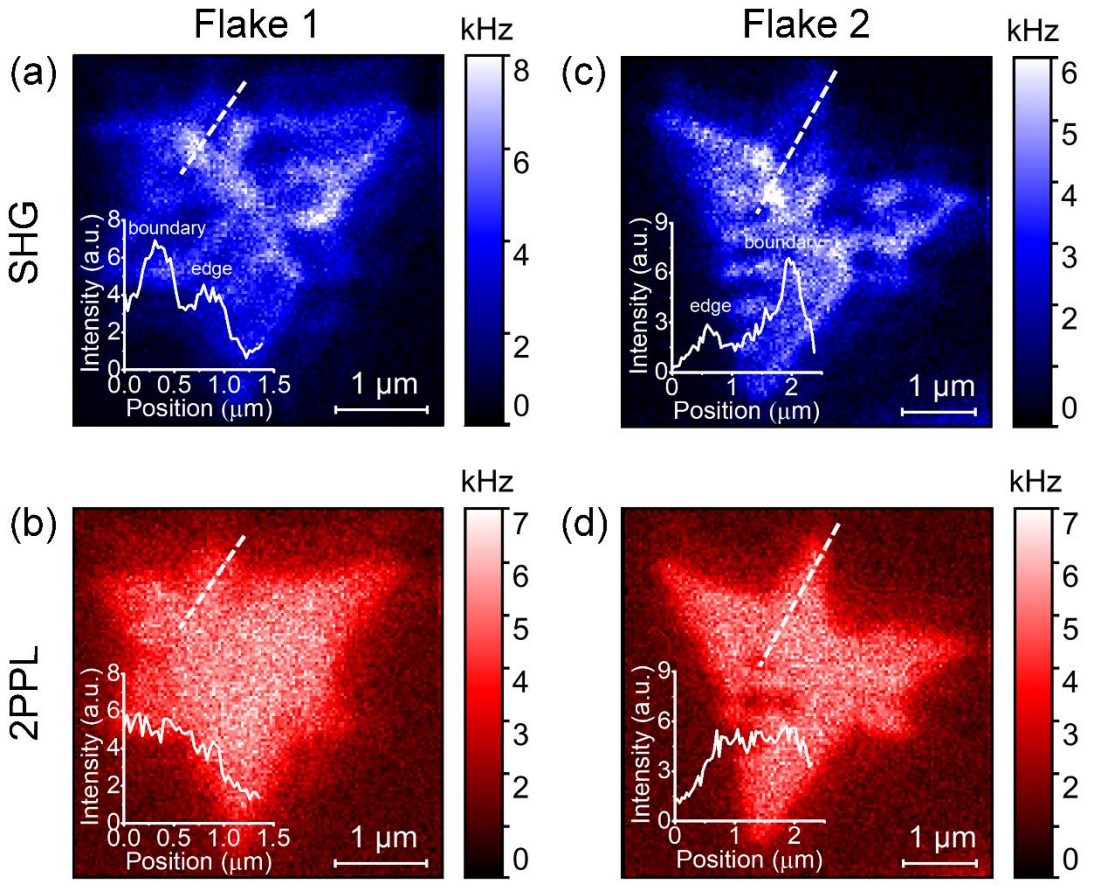

Figure 4.5: The visualization of grain boundaries and edges in two different $MoSe_2$ flakes.

(a) SHG and (b) 2PPL images of $MoSe_2$ flake 1. (c) SHG and (d) 2PPL images of $MoSe_2$ flake 2. The insets in (a) and (c) depict the cross sections of SHG intensity. The insets in (b) and (d) depict the cross sections of 2PPL intensity. The dashed white lines denote the positions where the cross sections are obtained.

4.5 Conclusion

In conclusion, the local structure properties of atomically thin $MoSe_2$ flakes have been investigated by SHG and 2PPL signals. The 2PPL peak maxima at ~2.30 eV and at ~2.38 eV could be assigned to the A' exciton and B' exciton transitions of $MoSe_2$ flake, respectively. The crystal orientations of discrete $MoSe_2$ flakes are determined by the polarization-dependent SHG intensity. We observed the differences in the angle 3θ which is defined as the angle between the generated SH electric field and the laser electric field, which experimentally indicates the different crystal orientations of discrete $MoSe_2$ flakes. The SHG response is sensitively related to the crystalline structure of $MoSe_2$ flake, which has been proved by a high SHG intensity observed at the grain boundaries and edges within a $MoSe_2$ flake.

Chapter 5 Local structural properties at the surface of $MoSe_2$ flake

5.1 Introduction

TMDCs materials and graphene have become promising candidates for unraveling chemical enhancement mechanism.[138, 139] Recently, the enhanced Raman signals of molecules on the plasma-treated MoS_2 were observed by modifying the symmetry of Raman molecules, which was through the interaction with local dipoles in treated MoS_2.[140] In addition, through the enhanced charge transfer resonance and exciton resonance, the Raman enhancement factor up to 100000-fold on oxygen incorporation in MoS_2 as compared to that on oxygen-unincorporated MoS_2 has been achieved.[121] It was also reported that cobalt phthalocyanine molecular orientation can contribute to the Raman spectral changes on the substrate of nanospheres coated gold film.[67] All in all, both local structural properties at the surface substrate and orientation of Raman probes play the crucial roles in the Raman enhancement process. Therefore, it is important to investigate the dependency of local structural properties on the chemical enhancement at the TMDCs monolayer surfaces.

In this chapter, a triangle-shaped $MoSe_2$ flake that is grown by a CVD process is used as a SERS platform. The Raman enhancement on $MoSe_2$ flake is investigated by coating a 5 nm of CuPc molecule film onto the surface of $MoSe_2$ flake by thermal vapor deposition. Excited by the azimuthally and radially polarized laser beams, the polarization- and local structure-dependent Raman enhancement on $MoSe_2$ flake are demonstrated and discussed. More

importantly, the structural irregularities properties in $MoSe_2$ flake are investigated by SHG microscopy together with PL microscopy. These results contribute to understand the impacts of local structural properties on the Raman enhancement at the surface of TMDCs materials.

The result of this chapter has been published:

Lin Pan, Peng Miao, Anke Horneber, Alfred J. Meixner, Pierre-Michel Adam, and Dai Zhang. Revealing local structural properties of an atomically thin $MoSe_2$ surface using optical microscopy. *Beilstein Journal of Nanotechnology*, **2022,** 13, 572-581.

5.2 Structural characterization of CuPc/$MoSe_2$

The triangular $MoSe_2$ flake was chemically synthesized on a 300 nm SiO_2/Si substrate. Due to the larger cross section of Raman scattering and no luminescence signal of CuPc molecule, the molecule is used as the Raman probe for investigating the Raman enhancement on the triangular $MoSe_2$ flake. A 5 nm of CuPc molecular film is deposited on the $MoSe_2$ flake substrate through thermal vapor deposition. Figure 5.1(a) shows the bright-field optical image of the triangular $MoSe_2$ flake covered with a 5 nm of CuPc thin film (CuPc/$MoSe_2$). The chemical structure of CuPc molecule is exhibited in Figure 5.1(b). As shown in Figure 5.1(a), the flake thickness can be estimated from the optical contrast, and the more transparent region of $MoSe_2$ flake is thinner compared to other regions.

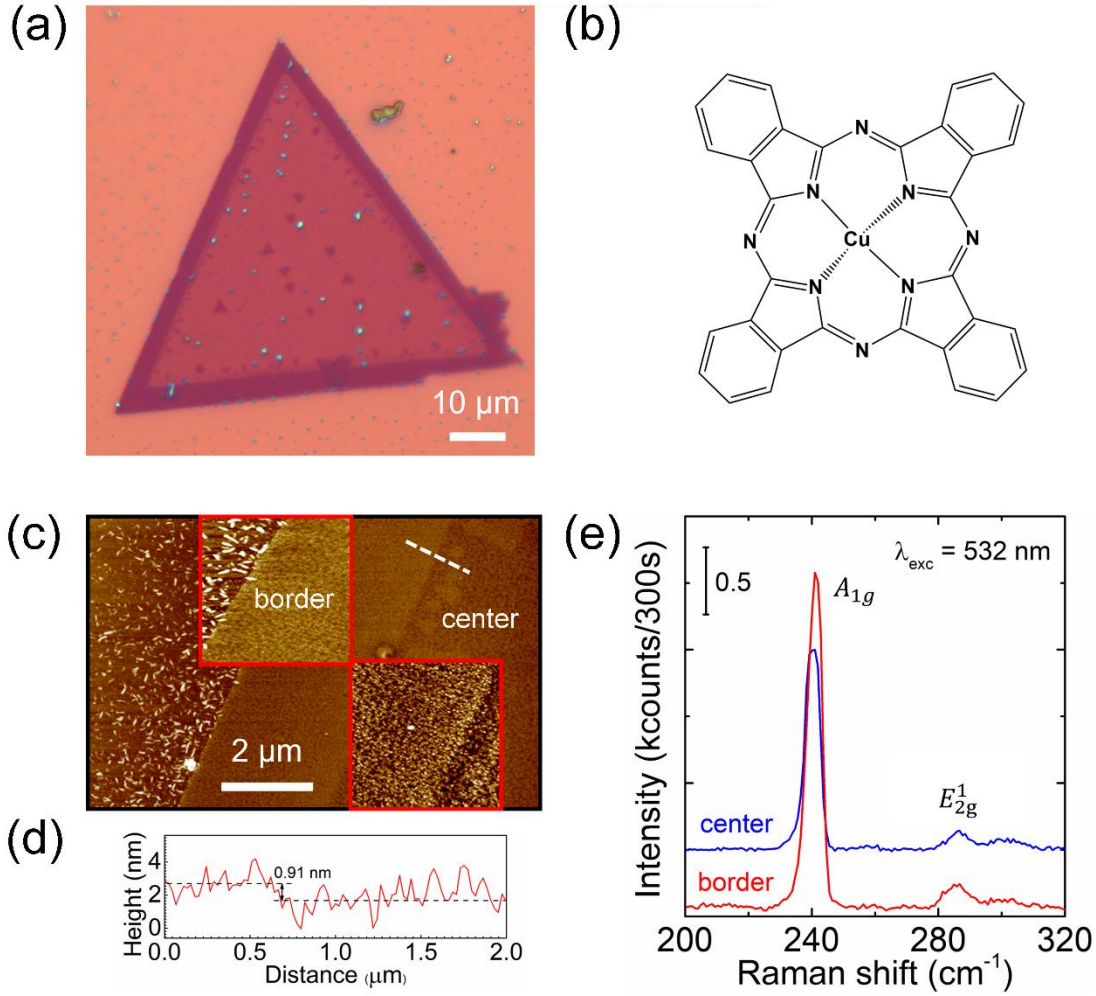

Figure 5.1: The structural and optical characterization of triangular $MoSe_2$ flake covered with a 5 nm of CuPc thin film (CuPc/$MoSe_2$).

(a) Bright-field optical image of CuPc/$MoSe_2$. (b) Chemical structure of CuPc molecule. (c) Topographical image of CuPc/$MoSe_2$. The right and left insets in (c) are the high-resolution topographical images measured from the SiO_2/Si substrate to the border of $MoSe_2$ flake and from the border to the center of $MoSe_2$ flake, respectively. (d) Height profile of CuPc/$MoSe_2$. The dashed white line in (c) indicates the position where the height profile is obtained. (e) Two Raman spectra from the border and the center regions of $MoSe_2$ flake excited by a 532 nm CW laser.

The AFM topographical image of CuPc/$MoSe_2$ is shown in Figure 5.1(c). The high-resolution AFM images (size: 2 × 2 μm) scanned from the SiO_2/Si substrate to border of $MoSe_2$ flake and from the border to center of $MoSe_2$ flake are exhibited in the right and left insets of Figure 5.1(c), respectively. It is observed that the $MoSe_2$ flake is fully covered with the CuPc molecule

aggregations. Some CuPc rod-like aggregates on SiO_2/Si substrate are observed, which is also reported in the previous literature.[139] The height profile measured from the border to center of $MoSe_2$ flake is taken from the dashed white line in Figure 5.1(c). From Figure 5.1(d), it confirms that the flake thickness is thinned from the border to center region of $MoSe_2$ flake. Figure 5.1(e) shows the Raman spectra obtained from the border and center regions of $MoSe_2$ flake using a 532 nm CW laser as an excitation source. An out-of-plane Raman mode at 240 cm^{-1} (A_{1g}) and another in-plane mode at 287 cm^{-1} (E_{2g}^1) are observed from the center of $MoSe_2$ flake, which can be determined to be a $MoSe_2$ monolayer.[129] At the border of $MoSe_2$ flake, two Raman modes A_{1g} and E_{2g}^1 shift to 241 cm^{-1} and 285 cm^{-1}, respectively, which agrees very well with Raman modes of $MoSe_2$ bilayer.[130]

Crystal stacking of the $MoSe_2$ flake is explored by SHG microscopy and spectroscopy by using a 780 nm femtosecond pulsed laser as an excitation source. As shown in Figure 5.2(a), the dashed white triangular denotes the real size of the $MoSe_2$ flake. We barely observe the SHG intensity at the border of $MoSe_2$ flake. In Figure 5.1(a), it is seen that some small triangular $MoSe_2$ flakes locate at the center region of large $MoSe_2$ flake, which shows dark in the SHG image in Figure 5.2(a). Three SHG spectra measured at three different positions are shown in Figure 5.2(b). The blue, red, and green stars in Figure 5.2(a) denote the positions where the SHG spectra are taken. The peak position of SHG spectra situates at 390 nm. The SHG intensity at the border is significantly lower than that at the center of $MoSe_2$. The SHG intensity shows a clear decrease as increasing of flake thickness, revealing a mirrored orientation of neighboring layers in this $MoSe_2$ flake, which is typical for a hexagonal 2H-phase $MoSe_2$ flake.[115, 141]

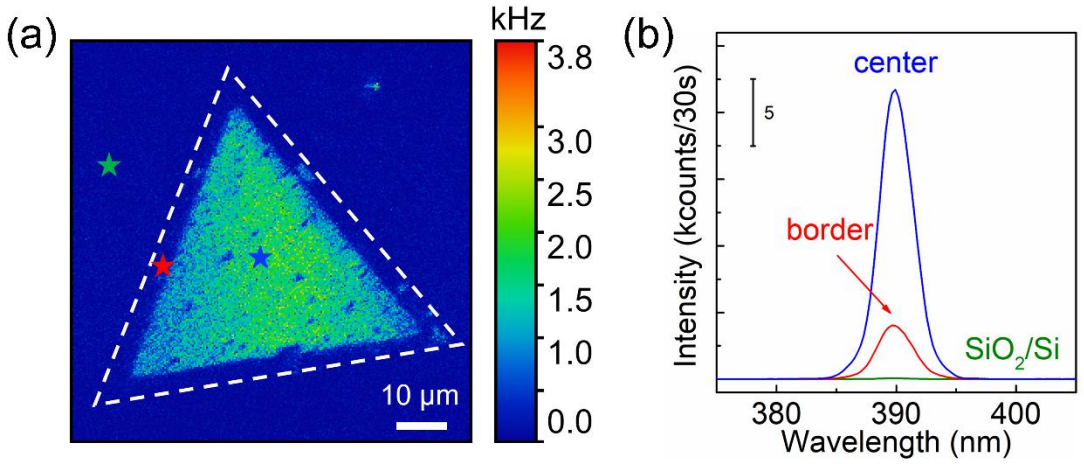

Figure 5.2: The SHG characterization of $CuPc/MoSe_2$.

(a) SHG image of $CuPc/MoSe_2$ excited by a 780 nm femtosecond pulsed laser. The dashed white triangular denotes the size of $MoSe_2$ flake. (b) shows three SHG spectra of the border and center of $MoSe_2$ flake, as well as SiO_2/Si substrate. The blue, red, and green stars in (a) represent the positions where the SHG spectra are taken at the center of $MoSe_2$ flake, border of $MoSe_2$ flake, and SiO_2/Si substrate, respectively.

5.3 Raman enhancement on $MoSe_2$ monolayer

Figure 5.3(a) shows the absorption spectrum of a 10 nm of CuPc molecular film that is deposited onto the surface of glass substrate by using thermal vapor deposition. The CuPc thin film exhibits a Q-band absorption in the visible region from 500 nm to 800 nm. One absorption peak located at 627 nm and another absorption peak situated at 696 nm are attributed to second and first π-π* transition of the phthalocyanine macrocycle, respectively.[142] Therefore, the Raman measurements are performed by a confocal optical microscopy coupled with a 636 nm CW laser, because the laser wavelength is in good resonance with the CuPc molecular absorption. To probe the polarization-dependent Raman signals on $CuPc/MoSe_2$, higher-order laser modes namely azimuthally, and radially polarized doughnut modes are used. Figure 5.3(b) and (c) exhibit the calculated electric field intensity distribution in the x-y plane in the focus of radial and azimuthal polarization, respectively. The focused radial polarization

beam shows dominantly $|E_z|^2$ component, which is about 14 times stronger than the $|E_{x,y}|^2$ component.[94] In contrast, azimuthal polarization in the focus only has $|E_{x,y}|^2$ component.[92, 97]

Figure 5.3(d) and (e) show the optical images of CuPc/$MoSe_2$ under a radially and an azimuthally polarized laser beam, respectively. The optical intensities in the image of Figure 5.3(d) and (e) contain the PL signal from $MoSe_2$ flake and Raman scattering signal of CuPc molecules. The CuPc/$MoSe_2$ excited under radial polarization gives a stronger optical intensity than that under azimuthal polarization, and the optical intensity at the border of $MoSe_2$ flake is weaker than that at the center of $MoSe_2$ flake. Figure 5.3(f) shows the Raman spectra that are measured at the center region of CuPc/$MoSe_2$ under a radially and an azimuthally polarized laser beam. Figure 5.3(g) illustrates the Raman spectra obtained at three different regions of CuPc/$MoSe_2$ substrate, and exact positions marked by blue, red, and green stars can be seen in Figure 5.3(d) and (e). The background of Raman spectra has been subtracted. The CuPc Raman intensity under radial polarization is stronger than that under azimuthal polarization as shown in Figure 5.3(f). Taking the 1527 cm^{-1} Raman mode as an example, the integrated Raman intensity using the radial polarization is nearly 1.75 times stronger than that using azimuthal polarization. As shown in Figure 5.3(g), integrated Raman intensity of CuPc Raman mode (1527 cm^{-1}) collected from the central region of CuPc/$MoSe_2$ is strongest, which is nearly 3 times higher than it is on SiO_2/Si substrate. Moreover, the Raman intensity obtained at the center of CuPc/$MoSe_2$ is slightly higher compared to that at the border of CuPc/$MoSe_2$.

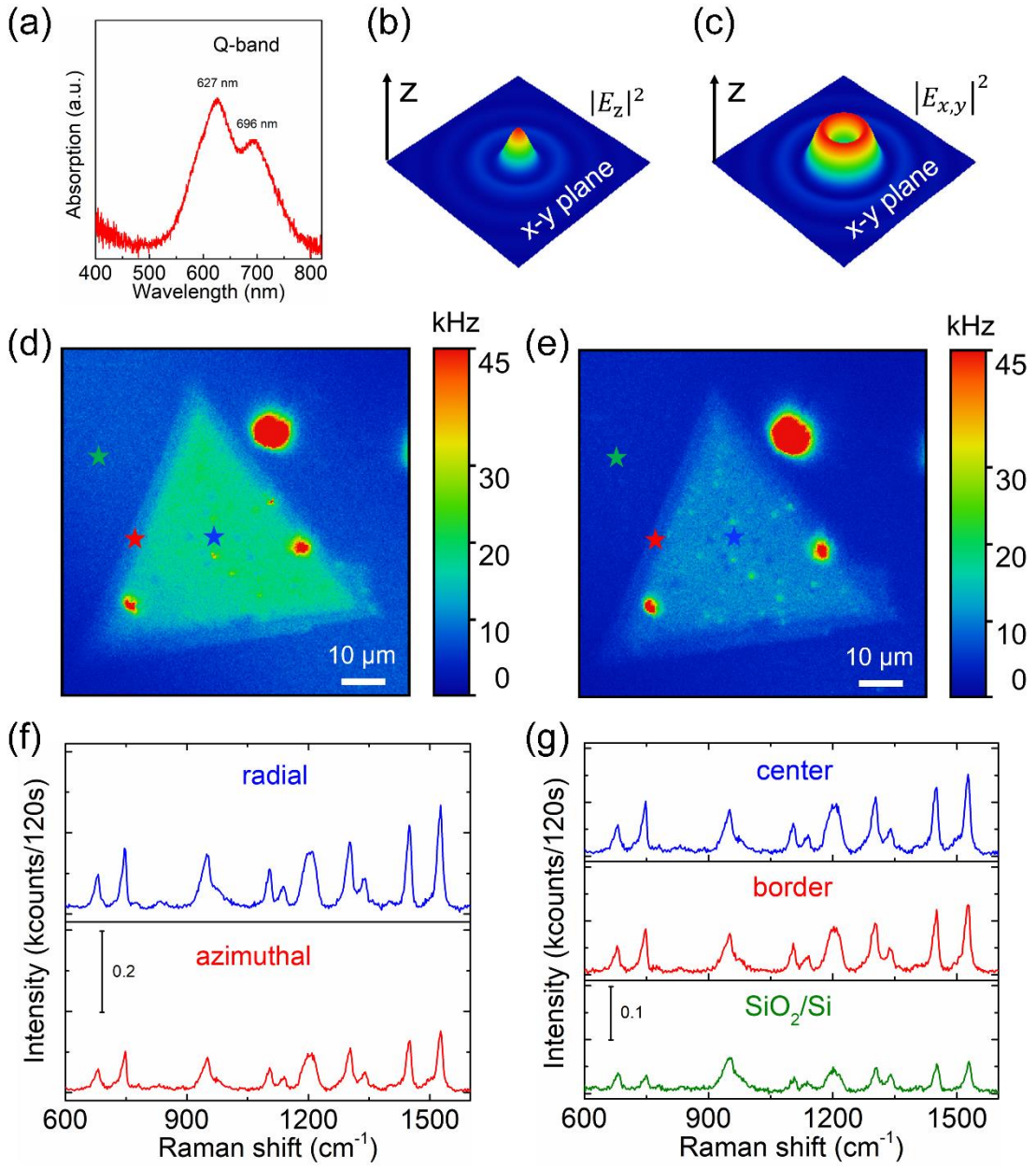

Figure 5.3: The Raman enhancement on the triangle-shaped $MoSe_2$ flake.

(a) Absorption spectrum of CuPc thin film with a thickness of 10 nm on the glass substrate. (b) and (c) show the calculated electric field intensity distribution in the x-y plane in the focus of radial and azimuthal polarization, respectively. (d) and (e) show the optical images of CuPc/$MoSe_2$ obtained with the radial and azimuthal polarizations, respectively. The blue, red, and green stars in (d) and (e) denote the positions where the Raman spectra are taken at the center of $MoSe_2$ flake, border of $MoSe_2$ flake, and SiO_2/Si substrate, respectively. (f) Raman spectra measured from the center of CuPc/$MoSe_2$ under radial and azimuthal polarization. (g) Raman spectra measured at three regions of CuPc/$MoSe_2$ using azimuthal polarization.

5.4 Dependency of Raman enhancement on polarization

Figure 5.4 shows the relative Raman enhancement factor on $MoSe_2$ monolayer under radial and azimuthal polarization. The enhancement factor is calculated by comparing the Raman intensity (integration of Raman peak area) of CuPc molecule at the central region of CuPc/$MoSe_2$ with that on SiO_2/Si substrate. The Raman enhancement factors of different Raman modes are different, ranging from 1.1 to 3.5, excited by both radial and azimuthal polarization. Although CuPc Raman intensity through excitation of the radial polarization is stronger (e.g., Raman mode at 1527 cml^{-1}) compared to that by using azimuthal polarization, the enhancement factor of each Raman mode under azimuthal polarization is higher than that under radial polarization. Herein eight Raman modes (681, 745, 1105, 1138, 1302, 1339, 1449, and 1527 cm^{-1}) can be assigned.[66, 71, 143] Table 1 shows the experimental Raman peaks of CuPc molecule and corresponding assignments.

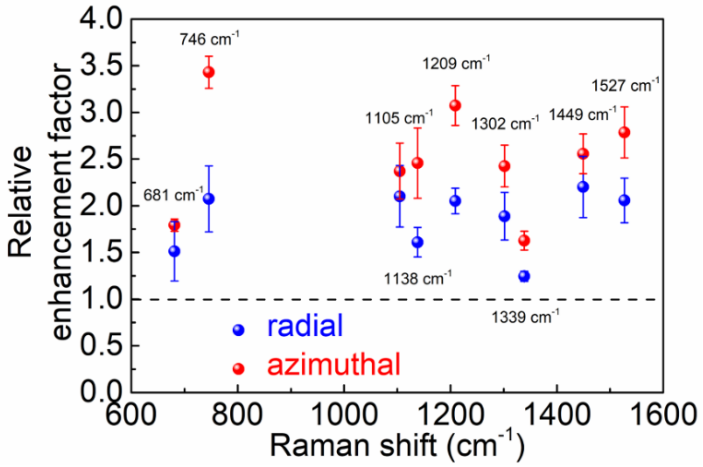

Figure 5.4: The comparison of relative Raman enhancement factor on $MoSe_2$ monolayer under a radially and an azimuthally polarized laser mode. The enhancement factor is calculated by dividing the CuPc Raman intensity at the center of CuPc/$MoSe_2$ by that on SiO_2/Si substrate.

As reported in the previous literature,[138] by using the graphene as the SERS platform, the Raman modes at 1342 cm^{-1}, 1452 cm^{-1}, and 1531 cm^{-1} of CuPc

monolayer have the largest Raman enhancement factor when compared to other Raman modes, which is due to the pronounced charge-transfer process between CuPc molecule and graphene. On the other hand, the Raman modes located at 749 cm^{-1}, and 1143 cm^{-1} of CuPc molecule are significantly enhanced using the hexagonal boron nitride (h-BN) as the substrate, which is benefitting from these Raman modes showing large dipoles, further leading to an efficient dipole-dipole interaction with the h-BN substrate. Here in our work, the CuPc Raman modes of 746 cm^{-1}, 1138 cm^{-1}, 1339 cm^{-1}, 1449 cm^{-1}, and 1527 cm^{-1} on the $MoSe_2$ monolayer are all enhanced when compared to that on the SiO_2/Si substrate, and the $MoSe_2$ monolayer is a direct bandgap semiconductor and has a polar covalent bond (Mo-Se). Therefore, both charge-transfer process and dipole-dipole interaction in CuPc/$MoSe_2$ heterostructure can possibly happen.

Table 1: The experimental CuPc Raman peaks and the corresponding assignments in CuPc molecule.

experimental peak (cm^{-1})	mode assignment
681	in plane full symmetric non-metal bound N-M stretch and isoindole ring stretch
746	in plane ring symmetric metal bound N-M stretch
1105	in plane symmetric N-M-N bend
1138	in plane ring symmetric and isoindole ring breathing
1209	
1302	in plane symmetric isoindole ring rotation
1339	in plane full symmetric N-C stretch and ring C-C stretch
1449	in plane ring symmetric isoindole ring C-C stretch
1527	in plane ring symmetric non-metal bound N-C stretch and ring C-C stretch

Furthermore, these interactions on CuPc/$MoSe_2$ heterostructure can be more efficient when the $|E_{x,y}|^2$ component of azimuthal polarization is used. To explain this result, the CuPc molecular orientation at the $MoSe_2$ surface will be

considered. The CuPc molecule that is deposited at the MoS_2 surface through thermal vapor deposition shows a face-on orientation, because the Cu metal center could link to the sulfur atom of MoS_2 via axial coordination.[144] We attribute the high SERS enhancement with the azimuthal polarization to the first-layer effect, where the charge-transfer process can be more pronounced between the first layer face-on oriented CuPc molecule and the $MoSe_2$ surface. As an increase of CuPc layer thickness, the CuPc molecular orientation can change, such as CuPc molecule showing a tilt angle with respect to the sample surface. Such CuPc molecular orientation evolution is observed in the iron phthalocyanine (FePc) thin film deposited on a MoS_2 crystal surface, where the FePc molecule is predominantly lying on the surface of MoS_2 and with the increasing of film thickness (more than 4.5 nm) the FePc molecules adopt a small tilt angle with respect to the sample plane.[145] Here in this study, CuPc molecules give a higher Raman intensity under radial polarization than that under azimuthal polarization, because the tilt CuPc molecules are excited under radial polarization, where it mainly shows $|E_z|^2$ component in the laser focus.

A comparison of PL spectra measured at the border (bilayer) and center (monolayer) of CuPc/$MoSe_2$ with radial and azimuthal polarization is shown in Figure 5.5(a). The PL peak located at ~790 nm is attributed to the exciton emission from the $MoSe_2$ monolayer.[130] Due to the thickness-dependent PL properties of $MoSe_2$, we observe from Figure 5.5(a) that the PL intensity measured at the border of CuPc/$MoSe_2$ (bilayer) is significantly lower than that at the central region of CuPc/$MoSe_2$ (monolayer) for both two polarizations. In addition, the PL intensity under radial polarization is stronger than that under azimuthal polarization for both monolayer and bilayer $MoSe_2$. The PL peak area ratio (I_{rad}/I_{azi}) can be calculated by dividing PL intensity spectrally integrated from 750 nm to 1000 nm under azimuthal polarization by that under radial polarization. The ratio on the monolayer $MoSe_2$ is 1.63, while the ratio on the bilayer $MoSe_2$ is 1.49.

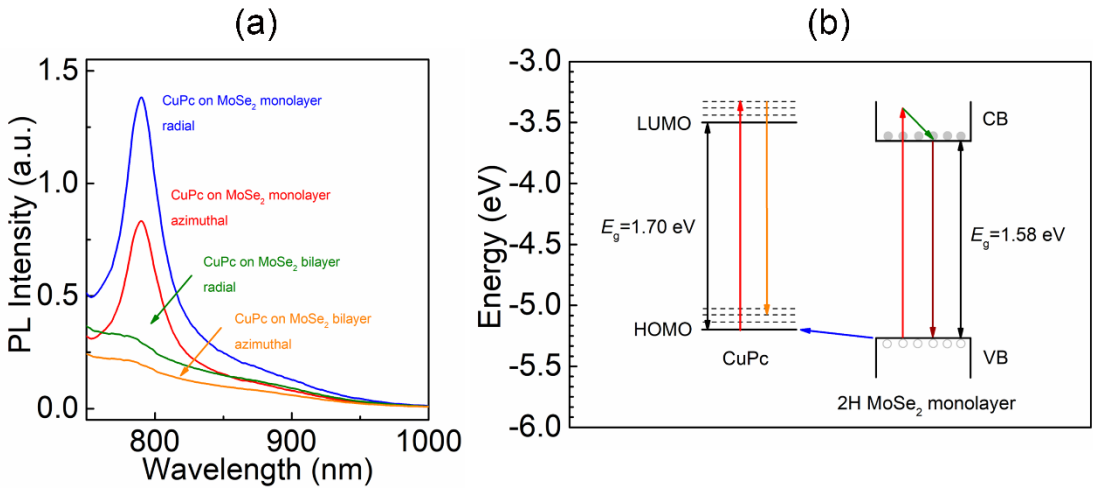

Figure 5.5: The enhancement mechanism between CuPc molecule and $MoSe_2$ monolayer.

(a) PL spectra measured at the border (bilayer) and center (monolayer) regions of CuPc/$MoSe_2$ under radial and azimuthal polarizations. (b) Energy level diagram at the interface between CuPc molecule and 2H $MoSe_2$ monolayer. The blue arrow indicates the ground-state charge-transfer process from $MoSe_2$ monolayer to CuPc molecule. Left side: the HOMO-LUMO transition of CuPc molecule is represented by the red arrow. The yellow arrow denotes the Raman scattering process. Right side: the optical absorption process is shown by the red arrow. Non-radiative relaxation process is indicated by the olive arrow. The wine-red arrow denotes the PL emission in $MoSe_2$ monolayer.

Based on the above results and discussion, the chemical enhancement mechanism at the interface between CuPc molecule and $MoSe_2$ monolayer is illustrated, as shown in Figure 5.5(b).[66, 130, 146, 147] Excited with a 636 nm CW laser, the electrons can migrate from the highest occupied molecular orbital (HOMO) to the lowest unoccupied molecular orbital (LUMO) of CuPc molecule, leading to the formation of hole in the HOMO, which is expressed by the red arrow seen in the left side of Figure 5.5(b). Due to the first-layer effect, we find that the charge-transfer process can be more efficient with an excitation of azimuthal polarization laser beam. In this case more electrons in the valence band (VB) of $MoSe_2$ monolayer can be involved the CuPc Raman scattering process, which can be demonstrated by the ground-state charge-transfer process (blue arrow), therefore the Raman scattering can be more enhanced under azimuthal polarization as denoted by the yellow arrow.[66, 77] Then, less

electrons can be excited from VB to conduction band (CB) of $MoSe_2$ monolayer as shown by the red arrow seen in the right side of Figure 5.5(b), which induces the radiative electron-hole pair recombination (wine-red arrow) is weaker than it is under the radial polarization, thus, the PL intensity is low with azimuthal polarization as shown in Figure 5.5(a). Furthermore, the ratio (I_{rad}/I_{azi}) on the monolayer $MoSe_2$ is higher than that on the bilayer $MoSe_2$, which indicates the ground-state charge-transfer process between CuPc molecule and $MoSe_2$ monolayer is more pronounced compared to that between $MoSe_2$ bilayer and CuPc molecule.

In general, Raman scattering process involves three steps: the incident light firstly interacts the electron in the ground state, then the electron in the excited state couples to the phonon (vibrational mode), eventually scattering light radiation. Both the charge-transfer process and dipole-dipole interaction contribute positively to the electron-phonon coupling in the Raman scattering process.[66] The HOMO of CuPc molecule is in the vicinity of the VB of $MoSe_2$ monolayer shown in Figure 5.5(b), and the 18 delocalized π electrons in the first-layer face-on lying CuPc molecule can overlap with the electrons cloud of $MoSe_2$ monolayer efficiently, which increases the electron density of states. The electron transition probability rate w_{lk} is expressed according to Fermi's golden rule as below:

$$w_{lk} = \frac{2\pi}{\hbar} g(E_k)|H'_{kl}|^2 \tag{5.1}$$

where the $g(E_k)$ denotes the density of states, and H'_{kl} indicates the matrix element of the LUMO-HOMO transition. In this case, as an increase of the density of states the electron transition probability can be increased, which plays an important key in the ground-state charge-transfer process, therefore enhancing the electron-phonon coupling and then increasing the Raman scattering process.[146]

In addition, due to the polar covalent bond (Mo-Se) in the presence of $MoSe_2$ monolayer, the interface dipole-dipole interaction between the face-on oriented CuPc molecule and $MoSe_2$ monolayer is induced.[139] The dipole-dipole interaction can give rise to a local symmetry related perturbation, which induces an increase of the matrix element of the LUMO-HOMO transition (H'_{kl}), further leading to a positive change of the electron transition probability.[138] In particular, the enhancement factor of Raman mode at 746 cm^{-1} under azimuthal polarization is larger than that with the radial polarization shown in Figure 5.4, because the Raman mode at 746 cm^{-1} is attributed to the metal bound N-M stretching vibration with a larger intrinsic dipole, further leading to a strong dipole-dipole interaction with the Mo-Se bond in $MoSe_2$ monolayer.

5.5 Revealing local structural properties of $MoSe_2$ flake

The optical image and SHG map (area size: 8 × 8 μm) scanned from the border to center region of CuPc/$MoSe_2$ are illustrated in Figure 5.6(a) and (b), respectively. Both Raman scattering of the CuPc molecules and PL signal of the $MoSe_2$ flake are collected in the optical intensities shown in Figure 5.6(a). The optical intensities seen in Figure 5.6(a) can apparently correlate with the SHG intensities shown in Figure 5.6(b), which is clearly observed from the region marked by the dashed red circles in Figure 5.6(a) and (b). The AFM topographical image of the corresponding region of CuPc/$MoSe_2$ is shown in Figure 5.6(c). We find that the surface of the area of CuPc/$MoSe_2$ is partially covered by some nanoparticles marked by the dashed red circles, which have been reported to be the intermediate products formed in the process of $MoSe_2$ growth.[114] The oxidation byproducts are observed at the surface of $MoSe_2$ and SiO_2/Si substrate, which are shown by the small blue particles seen in Figure 5.1(a).

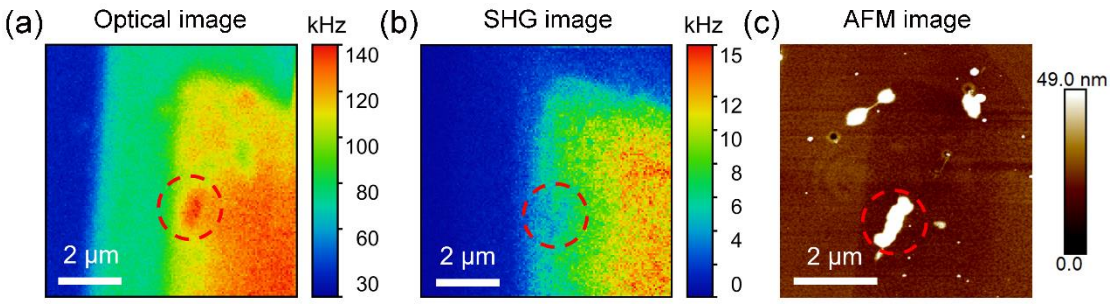

Figure 5.6: The comparison of optical image, SHG image, and AFM image of CuPc/$MoSe_2$.

(a) Optical image measured from the border to center region of CuPc/$MoSe_2$. Both Raman and PL signals are collected in the optical image. (b) SHG image of the corresponding region of CuPc/$MoSe_2$. (c) AFM topographical image for the same area of CuPc/$MoSe_2$.

Furthermore, 16 × 16 optical spectra from the corresponding region of CuPc/$MoSe_2$ are conducted by using the hyperspectral mapping technique. Figure 5.7(a) and (b) show the optical intensities mappings spectrally integrated from 750 nm to 850 nm and CuPc Raman peak area at 1527 cm^{-1}, respectively. Three regions at the border (R1), the border to center (R2), and the center (R3) are marked by the dashed black circles seen in Figure 5.7(a) and (b). In addition, a series of PL and Raman optical spectra are obtained from the three regions (R1, R2, and R3) shown in Figure 5.7(c) and (d), respectively. It is observed that PL intensity gradually increases from region R1 to R3 in Figure 5.7(a) and (c). Moreover, a 3 to 6 nm red-shift of photoluminescence peak position of region R2 is observable when compared to that of regions R1 and R3. On the other hand, the Raman intensity from region R2 is strongest than that from regions R1 and R3 in Figure 5.7(b) and (d). Based on the above results, we demonstrate that the SHG intensity, photoluminescence intensity and peak position, as well as Raman enhancement are sensitively relevant to the local structure properties of $MoSe_2$ flake.

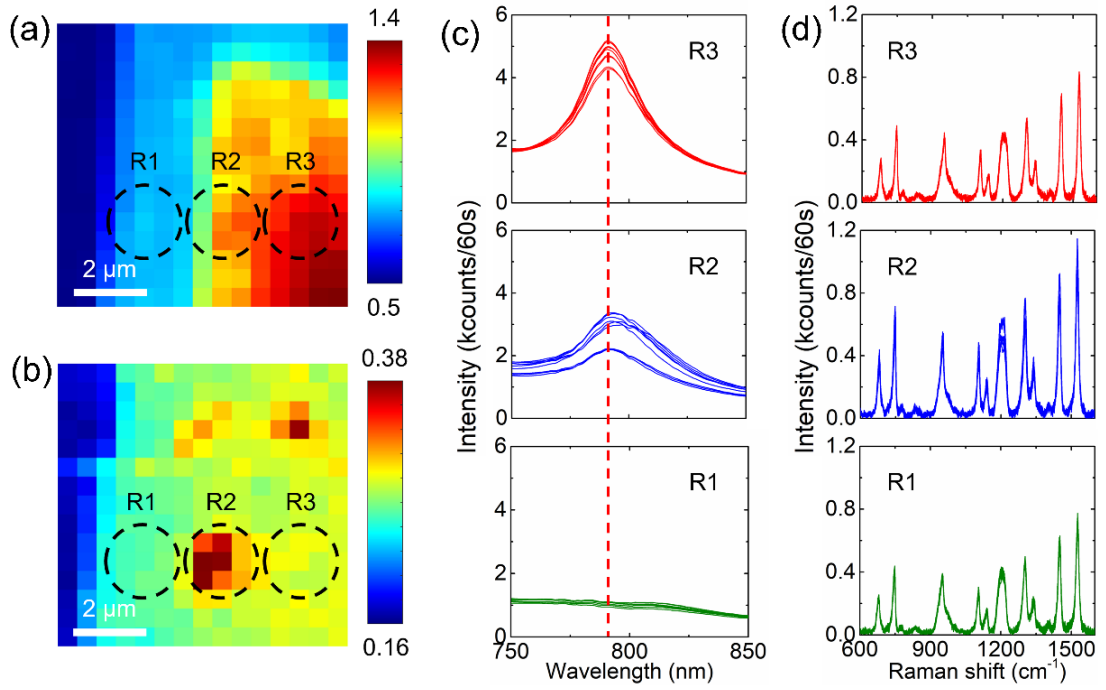

Figure 5.7: Local structure-related Raman enhancement on $MoSe_2$ flake.

(a) and (b) show PL and Raman mappings at the same region of CuPc/$MoSe_2$, respectively. The optical intensities in (a) are the integrated intensity of PL peak at 790 nm from $MoSe_2$ flake. The Raman peak at 1527 cm^{-1} of CuPc molecule is spectrally integrated for obtaining the Raman mapping. The color bar in (a) and (b) represents the integrated intensities. Both the Raman and PL mapping are measured under azimuthal polarization. (c) and (d) are a series of PL and Raman spectra obtained from three different regions of CuPc/$MoSe_2$, respectively. Three regions (R1, R2, and R3) are marked by black dashed circles as seen in the (a) and (b).

The lowest Raman intensity of CuPc molecule at region R1 is attributed to the bilayer property of $MoSe_2$ flake, which is proved by the vanished photoluminescence intensity (seen in Figure 5.7(c)) and A_{1g} vibrational mode located at a higher wavenumber (seen in Figure 5.1(d)). At the regions of the $MoSe_2$ monolayer, the stronger Raman intensity of CuPc molecule and weaker photoluminescence intensity of $MoSe_2$ flake at region R2 is observed than that at region R3, which is in good agreement with the ground-state charge-transfer process discussed above in Figure 5.5(b). In the AFM topographical image, the presence of intermediate products has been reported to be the oxidation products (MoO_xSe_y or MoO_3) either via the CVD growth process, or via the

aging effect in air. The oxidation product can be formed by exposing the tungsten diselenide (WSe_2) flake in air, which can induce a 2 to 4 nm red-shift of photoluminescence peak position when compared to the pristine flake. This phenomenon is possibly due to the formation of different states or strain in the presence of oxidation products.[126] In Figure 5.7, we observe a red-shift of photoluminescence peak maxima in the oxidation products, where high Raman intensity is obtained. This is interpreted by the formation of new energy states due to the presence of oxidated $MoSe_2$, which is sensitively indicated by the SERS effect.

5.6 Conclusion

In conclusion, with a combination of SHG, Raman and PL spectroscopies and microscopies, the local structure-related optical properties of the CuPc/$MoSe_2$ heterostructure have been demonstrated. The Raman enhancement on $MoSe_2$ monolayer under azimuthally polarized excitation is stronger than that under radially polarized excitation, which is mainly benefiting from the first layer effect, where the ground-state charge-transfer process and the dipole-dipole interaction between the face-on oriented CuPc molecules and $MoSe_2$ monolayer are more pronounced. More importantly, we demonstrate that structural irregularity properties at the surface of $MoSe_2$ flake are determined by both SHG and PL properties, and such local structure can also affect the Raman enhancement on $MoSe_2$ flake.

Chapter 6 Directional emission in DH-P-TTA thin molecule film

6.1 Introduction

The structural properties involving molecular orientation and structural ordering of organic semiconducting films have been considered as the crucial parameters influencing their optical and electrical properties.[3, 9] For example, it has been reported that the horizontal orientation of molecular emitters with respect to the substrate plane is beneficial for achieving a high efficiency of organic light-emitting diodes (OLED).[148] On the contrary, single-crystal molecular film has been proven to be an excellent candidate in organic field-effect transistors (OFET), which is resulted from their highly structural ordering and also the vertical orientation of molecules, then leading to enhance the charge carrier transport in OFET.[9, 149] For this reason, characterizing the structural properties of organic semiconductor film has become a critical subject for understanding their optical and electronic properties.

The k-space imaging microscopy can be used to directly visualize the emissive directionality;[150-154] hence has been applied to identify the molecular orientation in various materials.[87, 155, 156] Here in this chapter, we develop a k-space imaging microscopy coupled with a 780 nm femtosecond pulsed laser, which is an update our home-built parabolic mirror-assisted confocal optical microscope. The angular emission patterns of an ultrathin film of DH-P-TTA molecule (tetrathienoacene as the central core end-capped with 4-hexyl-1-(4,4,5,5-tetramethyl-1,3,2-dioxaborolan-2-yl) benzene) deposited on SiO_2/Si substrate are probed with the k-space imaging microscopy. We investigate the sample

location- and layer thickness-dependent emission directionalities in DH-P-TTA thin molecule films. In addition, the optical image and spectral response of DH-P-TTA films are measured as well. The molecular orientations within the DH-P-TTA films are discussed based on the experimental results together with calculated emission patterns. These results contribute to study the impacts of molecular orientations on the optical properties of novel organic semiconducting materials.

6.2 Optical characterization of DH-P-TTA thin film

The chemical structure and schematic orientation of the DH-P-TTA molecule are illustrated in Figure 6.1(a). The DH-P-TTA films are prepared on the precleaned SiO_2/Si substrate via a solution-processed method combined with a slow solvent evaporation, which is provided by the collaboration partner Prof. Dmitry Yu. Paraschuk from Enikolopov Institute of Synthetic Polymetric Materials of Russian Academy of Science. The chemical structures of DH-P-TTA molecule (labelled by the dashed grey square) and tetrathienoacene (TTA) part (marked by the dashed red square) are illustrated in Figure 6.1(a). Ponomarenko et al have calculated the electronic structure of DH-P-TTA molecule using the density functional theory (DFT).[157] According to the DFT calculation, both highest occupied molecular orbital (HOMO) and lowest unoccupied molecular orbital (LUMO) of DH-P-TTA molecule are located mostly at the TTA part, mainly due to the repulsion between the phenyl and TTA hydrogens. Furthermore, the transition dipole moment of the molecule orients along the long axis of the molecule, as illustrated by the double-ended red arrow in Figure 6.1(a).

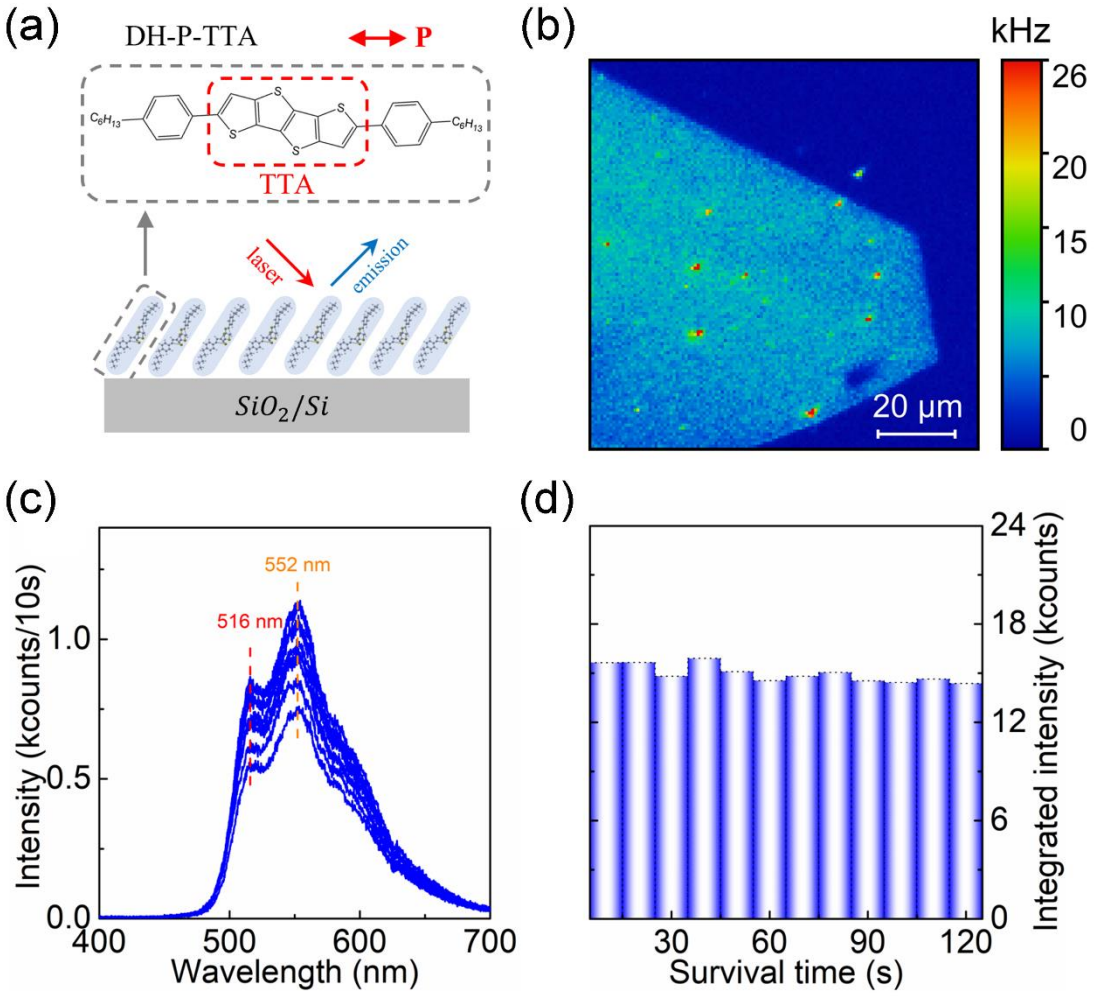

Figure 6.1: Nonlinear optical characterization of DH-P-TTA thin molecule film.

(a) Schematic drawing of the DH-P-TTA thin film prepared on SiO_2/Si substrate. The chemical structures of the DH-P-TTA molecule and TTA part are marked in the dashed grey and red squares, respectively. The transition dipole moment of the molecule is indicated by the double-ended red arrow. (b) Nonlinear optical image of the DH-P-TTA film. (c) Nine optical spectra measured from the different positions in (b). (d) The evaluation of the DH-P-TTA molecular photostability under the continuous irradiation of pulsed laser.

The nonlinear optical properties of DH-P-TTA film are obtained via a confocal microscopy coupled with a 780 nm femtosecond pulsed laser. We perform optical data acquisition by first obtaining a scanning confocal image together with the spectral response and then acquiring the angular emission pattern.

Figure 6.1(b) shows the nonlinear optical image that is taken from part of the DH-P-TTA film. From the height profile taken from the AFM measurements, we know the thickness of the DH-P-TTA film is rough ~4.68 nm. A homogeneous distribution of optical intensity is observed in Figure 6.1(b). The film exhibits a faceted shape, indicating its two-dimensional (2D) crystal properties.[157, 158] Figure 6.1(c) shows nine 2PPL spectra collected at different positions on the film shown in Figure 6.1(b). All the 2PPL spectrum shows two peak maxima located at ~516 nm and ~552 nm. Furthermore, the molecular photostability under the fs-laser pulse illumination is tested by continuously collecting spectrum at one sample position. The 2PPL intensity spectrally integrated from 450 nm to 700 nm is plotted against the illumination duration (survival time), as shown in Figure 6.1(d). No significant decrease of 2PPL signal is observed in Figure 6.1(d), which suggests a good photostability of the DH-P-TTA molecule within 120 s, which is adequate to image the angular emission pattern of DH-P-TTA molecule using the k-space imaging microscopy.

Now we turn to probe the angular emission patterns of DH-P-TTA thin film. As shown in Figure 2.5 in the Chapter 2.1.3 (Methods and materials), an extremely sensitive EMCCD is used to project the intensity distribution, and the full wave vector information of the emitting light. To optimize the signal-to-noise ratio, 4 × 4 hardware binning of the EMCCD pixels is used. Only 2PPL signal is collected by filtering out the elastically scattered light and each emission pattern is obtained with an exposure time of 120 seconds. The rim of the 2PPL emission pattern is determined according to the pattern from the elastically scattered light.

Figure 6.2(a) shows the emission pattern of DH-P-TTA thin film, which is measured on the film shown in Figure 6.1(b). Notably, the round-shaped pattern in the middle of the emission pattern is because of the one-arm sample holder that blocks part of the optical signal. Another reason for this dark region is the hole at the center of the parabolic mirror, which leads to the losing of signal

collection from 0-27 degrees vs. the optical axis. Each point in the pattern corresponds to an emission angle. Figure 6.2(b) shows the image plane information via a fast Fourier transform (FFT) of the emission pattern in Figure 6.2(a). The one-point pattern exhibited in Figure 6.2(b) suggests that focus in the emission pattern measurement is well located.

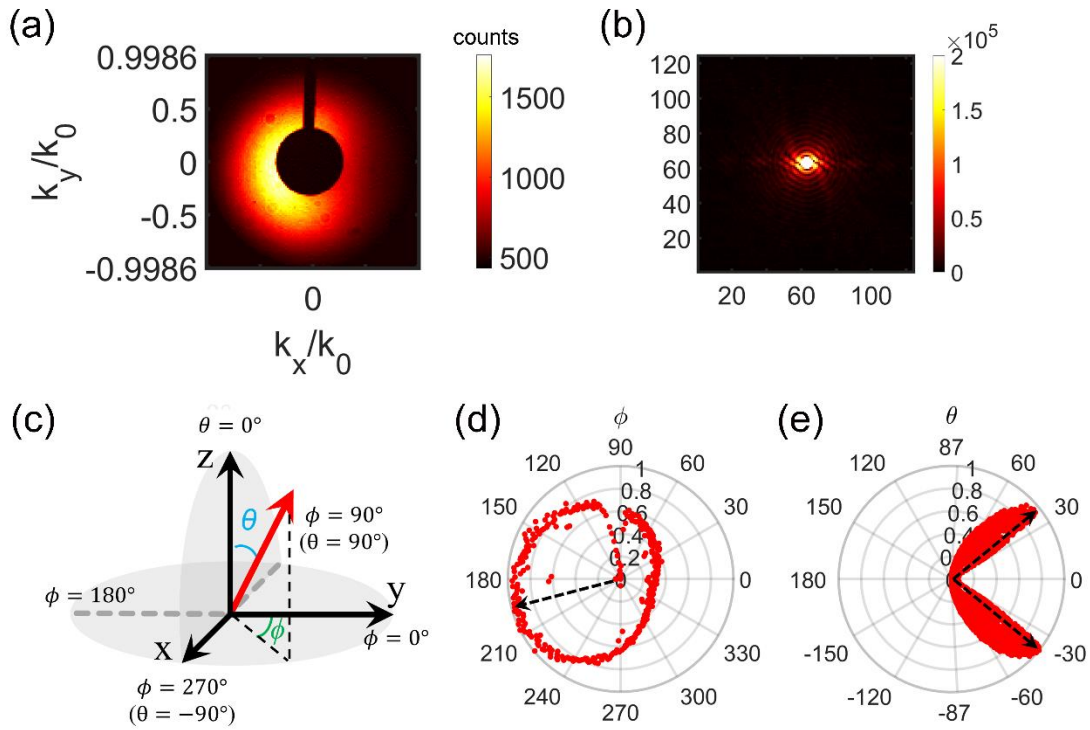

Figure 6.2: The directionality behavior of DH-P-TTA thin film.

(a) The experimental emission pattern collected from the DH-P-TTA thin film. (b) The fast Fourier transform (FFT) of the experimental emission pattern. The color bars represent the optical intensity. (c) The spherical angle ϕ, and θ defines the in-plane and out-of-plane emission direction, respectively. The red arrow indicates the emission direction. (d) The polar plot of the optical intensity as a function of the in-plane angle ϕ_{em}. (e) The polar plot of the optical intensity as a function of the out-of-plane angle θ_{em}. The in-plane angle ϕ_{em} varies from 0° to 360°, and the out-of-plane angle θ_{em} varies from 27° (-27°) to 87° (-87°) due to the geometry of the parabolic mirror.

To describe the emission direction, a spherical ϕ, θ-coordinate is introduced, as shown in Figure 6.2(c). The red arrow represents the emission direction. The emission direction $I(\phi_{em}, \theta_{em})$ can be defined by the in-plane angle ϕ_{em} and

the out-of-plane angle θ_{em}. Figure 6.2(d) and (e) show the polar plot of the 2PPL intensity as a function of the in-plane ϕ_{em} and the out-of-plane θ_{em}, respectively. In Figure 6.2(d), we can see that the in-plane ϕ_{em} is allowed to range from $0°$ to $360°$, and 2PPL intensity is mainly distributed at the left side that points toward an in-plane angle of $\phi_{em} = 195°$ as indicated by the dashed arrow, where the strongest emission can be seen. In Figure 6.2(e), the out-of-plane θ_{em} is only allowed to range from $27°$ ($-27°$) to $87°$ ($-87°$). The detail can be found in Chapter 2.1.3 (Methods and materials). The polar plot shown in Figure 6.2(e) reveals a prominent emission direction at $|\theta_{em}| = \sim 40°$ as marked by the dashed arrow, where the strongest intensity is observed.

6.3 Directional emission in two individual domains

Figure 6.3(a) shows the nonlinear optical image of a DH-P-TTA thin film that contains two individual domains. The AFM measurements are also conducted to compare their thicknesses. The results show that the upper domain has a thickness of ~5.22 nm, and the lower domain is ~6.47 nm thick. The spectral responses of these two domains are probed, as shown in Figure 6.3(b). For each domain, five 2PPL optical spectra are collected at different positions (a1-5 and b1-5). We observe two 2PPL peak maxima for all the spectra and no change in the 2PPL peak position within one domain. However, a shift of peak 2 is observed when comparing the spectra taken from the upper and the lower domains. The maximum position of peak 2 measured from the lower domain is shifted to a higher wavelength of ~552 nm when compared to that obtained from the upper domain (peak maximum at ~544 nm), while no shift of maximum position of peak 1 is observed. The red-shift of 2PPL peak is possibly attributed to the different molecular stacking behavior (*e.g.*, orientation, and order) within DH-P-TTA thin film. To address this phenomenon, the angular emission patterns of the two domains are measured and the experimental results are exhibited in Figure 6.4.

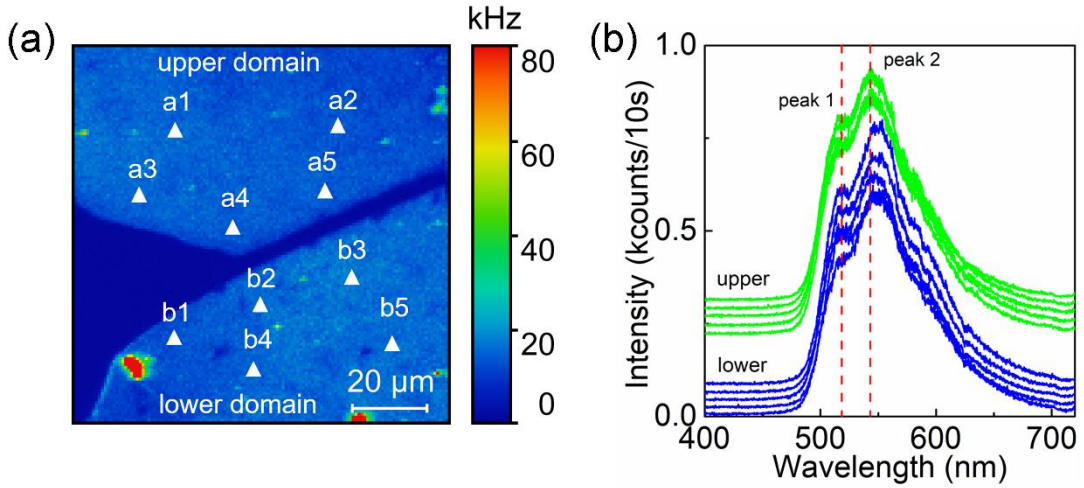

Figure 6.3: Nonlinear optical characterization of DH-P-TTA thin film.

(a) Nonlinear optical image of two individual domains. (b) The 2PPL optical spectra obtained at different locations (marked by a1-5 and b1-5 in (a)) of two domains.

For each domain, we measure five emission patterns at different positions (a1-5 and b1-5). To precisely compare the difference in emission directionality, the optical intensity as a function of the in-plane angle ϕ_{em} and the out-of-plane angle θ_{em} is also plotted in Figure 6.4(a) and (b). As shown in Figure 6.4(a), no significant difference in the distribution of optical intensity within the five experimental emission patterns is visible. The same observation is also shown at the lower domain in Figure 6.4(b). Interestingly, the emission patterns obtained from the two domains seem to be mirrored when comparing the upper and the lower domains. In detail, for the in-plane angle ϕ_{em}, the optical signal obtained from the upper domain points towards the left side at $\phi_{em} = 200°$; whilst the optical signal taken from the lower domain emits towards the right side at $\phi_{em} = 345°$. For the out-of-plane angle θ_{em}, a prominent emission direction at $|\theta_{em}| = \sim 36°$ of the upper domain is observed, which appear at $|\theta_{em}| = \sim 42°$ from the lower domain. The distinct directionality properties between the two separated domains of DH-P-TTA thin film indicate the different molecular orientations in the crystalline structure.

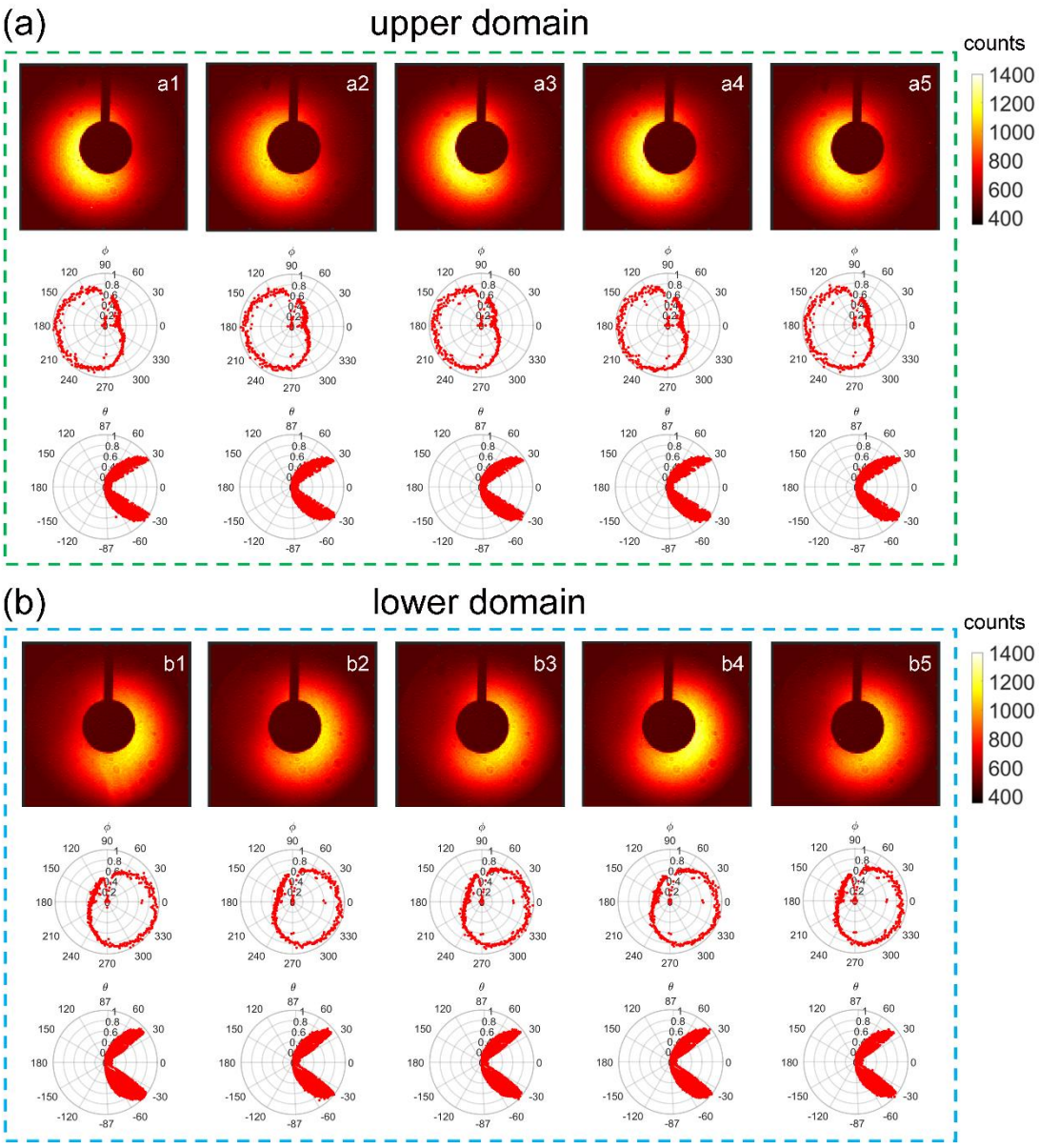

Figure 6.4: The directionality behavior obtained from two individual domains of DH-P-TTA film.

(a) and (b) exhibit the experimental emission patterns collected from five different positions from the upper and lower domains, respectively. The exact positions (a1-5 and b1-5) are marked in Figure 6.3(a). The color bar in (a) and (b) represents the optical intensity. The polar plots of the optical intensity versus in-plane angle ϕ_{em} and versus out-of-plane angle θ_{em} of the corresponding emission pattern are shown in (a) and (b). The upper and lower domains can be visualized in Figure 6.3(a).

To further address the underlying mechanism of emission directionality from the two domains, we extend the angular emission pattern measurements by adjusting the orientation of sample substrate.

The schematic drawings for adjusting the in-plane orientation (shown as 'Top view') and out-of-plane orientation (shown as 'Side view') of sample substrate are illustrated in Figure 6.5. The two DH-P-TTA domains are shown in blue, and the substrate rotation directions are indicated by the green arrows. After an in-plane rotation of the sample substrate, the angular emission patterns and the corresponding polar plots (optical intensity versus in-plane angle ϕ_{em}) from the upper and lower domains are exhibited in Figure 6.5(a). The optical signals from the upper and lower domains emit at in-plane angles at $\phi_{em} = 150°$ and at $\phi_{em} = 300°$, respectively. Comparing with the results in Figure 6.4, we conclude that the sample substrate is rotated roughly by an in-plane angle of $50°$. Furthermore, we tilt the sample substrate with a certain out-of-plane angle with respect to the optical axis (represented by z axis) and the resulted emission patterns from the two domains are displayed in Figure 6.5(b). We observe the emission direction from the upper domain at the out-of-plane angle $|\theta_{em}| < 36°$. However, we can't estimate the exact direction due to the presence of forbidden collection region (-27 degrees to 27 degrees) in the parabolic mirror. In addition, the lower domain exhibits an emission direction at $|\theta_{em}| = \sim 50°$, larger than the out-of-plane angle $|\theta_{em}| = \sim 42°$ shown in Figure 6.4(a), clearly suggesting the influences of tilted sample on the emission direction. In summary, Figure 6.4 and Figure 6.5 demonstrate that the emission directionality of the DH-P-TTA thin film is highly related to the molecular orientation, which is further proved by modifying the sample orientation.

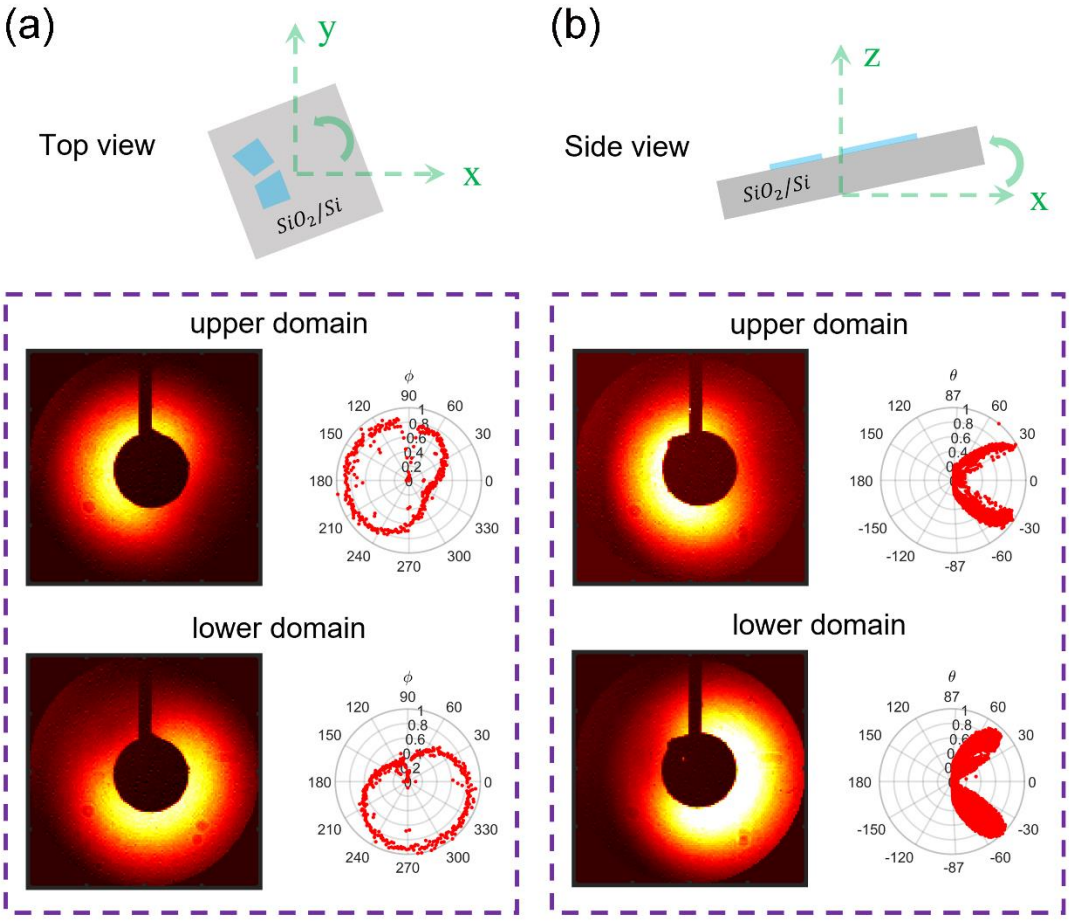

Figure 6.5: The emission directionality of DH-P-TTA thin film at different substrate orientations.

(a) Experimental emission patterns and the corresponding polar plots (the optical intensity as a function of the in-plane angle ϕ_{em}) from two domains by rotating the in-plane orientation of the sample substrate. (b) Emission patterns and the corresponding polar plots (the optical intensity versus the out-of-plane angle θ_{em}) by tilting the out-of-plane orientation of sample substrate. The simplified sketches for adjusting the orientation of the sample substrate are also shown in (a) and (b). The upper and lower domains can be seen in the nonlinear optical image in Figure 6.3(a).

6.4 Dependency of emission directionality on thickness

Now we extend to the optical measurements to reveal the thickness dependence of the 2PPL optical intensity and their angular emission patterns.

The nonlinear optical images of three regions of DH-P-TTA film are exhibited in Figure 6.6(a)-(c). The white dashed squares R1, R2, and R3 marked in Figure 6.6(a)-(c) represent the three domains of different thicknesses. From the AFM measurements, the layer thickness of R1, R2, and R3 is ~0.87 nm, ~33.0 nm, and ~58.18 nm, respectively. Figure 6.6(d) shows the spectral responses recorded from R1, R2, and R3. Two 2PPL peaks are observable from all three domains. The average of 2PPL intensities spectrally integrated from 450 nm to 700 nm for three domains are illustrated in Figure 6.6(e). The strongest intensity appears in the domain R3 and the weakest in the domain R1, indicating a clear film-thickness dependent 2PPL intensity.

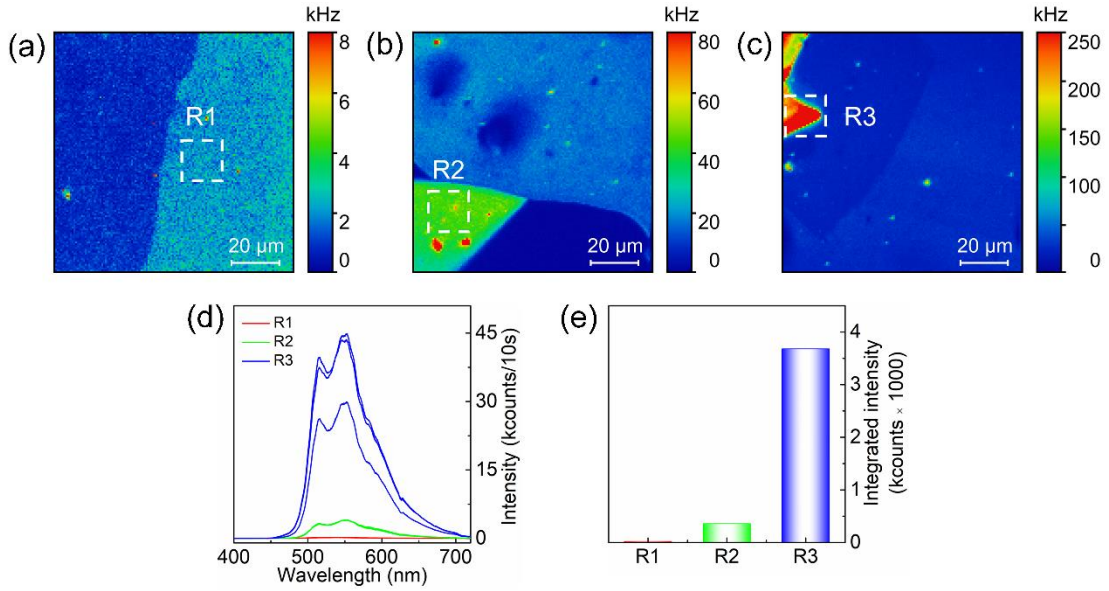

Figure 6.6: Dependency of 2PPL signal on thickness of DH-P-TTA thin film.

(a)-(c) The nonlinear optical images of three regions of DH-P-TTA film. The dashed white squares marked in (a), (b), and (c) represent the domains where the optical spectra and angular emission patterns are taken. The layer thickness of R1, R2, and R3 is ~0.87 nm, ~33.0 nm, and ~58.18 nm, respectively. (d) 2PPL optical spectra obtained from the three domains R1, R2, and R3. (e) The thickness dependence of the 2PPL intensity spectrally integrated from 450 nm to 700 nm.

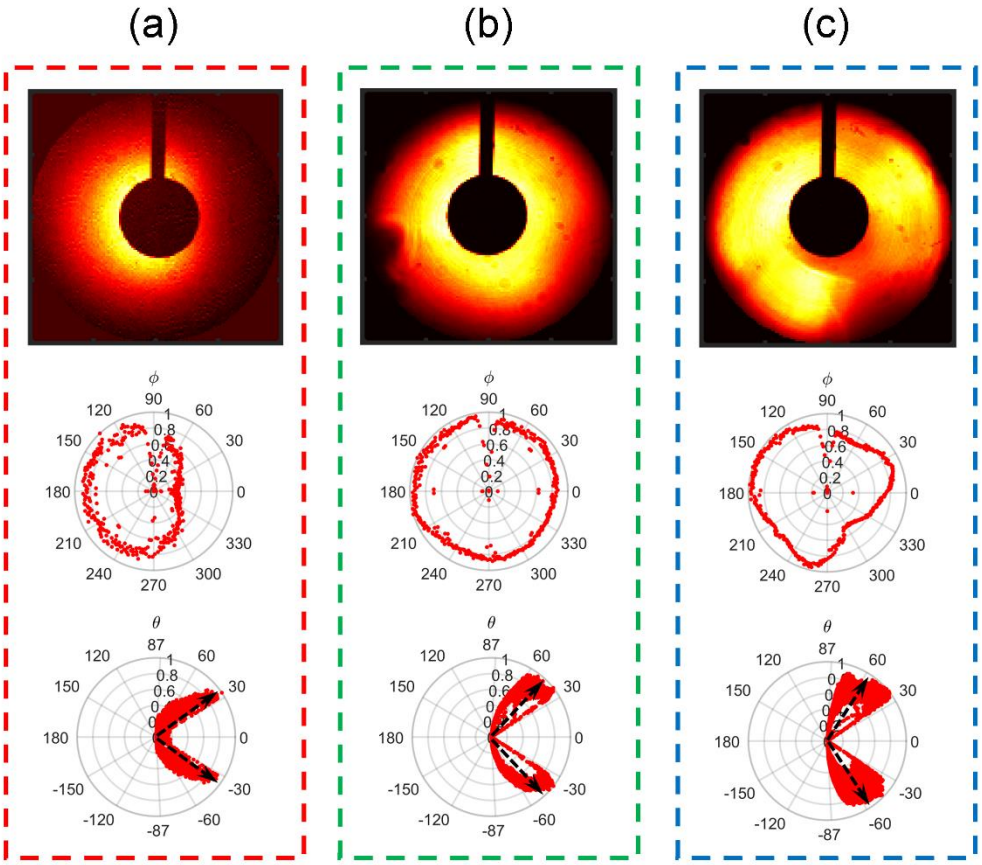

Figure 6.7: Dependency of emission directionality on thickness.

(a)-(c) The experimental emission patterns taken from the domains (marked in Figure 6.6) R1, R2, and R3, respectively. The corresponding polar plots of the optical intensity as the function of the in-plane angle ϕ_{em} and the out-of-plane angle θ_{em} are also shown in (a-c). The out-of-plane angle θ_{em} is indicated by the dashed arrow, where the strongest intensity is observed.

Figure 6.7(a), (b), and (c) show the angular emission patterns together with the corresponding polar plots (2PPL intensity versus in-plane angle ϕ_{em} and versus out-of-plane θ_{em}), that is measured from the respective domains R1, R2, and R3. In the domain R1 which has a thickness of ~0.87 nm, the 2PPL intensity dominantly distributes at the left side of the emission pattern, as seen in Figure 6.7(a). This pattern is similar to the emission direction from the domains with a thickness ranging from ~5 nm to ~10 nm, as seen in Figure 6.2 and Figure 6.4. From the corresponding polar plots as the function of the in-plane angle ϕ_{em} and the out-of-plane angle θ_{em}, one can see the emission direction points towards $\phi_{em} = 180°$ and $|\theta_{em}| = \sim 36°$. In contrast, with the

increase of the layer thickness such as in domains R2 and R3, the angular emission patterns are nearly isotropic. Now considering the out-of-plane angle θ_{em}, we find the domain R2 exhibits an emission direction at $|\theta_{em}| = \sim 45°$. As compared to the domain R2, the emission from the thicker domain R3 points toward an angle of up to $|\theta_{em}| = \sim 55°$, which is distinctly different from the out-of-plane emission angle ($|\theta_{em}| = \sim 36°$) observed in the ultrathin domain R1. The observed data obviously demonstrates that angular radiation properties are strongly correlated to the thickness of DH-P-TTA film.

6.5 Possible molecular orientation in DH-P-TTA thin film

To address the possible molecular orientation within DH-P-TTA thin film, we first calculate the angular emission patterns of a single molecule that is placed on the surface of SiO_2/Si substrate ($n_{air} = 1.0$, $n_{SiO_2} = 1.46$, $n_{Si} = 4.09$) and positioned in the focus of parabolic mirror. The used program is developed by Dr. Quan Liu from Institute of Theoretical and Physical Chemistry of Eberhard Karls University of Tübingen. Figure 6.8 shows the calculated emission patterns and the corresponding polar plots (optical intensity versus in-plane angle ϕ_{em} and versus out-of-plane θ_{em}) of single molecule with four different dipole orientations. The orientation of the single dipole (elementary Hertzian dipole) $P(\Phi_{dip}, \Theta_{dip})$ can be expressed by one in-plane angle Φ_{dip} and another out-of-plane angle Θ_{dip}. The spherical Φ, Θ-coordinate is exhibited in Figure 6.9(a). Figure 6.8(a) and (b) show the calculated emission patterns of single molecules that are horizontally oriented to the substrate plane, namely the emission dipole is in-plane. Anisotropic patterns can be seen in Figure 6.8(a) and (b). The optical intensity at the central region is blocked considering the presence of sample holder. The orientations of the anisotropic patterns are determined by the different Φ_{dip}, and Θ_{dip} angles. When the emission dipole is vertical to the substrate plane, namely out-of-plane dipole, the emission pattern shows homogeneous intensity distribution as shown in Figure 6.8(c). In Figure 6.8(d),

the emission pattern of a dipole with an out-of-plane angle Θ_{dip} of $45°$ and in-plane angle Φ_{dip} of $0°$ is shown, which is clearly anisotropic. These distinctively different emission patterns allow us to determine the molecular orientation not only in the single molecule model system, but also well-ordered crystalline thin film.

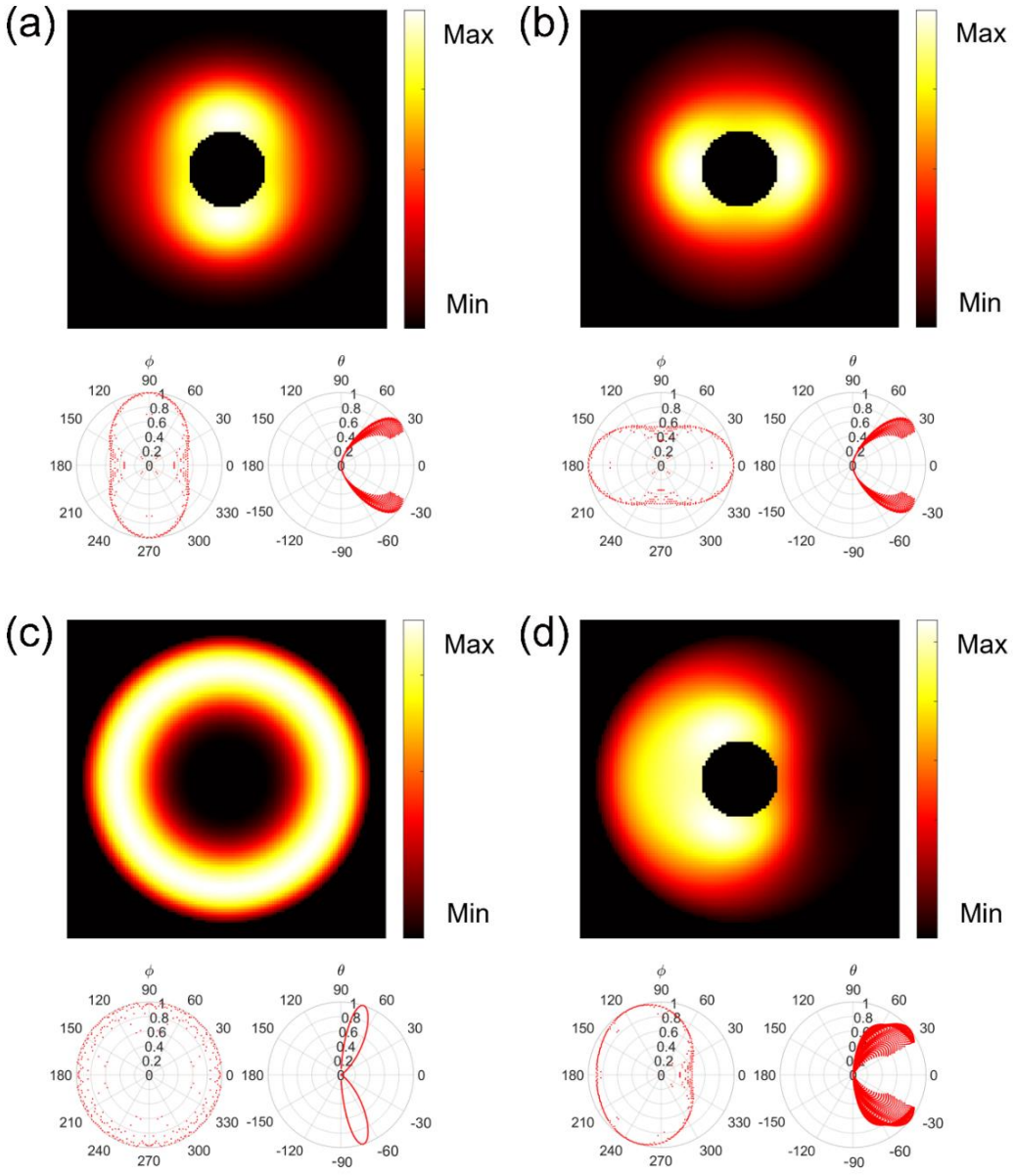

Figure 6.8: Calculated emission patterns and the corresponding polar plots (optical intensity versus in-plane angle ϕ_{em} and versus out-of-plane θ_{em}) of a single dipole at the air-SiO_2/Si interface using a parabolic mirror.

(a) $\Phi_{dip} = 0°$, $\Theta_{dip} = 0°$ (in-plane dipole). (b) $\Phi_{dip} = 90°$, $\Theta_{dip} = 0°$. (c) $\Phi_{dip} = 0°$, $\Theta_{dip} = 90°$ (out-of-plane dipole). (d) $\Phi_{dip} = 0°$, $\Theta_{dip} = 45°$.

To quantitively derive the molecular orientation information at the air-SiO_2/Si interface, the correlation between the out-of-plane angle Θ_{dip} of a dipole orientation and the out-of-plane angle θ_{em} of emission direction is calculated, as shown in Figure 6.9(a) and (b). The angle θ_{em} of emission direction is in a range from $\sim 36°$ to $\sim 72°$, where a horizontal dipole shows an emission direction $|\theta_{em}| = \sim 36°$, and a vertically oriented dipole emits the light that points towards the angle at $|\theta_{em}| = \sim 72°$. No significant transformation in the out-of-plane angle θ_{em} is observed when the dipole adopts a small tilt angle $|\Theta_{dip}| < 45°$. The angle θ_{em} of emission direction highly depends on the dipole orientation, if the tilt angle $|\Theta_{dip}|$ is larger than $45°$. In particular, the emission direction is evidently altered within the range of angle $|\Theta_{dip}|$ from $45°$ to $60°$. In this case the exact orientation of DH-P-TTA molecule within the thin film can be possibly obtained.

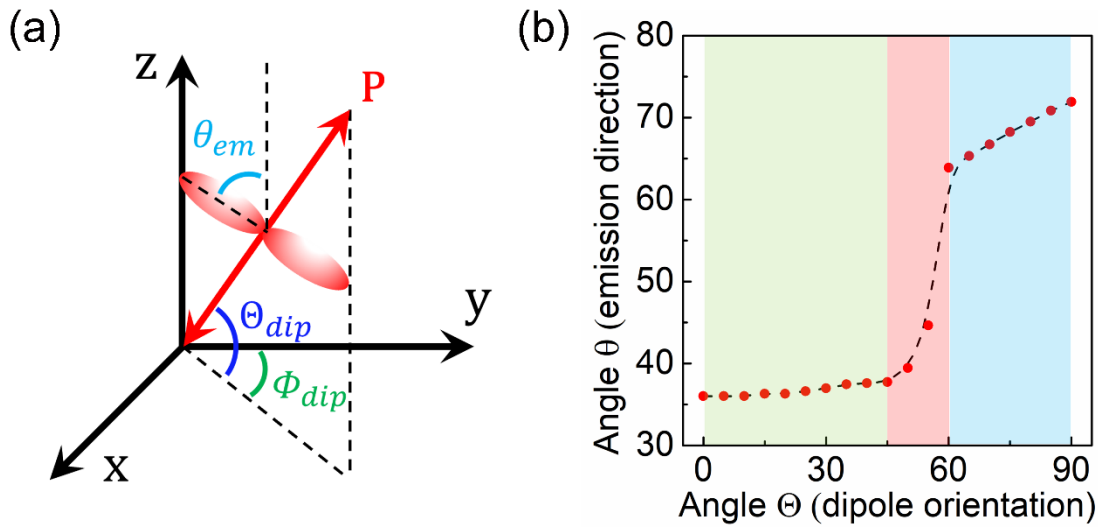

Figure 6.9: (a) The spherical angle Φ_{dip}, and Θ_{dip} defines the in-plane and out-of-plane angle of a dipole orientation, respectively. The dipole orientation is indicated by the double-ended red arrow. (b) The calculated relationship between the out-of-plane angle Θ_{dip} of a dipole orientation and the out-of-plane angle θ_{em} of emission direction at the air-SiO_2/Si interface using a parabolic mirror.

By comparing the experimental and calculated emission patterns, the possible molecular orientation in the DH-P-TTA thin film is proposed in Figure 6.10. The DH-P-TTA molecular orientation can be estimated by its emission directionality because the transition dipole moment of the molecule orients along the long axis of the molecule. We first consider the molecular orientation within the DH-P-TTA domains with a thickness ranging from 5 nm to 10 nm (seen in Figure 6.1 and Figure 6.3). Due to the multilayer feature, molecules from different layers could contribute to the observed emission patterns. No distinct variations of the emission directions (in-plane angle ϕ_{em} and out-of-plane θ_{em}) can be observed within one DH-P-TTA domain (seen in Figure 6.4), which indicates that the molecules are either ordered with a similar orientation or completely randomly oriented. The second situation is rather unlikely since the emission will be isotropic due to the overlapping of all emission directions of the randomly oriented molecules. This is clearly different from the patterns shown in Figure 6.4, which are anisotropic and are mirrored in the two domains. Furthermore, these anisotropic patterns agree very well with the calculated emission patterns shown in Figure 6.8(d), where the emission direction of a dipole with angles of $\Phi_{dip} = 0°,\ \Theta_{dip} = 45°$ is predicted. These results indicate that the molecules are well-ordered and adopt tilt angles up to $|\Theta_{dip}| \geq 45°$. This conclusion complies with the recent report that the oligomers are orderly oriented in the single-crystal layers revealed by the X-ray characterization method.[159] The reported oligomer has a similar chemical structure with the measured molecule, where the molecule is composed of a conjugated core terminated with long alkyl substituents. The molecular orientations within the two individual domains (seen in Figure 6.3) are proposed in Figure 6.10(a). Considering their opposite emission directions, the molecules in these two-neighboring domains are oriented in the mirrored directions, e.g., opposite sign of the in-plane angle Φ_{dip}.

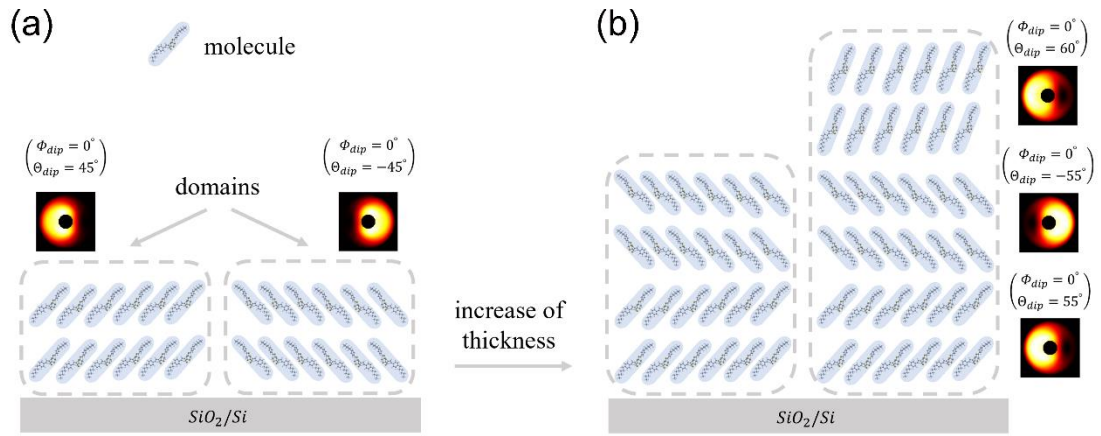

Figure 6.10: The proposed scheme for interpretation of the impact of domain and thickness on emissive directionality.

(a) thin film; (b) thick film.

With the increase of the film thickness, we assume that the molecular orientation and structural order can vary, as shown in Figure 6.10(b). In Figure 6.7(b), an isotropic emission feature is observed at the domain with a thickness of ~33.0 nm. According to the calculated result in Figure 6.9, the out-of-plane angle θ_{em} of emission direction maintains at $|\theta_{em}| = \sim 45°$, clearly suggesting that the molecules adopt the tilt angles at $|\Theta_{dip}| = \sim 55°$. As the polar plot of the optical intensity versus in-plane angle ϕ_{em} is isotropic shown in Figure 6.7(b), we attribute the isotropic pattern to the sum of emission patterns from the molecules oriented at $\Theta_{dip} = -55°$ and $\Theta_{dip} = +55°$. This result indicates that the molecules in the first few layers at the molecular film/SiO_2 interface (interfacial layers) and in the next layers (on the top of the interfacial layers) are possibly oriented in the mirrored directions. Another situation is that the molecules are oriented in the mirrored directions within an individual layer, which is rather unlikely since the molecules within one domain are well-ordered with the same orientation as discussed in Figure 6.4. Moreover, an isotropic pattern is also observed when the film thickness further increases to ~58.18 nm, and the out-of-plane angle θ_{em} of emission direction is continuously going to $|\theta_{em}| = \sim 55°$. These phenomena suggest that the molecules in the next layers

are likely oriented more vertically against the sample substrate. This kind of molecular organization has been reported in the multilayer constructed by the conjugated molecules.[6, 9, 160] These organic layers belong to single crystals, where the molecules can stand up vertically due to the strong interaction of π-conjugated moieties between the neighboring molecules. Such molecular orientations can promote the charge carrier mobilities in OFET.

6.6 Conclusion

In conclusion, we demonstrate the 2PPL angular emission patterns of DH-P-TTA thin molecule films with a k-space imaging microscopy. By comparing the experimental and calculated emission patterns, the possible molecular orientations within the DH-P-TTA thin film are discussed. We observe the anisotropic emission pattern on the ultrathin film, which suggests the molecules adopt a tilt angle and also a high degree of ordering within one domain. Moreover, close correlation between the generated 2PPL signal and the layer thickness of DH-P-TTA film is also demonstrated. Two 2PPL peak maxima located at ~516 nm and ~552 nm are clearly distinguished on the DH-P-TTA film. The almost isotropic emission patterns are visualized on the thick film with a thickness of ~33.0 nm and ~58.18 nm. The observation could be attributed to the vertical orientation of DH-P-TTA molecules in the film.

Summary and outlook

The structural properties dependency of linear and nonlinear optical properties of two-dimensional semiconducting layers are systematically investigated in this thesis. The layered materials studied in the thesis contain TMDCs flakes, molecule film/TMDCs heterostructures, and ultrathin molecule films. The home-built confocal scanning optical microscopy assisted by a parabolic mirror is employed to perform all of optical characterizations. During my Ph.D. work, the confocal microscopy combined with a femtosecond pulsed laser has been rebuilt. The additional functions, such as SHG imaging, 2PPL imaging, angular emission pattern imaging, and polarization dependency of SHG and 2PPL spectroscopies, are implemented. Applying the above-mentioned functions, we are able to identify the local structural properties of layered materials, such as the structural irregularities, structural symmetry, and crystalline orientation of TMDCs flakes, as well as their interactions with the surface adsorbates; and reveal the variations in the emission directionalities of DH-P-TTA ultrathin molecule films in the k-space.

The angular emission patterns of SHG and Raman signals from optical materials are not involved in this thesis. This optical information has recently drawn extensive attention in TMDCs materials, plasmonic nano-antennas, and metallic antennas coupled to optical semiconductors. In particular, the experimental investigations of SHG directionalities are still limited. For the implementation, the signal-to-noise ratio should be first considered and overcome. To pursue and understand the emission direction of light beam can be an open and promising task in the near future.

References

1. Chen, H.; Zhang, W.; Li, M.; He, G.; Guo, X., Interface Engineering in Organic Field-Effect Transistors: Principles, Applications, and Perspectives. *Chem. Rev.* **2020,** *120* (5), 2879-2949.

2. Bhimanapati, G. R.; Lin, Z.; Meunier, V.; Jung, Y.; Cha, J.; Das, S.; Xiao, D.; Son, Y.; Strano, M. S.; Cooper, V. R.; Liang, L.; Louie, S. G.; Ringe, E.; Zhou, W.; Kim, S. S.; Naik, R. R.; Sumpter, B. G.; Terrones, H.; Xia, F.; Wang, Y.; Zhu, J.; Akinwande, D.; Alem, N.; Schuller, J. A.; Schaak, R. E.; Terrones, M.; Robinson, J. A., Recent Advances in Two-Dimensional Materials beyond Graphene. *ACS Nano* **2015,** *9* (12), 11509-11539.

3. Huh, J.-S.; Kim, K.-H.; Moon, C.-K.; Kim, J.-J., Dependence of Pt(II) based phosphorescent emitter orientation on host molecule orientation in doped organic thin films. *Org. Electron.* **2017,** *45*, 279-284.

4. Frischeisen, J.; Yokoyama, D.; Adachi, C.; Brütting, W., Determination of molecular dipole orientation in doped fluorescent organic thin films by photoluminescence measurements. *Appl. Phys. Lett.* **2010,** *96* (7).

5. Brown, S. J.; DeCrescent, R. A.; Nakazono, D. M.; Willenson, S. H.; Ran, N. A.; Liu, X.; Bazan, G. C.; Nguyen, T. Q.; Schuller, J. A., Enhancing Organic Semiconductor-Surface Plasmon Polariton Coupling with Molecular Orientation. *Nano Lett.* **2017,** *17* (10), 6151-6156.

6. Yokoyama, D., Molecular orientation in small-molecule organic light-emitting diodes. *J. Mater. Chem.* **2011,** *21* (48).

7. Kim, M. S.; Yun, S. J.; Lee, Y.; Seo, C.; Han, G. H.; Kim, K. K.; Lee, Y. H.; Kim, J., Biexciton Emission from Edges and Grain Boundaries of Triangular WS_2 Monolayers. *ACS Nano* **2016,** *10* (2), 2399-2405.

8. van der Zande, A. M.; Huang, P. Y.; Chenet, D. A.; Berkelbach, T. C.; You, Y.; Lee, G. H.; Heinz, T. F.; Reichman, D. R.; Muller, D. A.; Hone, J. C., Grains and grain boundaries in highly crystalline monolayer molybdenum disulfide. *Nat. Mater.* **2013,** *12* (6), 554-561.

9. Li, M.; An, C.; Marszalek, T.; Baumgarten, M.; Mullen, K.; Pisula, W., Impact of Interfacial Microstructure on Charge Carrier Transport in Solution-Processed Conjugated Polymer Field-Effect Transistors. *Adv. Mater.* **2016,** *28* (11), 2245-2252.

10. Hong, J.; Wang, C.; Liu, H.; Ren, X.; Chen, J.; Wang, G.; Jia, J.; Xie, M.; Jin, C.; Ji, W.; Yuan, J.; Zhang, Z., Inversion Domain Boundary Induced Stacking and Bandstructure Diversity in Bilayer $MoSe_2$. *Nano Lett.* **2017,** *17* (11), 6653-6660.

11. Li, J.; Joseph, T.; Ghorbani-Asl, M.; Kolekar, S.; Krasheninnikov, A. V.; Batzill, M., Mirror twin boundaries in $MoSe_2$ monolayers as one dimensional nanotemplates for selective water adsorption. *Nanoscale* **2021,** *13* (2), 1038-1047.

12. Hong, J.; Hu, Z.; Probert, M.; Li, K.; Lv, D.; Yang, X.; Gu, L.; Mao, N.; Feng, Q.; Xie, L.; Zhang, J.; Wu, D.; Zhang, Z.; Jin, C.; Ji, W.; Zhang, X.; Yuan, J.; Zhang, Z., Exploring atomic defects in molybdenum disulfide monolayers. *Nat. Commun.* **2015,** *6*, 6293.

13. Chen, W.; Nikiforov, M. P.; Darling, S. B., Morphology characterization in organic and hybrid solar cells. *Energy Environ. Sci.* **2012,** *5* (8).

14. Sirringhaus, H.; Brown, P.; Friend, R.; Nielsen, M. M.; Bechgaard, K.; Langeveld-Voss, B.; Spiering, A.; Janssen, R. A.; Meijer, E.; Herwig, P. J. N., Two-dimensional charge transport in self-organized, high-mobility conjugated polymers. *Nature* **1999,** *401* (6754), 685-688.

15. Leijten, Z.; Keizer, A. D. A.; de With, G.; Friedrich, H., Quantitative Analysis of Electron Beam Damage in Organic Thin Films. *J. Phys. Chem. C* **2017,** *121* (19), 10552-10561.

16. Parson, W. W., *Modern optical spectroscopy*. **2007,** 2.

17. Maiman, T. H., Stimulated Optical Radiation in Ruby. *Nature* **1960,** *187* (4736), 493-494.

18. Li, Y.; Rao, Y.; Mak, K. F.; You, Y.; Wang, S.; Dean, C. R.; Heinz, T. F., Probing symmetry properties of few-layer MoS_2 and h-BN by optical second-harmonic generation. *Nano Lett.* **2013,** *13* (7), 3329-3333.

19. Lin, Z.; Carvalho, B. R.; Kahn, E.; Lv, R.; Rao, R.; Terrones, H.; Pimenta, M. A.; Terrones, M., Defect engineering of two-dimensional transition metal dichalcogenides. *2D Mater.* **2016,** *3* (2).

20. Wu, Z.; Ni, Z., Spectroscopic investigation of defects in two-dimensional materials. *Nanophotonics* **2017,** *6* (6), 1219-1237.

21. Lee, C.; Jeong, B. G.; Yun, S. J.; Lee, Y. H.; Lee, S. M.; Jeong, M. S., Unveiling Defect-Related Raman Mode of Monolayer WS_2 via Tip-Enhanced Resonance Raman Scattering. *ACS Nano* **2018,** *12* (10), 9982-9990.

22. Zhang, X.; Tan, Q. H.; Wu, J. B.; Shi, W.; Tan, P. H., Review on the Raman spectroscopy of different types of layered materials. *Nanoscale* **2016,** *8* (12), 6435-6450.

23. Rodriguez, A.; Verhagen, T.; Kalbac, M.; Vejpravova, J.; Frank, O., Imaging Nanoscale Inhomogeneities and Edge Delamination in As‐Grown MoS_2 Using Tip‐Enhanced Photoluminescence. *Phys. Status Solidi RRL* **2019,** *13* (11).

24. Liu, H.; Lu, J.; Ho, K.; Hu, Z.; Dang, Z.; Carvalho, A.; Tan, H. R.; Tok, E. S.; Sow, C. H., Fluorescence Concentric Triangles: A Case of Chemical Heterogeneity in WS_2 Atomic Monolayer. *Nano Lett.* **2016,** *16* (9), 5559-5567.

25. Gutierrez, H. R.; Perea-Lopez, N.; Elias, A. L.; Berkdemir, A.; Wang, B.; Lv, R.; Lopez-Urias, F.; Crespi, V. H.; Terrones, H.; Terrones, M., Extraordinary room-temperature photoluminescence in triangular WS_2 monolayers. *Nano Lett.* **2013,** *13* (8), 3447-3454.

26. Mouri, S.; Miyauchi, Y.; Matsuda, K., Tunable Photoluminescence of Monolayer MoS_2 via Chemical Doping. *Nano Lett.* **2013,** *13* (12), 5944-5948.

27. Rosa, H. G.; Junpeng, L.; Gomes, L. C.; Rodrigues, M. J. L. F.; Haur,

S. C.; Gomes, J. C. V., Second-Harmonic Spectroscopy for Defects Engineering Monitoring in Transition Metal Dichalcogenides. *Adv. Opt. Mater.* **2018,** *6* (5).

28. Mennel, L.; Paur, M.; Mueller, T., Second harmonic generation in strained transition metal dichalcogenide monolayers: MoS_2, $MoSe_2$, WS_2, and WSe_2. *APL Photonics* **2019,** *4* (3).

29. Wang, G.; Marie, X.; Gerber, I.; Amand, T.; Lagarde, D.; Bouet, L.; Vidal, M.; Balocchi, A.; Urbaszek, B., Giant Enhancement of the Optical Second-Harmonic Emission of WSe_2 Monolayers by Laser Excitation at Exciton Resonances. *Phys. Rev. Lett.* **2015,** *114* (9), 097403.

30. Dai, X.; Zhang, X.; Kislyakov, I. M.; Wang, L.; Huang, J.; Zhang, S.; Dong, N.; Wang, J., Enhanced two-photon absorption and two-photon luminescence in monolayer MoS_2 and WS_2 by defect repairing. *Opt. Express* **2019,** *27* (10), 13744-13753.

31. Zhang, S.; Dong, N.; McEvoy, N.; O'Brien, M.; Winters, S.; Berner, N. C.; Yim, C.; Li, Y.; Zhang, X.; Chen, Z.; Zhang, L.; Duesberg, G. S.; Wang, J., Direct Observation of Degenerate Two-Photon Absorption and Its Saturation in WS_2 and MoS_2 Monolayer and Few-Layer Films. *ACS Nano* **2015,** *9* (7), 7142-7150.

32. Li, Y.; Dong, N.; Zhang, S.; Zhang, X.; Feng, Y.; Wang, K.; Zhang, L.; Wang, J., Giant two-photon absorption in monolayer MoS_2. *Laser & Photonics Rev.* **2015,** *9* (4), 427-434.

33. Fan, X.; Jiang, Y.; Zhuang, X.; Liu, H.; Xu, T.; Zheng, W.; Fan, P.; Li, H.; Wu, X.; Zhu, X.; Zhang, Q.; Zhou, H.; Hu, W.; Wang, X.; Sun, L.; Duan, X.; Pan, A., Broken Symmetry Induced Strong Nonlinear Optical Effects in Spiral WS_2 Nanosheets. *ACS Nano* **2017,** *11* (5), 4892-4898.

34. Shen, Y. R., Surface properties probed by second-harmonic and sum-frequency generation. *Nature* **1989,** *337* (6207), 519-525.

35. Lin, X.; Liu, Y.; Wang, K.; Wei, C.; Zhang, W.; Yan, Y.; Li, Y. J.; Yao, J.; Zhao, Y. S., Two-Dimensional Pyramid-like WS_2 Layered Structures for

Highly Efficient Edge Second-Harmonic Generation. *ACS Nano* **2018,** *12* (1), 689-696.

36. Fourkas, J. T., Rapid determination of the three-dimensional orientation of single molecules. *Opt. Lett.* **2001,** *26* (4), 211-213.

37. Woźniak, P.; Banzer, P., Single nanoparticle real and k-space spectroscopy with structured light. *New J. Phys.* **2021,** *2*3, 103013.

38. Gao, Y.; Weidman, M. C.; Tisdale, W. A., CdSe Nanoplatelet Films with Controlled Orientation of their Transition Dipole Moment. *Nano Lett.* **2017,** *17* (6), 3837-3843.

39. Jurow, M. J.; Morgenstern, T.; Eisler, C.; Kang, J.; Penzo, E.; Do, M.; Engelmayer, M.; Osowiecki, W. T.; Bekenstein, Y.; Tassone, C.; Wang, L. W.; Alivisatos, A. P.; Brutting, W.; Liu, Y., Manipulating the Transition Dipole Moment of $CsPbBr_3$ Perovskite Nanocrystals for Superior Optical Properties. *Nano Lett.* **2019,** *19* (4), 2489-2496.

40. Boyd, R. W., *Nonlinear optics 4th*. **2020**.

41. Kauranen, M.; Zayats, A. V., Nonlinear plasmonics. *Nat. Photonics* **2012,** *6* (11), 737-748.

42. Franken, P. A.; Hill, A. E.; Peters, C. W.; Weinreich, G., Generation of Optical Harmonics. *Phys. Rev. Lett.* **1961,** *7* (4), 118-119.

43. Kumar, V.; Coluccelli, N.; Polli, D., Coherent Optical Spectroscopy/Microscopy and Applications. **2018,** 87-115.

44. Panoiu, N. C.; Sha, W. E. I.; Lei, D. Y.; Li, G. C., Nonlinear optics in plasmonic nanostructures. *Journal of Optics* **2018,** *20* (8).

45. Zhou, L.; Fu, H.; Lv, T.; Wang, C.; Gao, H.; Li, D.; Deng, L.; Xiong, W., Nonlinear Optical Characterization of 2D Materials. *Nanomaterials* **2020,** *10* (11), 2263.

46. Zhou, J.; Lin, J.; Huang, X.; Zhou, Y.; Chen, Y.; Xia, J.; Wang, H.; Xie, Y.; Yu, H.; Lei, J.; Wu, D.; Liu, F.; Fu, Q.; Zeng, Q.; Hsu, C. H.; Yang, C.; Lu, L.; Yu, T.; Shen, Z.; Lin, H.; Yakobson, B. I.; Liu, Q.; Suenaga, K.; Liu, G.; Liu, Z., A library of atomically thin metal chalcogenides.

Nature **2018,** *556* (7701), 355-359.

47. Mak, K. F.; Lee, C.; Hone, J.; Shan, J.; Heinz, T. F. J. P. r. l., Atomically thin MoS_2: a new direct-gap semiconductor. *Phys. Rev. Lett.* **2010,** *105* (13), 136805.

48. You, J. W.; Bongu, S. R.; Bao, Q.; Panoiu, N. C., Nonlinear optical properties and applications of 2D materials: theoretical and experimental aspects. *Nanophotonics* **2018,** *8* (1), 63-97.

49. Malard, L. M.; Alencar, T. V.; Barboza, A. P. M.; Mak, K. F.; de Paula, A. M., Observation of intense second harmonic generation from MoS_2 atomic crystals. *Phys. Rev. B* **2013,** *87* (20).

50. Wilson, J. A.; Yoffe, A. D., The transition metal dichalcogenides discussion and interpretation of the observed optical, electrical and structural properties. *Adv. in Phys.* **1969,** *18* (73), 193-335.

51. Zhao, M.; Ye, Z.; Suzuki, R.; Ye, Y.; Zhu, H.; Xiao, J.; Wang, Y.; Iwasa, Y.; Zhang, X., Atomically phase-matched second-harmonic generation in a 2D crystal. *Light: Sci. Appl.* **2016,** *5* (8), e16131.

52. Kaiser, W.; Garrett, C. G. B., Two-Photon Excitation in CaF_2:Eu^{2+}. *Phys. Rev. Lett.* **1961,** *7* (6), 229-231.

53. Pascal, S.; David, S.; Andraud, C.; Maury, O., Near-infrared dyes for two-photon absorption in the short-wavelength infrared: strategies towards optical power limiting. *Chem. Soc. Rev.* **2021,** 50, 6613-6658.

54. Dong, N.; Li, Y.; Zhang, S.; McEvoy, N.; Gatensby, R.; Duesberg, G. S.; Wang, J., Saturation of Two-Photon Absorption in Layered Transition Metal Dichalcogenides: Experiment and Theory. *ACS Photonics* **2018,** *5* (4), 1558-1565.

55. Ye, Z.; Cao, T.; O'Brien, K.; Zhu, H.; Yin, X.; Wang, Y.; Louie, S. G.; Zhang, X., Probing excitonic dark states in single-layer tungsten disulfide. *Nature* **2014,** *513* (7517), 214-218.

56. Raman, C. V.; Krishnan, K. S. J. N., A new type of secondary radiation. *Nature* **1928,** *121* (3048), 501-502.

57. Jones, R. R.; Hooper, D. C.; Zhang, L.; Wolverson, D.; Valev, V. K., Raman Techniques: Fundamentals and Frontiers. *Nanoscale Res. Lett.* **2019,** *14* (1), 231.

58. Graves, P.; Gardiner, D. J. S., Practical Raman spectroscopy. **1989**.

59. Wang, X.; Huang, S.-C.; Hu, S.; Yan, S.; Ren, B., Fundamental understanding and applications of plasmon-enhanced Raman spectroscopy. *Nat. Rev. Phys.* **2020,** *2* (5), 253-271.

60. Madzharova, F.; Heiner, Z.; Kneipp, J., Surface enhanced hyper Raman scattering (SEHRS) and its applications. *Chem. Soc. Rev.* **2017,** *46* (13), 3980-3999.

61. Verma, P., Tip-Enhanced Raman Spectroscopy: Technique and Recent Advances. *Chem. Rev.* **2017,** *117* (9), 6447-6466.

62. Blum, C.; Opilik, L.; Atkin, J. M.; Braun, K.; Kämmer, S. B.; Kravtsov, V.; Kumar, N.; Lemeshko, S.; Li, J.-F.; Luszcz, K.; Maleki, T.; Meixner, A. J.; Minne, S.; Raschke, M. B.; Ren, B.; Rogalski, J.; Roy, D.; Stephanidis, B.; Wang, X.; Zhang, D.; Zhong, J.-H.; Zenobi, R., Tip-enhanced Raman spectroscopy - an interlaboratory reproducibility and comparison study. *J. Raman Spectrosc.* **2014,** *45* (1), 22-31.

63. Fleischmann, M.; Hendra, P. J.; McQuillan, A. J., Raman spectra of pyridine adsorbed at a silver electrode. *Chem. Phys. Lett.* **1974,** *26* (2), 163-166.

64. Le Ru, E.; Etchegoin, P., *Principles of Surface-Enhanced Raman Spectroscopy and related plasmonic effects*. **2008**.

65. Ling, X.; Xie, L.; Fang, Y.; Xu, H.; Zhang, H.; Kong, J.; Dresselhaus, M. S.; Zhang, J.; Liu, Z., Can graphene be used as a substrate for Raman enhancement? *Nano Lett.* **2010,** *10* (2), 553-561.

66. Ling, X.; Moura, L. G.; Pimenta, M. A.; Zhang, J., Charge-Transfer Mechanism in Graphene-Enhanced Raman Scattering. *J. Phys. Chem. C* **2012,** *116* (47), 25112-25118.

67. Rodriguez, R. D.; Villagómez, C. J.; Khodadadi, A.; Kupfer, S.;

Averkiev, A.; Dedelaite, L.; Tang, F.; Khaywah, M. Y.; Kolchuzhin, V.; Ramanavicius, A.; Adam, P.-M.; Gräfe, S.; Sheremet, E., Chemical Enhancement vs Molecule–Substrate Geometry in Plasmon-Enhanced Spectroscopy. *ACS Photonics* **2021,** *8*, 2243-2255.

68. Fu, S.; Wang, R.; Tang, D.; Zhang, X.; He, D., Directly Probing Interfacial Coupling in a Monolayer $MoSe_2$ and CuPc Heterostructure. *ACS Appl. Mater. Interfaces* **2021,** *13* (15), 18372-18379.

69. Amsterdam, S. H.; Stanev, T. K.; Zhou, Q.; Lou, A. J.; Bergeron, H.; Darancet, P.; Hersam, M. C.; Stern, N. P.; Marks, T. J., Electronic Coupling in Metallophthalocyanine-Transition Metal Dichalcogenide Mixed-Dimensional Heterojunctions. *ACS Nano* **2019,** *13* (4), 4183-4190.

70. Huang, S.; Ling, X.; Liang, L.; Song, Y.; Fang, W.; Zhang, J.; Kong, J.; Meunier, V.; Dresselhaus, M. S., Molecular Selectivity of Graphene-Enhanced Raman Scattering. *Nano Lett.* **2015,** *15* (5), 2892-2901.

71. Tan, Y.; Ma, L.; Gao, Z.; Chen, M.; Chen, F., Two-Dimensional Heterostructure as a Platform for Surface-Enhanced Raman Scattering. *Nano Lett.* **2017,** *17* (4), 2621-2626.

72. Willets, K. A.; Van Duyne, R. P., Localized surface plasmon resonance spectroscopy and sensing. *Annu. Rev. Phys. Chem.* **2007,** *58*, 267-97.

73. Giannini, V.; Fernandez-Dominguez, A. I.; Heck, S. C.; Maier, S. A., Plasmonic nanoantennas: fundamentals and their use in controlling the radiative properties of nanoemitters. *Chem. Rev.* **2011,** *111* (6), 3888-3912.

74. Schlucker, S., Surface-enhanced Raman spectroscopy: concepts and chemical applications. *Angew. Chem. Int.* **2014,** *53* (19), 4756-4795.

75. Stiles, P. L.; Dieringer, J. A.; Shah, N. C.; Van Duyne, R. P., Surface-enhanced Raman spectroscopy. *Annu. Rev. Anal. Chem.* **2008,** *1*, 601-626.

76. Adrian, F. J., Charge transfer effects in surface ‐ enhanced Raman scattering). *J. Chem. Phys.* **1982,** *77* (11), 5302-5314.

77. Lippitsch, M. E., Ground-state charge transfer as a mechanism for surface-enhanced Raman scattering. *Phys. Rev. B* **1984,** *29* (6), 3101-3110.

78. Mrozek, I.; Otto, A., Long and Short-Range Effects in SERS from Silver. *Europhys. Lett.* **1990,** *11* (3), 243-248.

79. McCall, S. L.; Platzman, P. M.; Wolff, P. A., Surface enhanced Raman scattering. *Phys. Lett. A* **1980,** *77* (5), 381-383.

80. Abe, H.; Manzel, K.; Schulze, W.; Moskovits, M.; DiLella, D. P., Surface‐enhanced Raman spectroscopy of CO adsorbed on colloidal silver particles. *J. Chem. Phys.* **1981,** *74* (2), 792-797.

81. Eesley, G. L., Coverage dependence of enhanced adsorbate Raman scattering. *Phys. Lett. A* **1981,** *81* (2), 193-196.

82. Murray, C. A.; Allara, D. L., Measurement of the molecule–silver separation dependence of surface enhanced Raman scattering in multilayered structures. *J. Chem. Phys.* **1982,** *76* (3), 1290-1303.

83. Mrozek, I.; Otto, A., Quantitative separation of the “classical” electromagnetic and the “chemical” contribution to surface enhanced Raman scattering. *J. Electron Spectrosc. Relat. Phenom.* **1990,** *54-55*, 895-911.

84. Novotny, L., Single molecule fluorescence in inhomogeneous environments. *Appl. Phys. Lett.* **1996,** *69* (25), 3806-3808.

85. Jasny, J.; Sepioł, J., Single molecules observed by immersion mirror objective. A novel method of finding the orientation of a radiating dipole. *Chem. Phys. Lett.* **1997,** *273* (5), 439-443.

86. Bartko, A. P.; Dickson, R. M., Imaging Three-Dimensional Single Molecule Orientations. *J. Phys. Chem. B* **1999,** *103* (51), 11237-11241.

87. Lieb, M. A.; Zavislan, J. M.; Novotny, L., Single-molecule orientations determined by direct emission pattern imaging. *J. Opt. Soc. Am. B* **2004,** *21* (6), 1210-1215.

88. Brokmann, X.; Coolen, L.; Hermier, J.-P.; Dahan, M., Emission properties of single CdSe/ZnS quantum dots close to a dielectric interface. *Chem. Phys.* **2005,** *318* (1-2), 91-98.

89. Weyl, H., Ausbreitung elektromagnetischer Wellen über einem ebenen Leiter. *Annalen der Physik* **1919,** *365* (21), 481-500.

90. Ma, Y.; Diaz, H. C.; Avila, J.; Chen, C.; Kalappattil, V.; Das, R.; Phan, M. H.; Cadez, T.; Carmelo, J. M.; Asensio, M. C.; Batzill, M., Angle resolved photoemission spectroscopy reveals spin charge separation in metallic $MoSe_2$ grain boundary. *Nat. Commun.* **2017,** *8*, 14231.

91. Halas, N. J.; Lal, S.; Chang, W. S.; Link, S.; Nordlander, P., Plasmons in strongly coupled metallic nanostructures. *Chem. Rev.* **2011,** *111* (6), 3913-61.

92. Lieb, M. A.; Meixner, A. J., A high numerical aperture parabolic mirror as imaging device for confocal microscopy. *Opt. Express* **2001,** *8* (7), 458-474.

93. Stadler, J.; Stanciu, C.; Stupperich, C.; Meixner, A. J., Tighter focusing with a parabolic mirror. *Opt. Lett.* **2008,** *33* (7), 681-683.

94. Dorn, R.; Quabis, S.; Leuchs, G., Sharper focus for a radially polarized light beam. *Phys. Rev. Lett.* **2003,** *91* (23), 233901.

95. Wang, J.; Gurdal, E.; Horneber, A.; Dickreuter, S.; Kostcheev, S.; Meixner, A. J.; Fleischer, M.; Adam, P. M.; Zhang, D., Carrier recombination and plasmonic emission channels in metallic photoluminescence. *Nanoscale* **2018,** *10* (17), 8240-8245.

96. Shahbazyan, T. V., Theory of plasmon-enhanced metal photoluminescence. *Nano Lett.* **2013,** *13* (1), 194-198.

97. Zuchner, T.; Failla, A. V.; Meixner, A. J., Light microscopy with doughnut modes: a concept to detect, characterize, and manipulate individual nanoobjects. *Angew. Chem. Int.* **2011,** *50* (23), 5274-93.

98. Sebait, R.; Biswas, C.; Song, B.; Seo, C.; Lee, Y. H., Identifying Defect-Induced Trion in Monolayer WS_2 via Carrier Screening Engineering. *ACS Nano* **2021,** *15* (2), 2849-2857.

99. Huang, T. X.; Cong, X.; Wu, S. S.; Lin, K. Q.; Yao, X.; He, Y. H.; Wu, J. B.; Bao, Y. F.; Huang, S. C.; Wang, X.; Tan, P. H.; Ren, B., Probing the edge-related properties of atomically thin MoS_2 at nanoscale. *Nat. Commun.* **2019,** *10* (1), 5544.

100. Smithe, K. K. H.; Krayev, A. V.; Bailey, C. S.; Lee, H. R.; Yalon,

E.; Aslan, Ö. B.; Muñoz Rojo, M.; Krylyuk, S.; Taheri, P.; Davydov, A. V.; Heinz, T. F.; Pop, E., Nanoscale Heterogeneities in Monolayer $MoSe_2$ Revealed by Correlated Scanning Probe Microscopy and Tip-Enhanced Raman Spectroscopy. *ACS Appl. Nano Mater.* **2018,** *1* (2), 572-579.

101. Zhou, J.; Tang, B.; Lin, J.; Lv, D.; Shi, J.; Sun, L.; Zeng, Q.; Niu, L.; Liu, F.; Wang, X.; Liu, X.; Suenaga, K.; Jin, C.; Liu, Z., Morphology Engineering in Monolayer MoS_2 - WS_2 Lateral Heterostructures. *Adv. Funct. Mater.* **2018,** *28* (31).

102. Kern, J.; Trügler, A.; Niehues, I.; Ewering, J.; Schmidt, R.; Schneider, R.; Najmaei, S.; George, A.; Zhang, J.; Lou, J.; Hohenester, U.; Michaelis de Vasconcellos, S.; Bratschitsch, R., Nanoantenna-Enhanced Light–Matter Interaction in Atomically Thin WS_2. *ACS Photonics* **2015,** *2* (9), 1260-1265.

103. Li, X.; Liu, W.; Song, Y.; Zhang, C.; Long, H.; Wang, K.; Wang, B.; Lu, P., Enhancement of the Second Harmonic Generation from WS_2 Monolayers by Cooperating with Dielectric Microspheres. *Adv. Opt. Mater.* **2018,** *7* (3).

104. Li, B.; Gong, Y.; Hu, Z.; Brunetto, G.; Yang, Y.; Ye, G.; Zhang, Z.; Lei, S.; Jin, Z.; Bianco, E.; Zhang, X.; Wang, W.; Lou, J.; Galvão, D. S.; Tang, M.; Yakobson, B. I.; Vajtai, R.; Ajayan, P. M., Solid-Vapor Reaction Growth of Transition-Metal Dichalcogenide Monolayers. *Angew. Chem. Inter.* **2016,** *55* (36), 10656-10661.

105. Zeng, H.; Liu, G. B.; Dai, J.; Yan, Y.; Zhu, B.; He, R.; Xie, L.; Xu, S.; Chen, X.; Yao, W.; Cui, X., Optical signature of symmetry variations and spin-valley coupling in atomically thin tungsten dichalcogenides. *Sci. Rep.* **2013,** *3*, 1608.

106. McCreary, K. M.; Hanbicki, A. T.; Singh, S.; Kawakami, R. K.; Jernigan, G. G.; Ishigami, M.; Ng, A.; Brintlinger, T. H.; Stroud, R. M.; Jonker, B. T., The Effect of Preparation Conditions on Raman and Photoluminescence of Monolayer WS_2. *Sci. Rep.* **2016,** *6*, 35154.

107. Berkdemir, A.; Gutiérrez, H. R.; Botello-Méndez, A. R.; Perea-López, N.; Elías, A. L.; Chia, C.-I.; Wang, B.; Crespi, V. H.; López-Urías, F.; Charlier, J.-C.; Terrones, H.; Terrones, M., Identification of individual and few layers of WS_2 using Raman Spectroscopy. *Sci. Rep.* **2013,** *3* (1).

108. Peimyoo, N.; Shang, J.; Cong, C.; Shen, X.; Wu, X.; Yeow, E. K. L.; Yu, T., Nonblinking, Intense Two-Dimensional Light Emitter: Monolayer WS_2 Triangles. *ACS Nano* **2013,** *7* (12), 10985-10994.

109. Lin, K. I.; Ho, Y. H.; Liu, S. B.; Ciou, J. J.; Huang, B. T.; Chen, C.; Chang, H. C.; Tu, C. L.; Chen, C. H., Atom-Dependent Edge-Enhanced Second-Harmonic Generation on MoS_2 Monolayers. *Nano Lett.* **2018,** *18* (2), 793-797.

110. Yin, X.; Ye, Z.; Chenet, D. A.; Ye, Y.; O'Brien, K.; Hone, J. C.; Zhang, X., Edge Nonlinear Optics on a MoS_2 Atomic Monolayer. *Science* **2014,** *344* (6183), 488-490.

111. Hu, Z.; Avila, J.; Wang, X.; Leong, J. F.; Zhang, Q.; Liu, Y.; Asensio, M. C.; Lu, J.; Carvalho, A.; Sow, C. H.; Castro Neto, A. H., The Role of Oxygen Atoms on Excitons at the Edges of Monolayer WS_2. *Nano Lett.* **2019,** *19* (7), 4641-4650.

112. Luo, Z.; Zheng, W.; Luo, N.; Liu, B.; Zheng, B.; Yang, X.; Liang, D.; Qu, J.; Liu, H.; Chen, Y.; Jiang, Y.; Chen, S.; Zou, X.; Pan, A., Photoluminescence Lightening: Extraordinary Oxygen Modulated Dynamics in WS_2 Monolayers. *Nano Lett.* **2022,** *22* (5), 2112-2119.

113. Pankove, J. I. J. N. J., Optical processes in semiconductors Prentice-Hall. *New Jersey* **1971,** *92*, 36.

114. Barja, S.; Wickenburg, S.; Liu, Z.-F.; Zhang, Y.; Ryu, H.; Ugeda, Miguel M.; Hussain, Z.; Shen, Z.-X.; Mo, S.-K.; Wong, E.; Salmeron, Miquel B.; Wang, F.; Crommie, M. F.; Ogletree, D. F.; Neaton, Jeffrey B.; Weber-Bargioni, A., Charge density wave order in 1D mirror twin boundaries of single-layer $MoSe_2$. *Nat. Phys.* **2016,** *12* (8), 751-756.

115. Zeng, Z.; Sun, X.; Zhang, D.; Zheng, W.; Fan, X.; He, M.; Xu,

T.; Sun, L.; Wang, X.; Pan, A., Controlled Vapor Growth and Nonlinear Optical Applications of Large-Area 3R Phase WS_2 and WSe_2 Atomic Layers. *Adv. Funct. Mater.* **2019,** *29* (11).

116. Zhao, W.; Ghorannevis, Z.; Chu, L.; Toh, M.; Kloc, C.; Tan, P.-H.; Eda, G., Evolution of Electronic Structure in Atomically Thin Sheets of WS_2 and WSe_2. *ACS Nano* **2013,** *7* (1), 791-797.

117. Kumar, N.; Najmaei, S.; Cui, Q.; Ceballos, F.; Ajayan, P. M.; Lou, J.; Zhao, H., Second harmonic microscopy of monolayer MoS_2. *Phys. Rev. B* **2013,** *87* (16), 161403.

118. Splendiani, A.; Sun, L.; Zhang, Y.; Li, T.; Kim, J.; Chim, C.-Y.; Galli, G.; Wang, F., Emerging Photoluminescence in Monolayer MoS_2. *Nano Lett.* **2010,** *10* (4), 1271-1275.

119. Li, H.; Yin, Z.; He, Q.; Li, H.; Huang, X.; Lu, G.; Fam, D. W. H.; Tok, A. I. Y.; Zhang, Q.; Zhang, H., Fabrication of Single- and Multilayer MoS_2 Film-Based Field-Effect Transistors for Sensing NO at Room Temperature. *Small* **2012,** *8* (1), 63-67.

120. Song, Y.; Hu, S.; Lin, M.-L.; Gan, X.; Tan, P.-H.; Zhao, J., Extraordinary Second Harmonic Generation in ReS_2 Atomic Crystals. *ACS Photonics* **2018,** *5* (9), 3485-3491.

121. Zheng, Z.; Cong, S.; Gong, W.; Xuan, J.; Li, G.; Lu, W.; Geng, F.; Zhao, Z., Semiconductor SERS enhancement enabled by oxygen incorporation. *Nat. Commun.* **2017,** *8* (1).

122. Liang, J.; Zhang, J.; Li, Z.; Hong, H.; Wang, J.; Zhang, Z.; Zhou, X.; Qiao, R.; Xu, J.; Gao, P.; Liu, Z.; Liu, Z.; Sun, Z.; Meng, S.; Liu, K.; Yu, D., Monitoring Local Strain Vector in Atomic-Layered $MoSe_2$ by Second-Harmonic Generation. *Nano Lett.* **2017,** *17* (12), 7539-7543.

123. Karvonen, L.; Saynatjoki, A.; Huttunen, M. J.; Autere, A.; Amirsolaimani, B.; Li, S.; Norwood, R. A.; Peyghambarian, N.; Lipsanen, H.; Eda, G.; Kieu, K.; Sun, Z., Rapid visualization of grain boundaries in monolayer MoS_2 by multiphoton microscopy. *Nat. Commun.* **2017,** *8*, 15714.

124. Cheng, J.; Jiang, T.; Ji, Q.; Zhang, Y.; Li, Z.; Shan, Y.; Zhang, Y.; Gong, X.; Liu, W.; Wu, S., Kinetic Nature of Grain Boundary Formation in As-Grown MoS_2 Monolayers. *Adv. Mater.* **2015,** *27* (27), 4069-4074.

125. Carvalho, B. R.; Wang, Y.; Fujisawa, K.; Zhang, T.; Kahn, E.; Bilgin, I.; Ajayan, P. M.; de Paula, A. M.; Pimenta, M. A.; Kar, S.; Crespi, V. H.; Terrones, M.; Malard, L. M., Nonlinear Dark-Field Imaging of One-Dimensional Defects in Monolayer Dichalcogenides. *Nano Lett.* **2020,** *20* (1), 284-291.

126. Sahoo, P. K.; Zong, H.; Liu, J.; Xue, W.; Lai, X.; Gutiérrez, H. R.; Voronine, D. V., Probing nano-heterogeneity and aging effects in lateral 2D heterostructures using tip-enhanced photoluminescence. *Opt. Mater. Express* **2019,** *9* (4), 1620-1631.

127. Tongay, S.; Zhou, J.; Ataca, C.; Lo, K.; Matthews, T. S.; Li, J.; Grossman, J. C.; Wu, J., Thermally driven crossover from indirect toward direct bandgap in 2D semiconductors: $MoSe_2$ versus MoS_2. *Nano Lett.* **2012,** *12* (11), 5576-80.

128. Kim, D. H.; Lim, D., Optical second-harmonic generation in few-layer $MoSe_2$. *J. Korean Phys. Soc.* **2015,** *66* (5), 816-820.

129. Moore, D.; Jo, K.; Nguyen, C.; Lou, J.; Muratore, C.; Jariwala, D.; Glavin, N. R., Uncovering topographically hidden features in 2D $MoSe_2$ with correlated potential and optical nanoprobes. *npj 2D Mater. Appl.* **2020,** *4* (1).

130. Tonndorf, P.; Schmidt, R.; Böttger, P.; Zhang, X.; Börner, J.; Liebig, A.; Albrecht, M.; Kloc, C.; Gordan, O.; Zahn, D. R. T.; Michaelis de Vasconcellos, S.; Bratschitsch, R., Photoluminescence emission and Raman response of monolayer MoS_2, $MoSe_2$, and WSe_2. *Opt. Express* **2013,** *21* (4), 4908-4916.

131. Beal, A. R.; Knights, J. C.; Liang, W. Y., Transmission spectra of some transition metal dichalcogenides. II. Group VIA: trigonal prismatic coordination. *J. Phys. C: Solid State Phys.* **1972,** *5* (24), 3540-3551.

132. Mak, K. F.; Lee, C.; Hone, J.; Shan, J.; Heinz, T. F., Atomically thin

MoS_2: a new direct-gap semiconductor. *Phys. Rev. Lett.* **2010,** *105* (13), 136805.

133. Arora, A.; Nogajewski, K.; Molas, M.; Koperski, M.; Potemski, M., Exciton band structure in layered $MoSe_2$: from a monolayer to the bulk limit. *Nanoscale* **2015,** *7* (48), 20769-20775.

134. Hsu, W.-T.; Zhao, Z.-A.; Li, L.-J.; Chen, C.-H.; Chiu, M.-H.; Chang, P.-S.; Chou, Y.-C.; Chang, W.-H., Second Harmonic Generation from Artificially Stacked Transition Metal Dichalcogenide Twisted Bilayers. *ACS Nano* **2014,** *8* (3), 2951-2958.

135. Arora, A.; Noky, J.; Druppel, M.; Jariwala, B.; Deilmann, T.; Schneider, R.; Schmidt, R.; Del Pozo-Zamudio, O.; Stiehm, T.; Bhattacharya, A.; Kruger, P.; Michaelis de Vasconcellos, S.; Rohlfing, M.; Bratschitsch, R., Highly Anisotropic in-Plane Excitons in Atomically Thin and Bulklike 1T'-$ReSe_2$. *Nano Lett.* **2017,** *17* (5), 3202-3207.

136. Sheng, Y.; Best, A.; Butt, H.-J.; Krolikowski, W.; Arie, A.; Koynov, K., Three-dimensional ferroelectric domain visualization by Čerenkov-type second harmonic generation. *Opt. Express* **2010,** *18* (16), 16539-16545.

137. Roppo, V.; Kalinowski, K.; Sheng, Y.; Krolikowski, W.; Cojocaru, C.; Trull, J., Unified approach to Cerenkov second harmonic generation. *Opt. Express* **2013,** *21* (22), 25715-25726.

138. Ling, X.; Fang, W.; Lee, Y. H.; Araujo, P. T.; Zhang, X.; Rodriguez-Nieva, J. F.; Lin, Y.; Zhang, J.; Kong, J.; Dresselhaus, M. S., Raman enhancement effect on two-dimensional layered materials: graphene, h-BN and MoS_2. *Nano Lett.* **2014,** *14* (6), 3033-3040.

139. Ling, X.; Wu, J.; Xu, W.; Zhang, J., Probing the effect of molecular orientation on the intensity of chemical enhancement using graphene-enhanced Raman spectroscopy. *Small* **2012,** *8* (9), 1365-1372.

140. Sun, L.; Hu, H.; Zhan, D.; Yan, J.; Liu, L.; Teguh, J. S.; Yeow, E. K. L.; Lee, P. S.; Shen, Z., Plasma Modified MoS_2 Nanoflakes for Surface Enhanced Raman Scattering. *Small* **2014,** *10* (6), 1090-1095.

141. Puretzky, A. A.; Liang, L.; Li, X.; Xiao, K.; Wang, K.; Mahjouri-

Samani, M.; Basile, L.; Idrobo, J. C.; Sumpter, B. G.; Meunier, V.; Geohegan, D. B., Low-Frequency Raman Fingerprints of Two-Dimensional Metal Dichalcogenide Layer Stacking Configurations. *ACS Nano* **2015,** *9* (6), 6333-6342.

142. Farag, A. A. M., Optical absorption studies of copper phthalocyanine thin films. *Opt. Laser Technol.* **2007,** *39* (4), 728-732.

143. Jiang, N.; Foley, E. T.; Klingsporn, J. M.; Sonntag, M. D.; Valley, N. A.; Dieringer, J. A.; Seideman, T.; Schatz, G. C.; Hersam, M. C.; Van Duyne, R. P., Observation of multiple vibrational modes in ultrahigh vacuum tip-enhanced Raman spectroscopy combined with molecular-resolution scanning tunneling microscopy. *Nano Lett.* **2012,** *12* (10), 5061-5067.

144. Padgaonkar, S.; Amsterdam, S. H.; Bergeron, H.; Su, K.; Marks, T. J.; Hersam, M. C.; Weiss, E. A., Molecular-Orientation-Dependent Interfacial Charge Transfer in Phthalocyanine/MoS_2 Mixed-Dimensional Heterojunctions. *J. Phys. Chem. C* **2019,** *123* (21), 13337-13343.

145. Greulich, K.; Belser, A.; Bölke, S.; Grüninger, P.; Karstens, R.; Sättele, M. S.; Ovsyannikov, R.; Giangrisostomi, E.; Basova, T. V.; Klyamer, D.; Chassé, T.; Peisert, H., Charge Transfer from Organic Molecules to Molybdenum Disulfide: Influence of the Fluorination of Iron Phthalocyanine. *J. Phys. Chem. C* **2020,** *124* (31), 16990-16999.

146. Yin, Y.; Miao, P.; Zhang, Y.; Han, J.; Zhang, X.; Gong, Y.; Gu, L.; Xu, C.; Yao, T.; Xu, P.; Wang, Y.; Song, B.; Jin, S., Significantly Increased Raman Enhancement on MoX_2 (X = S, Se) Monolayers upon Phase Transition. *Adv. Funct. Mater.* **2017,** *27* (16).

147. Dong, H.; Zhu, H.; Meng, Q.; Gong, X.; Hu, W., Organic photoresponse materials and devices. *Chem Soc Rev* **2012,** *41* (5), 1754-808.

148. Kim, J.-S.; Ho, P. K. H.; Greenham, N. C.; Friend, R. H., Electroluminescence emission pattern of organic light-emitting diodes: Implications for device efficiency calculations. *J. Appl. Phys.* **2000,** *88* (2), 1073-1081.

149. Kazantsev, M. S.; Konstantinov, V. G.; Dominskiy, D. I.; Bruevich, V. V.; Postnikov, V. A.; Luponosov, Y. N.; Tafeenko, V. A.; Surin, N. M.; Ponomarenko, S. A.; Paraschuk, D. Y., Highly bendable luminescent semiconducting organic single crystal. *Synth. Met.* **2017,** *232*, 60-65.

150. Curto, A. G.; Taminiau, T. H.; Volpe, G.; Kreuzer, M. P.; Quidant, R.; van Hulst, N. F., Multipolar radiation of quantum emitters with nanowire optical antennas. *Nat. Commun.* **2013,** *4*, 1750.

151. Shegai, T.; Miljković, V. D.; Bao, K.; Xu, H.; Nordlander, P.; Johansson, P.; Käll, M., Unidirectional Broadband Light Emission from Supported Plasmonic Nanowires. *Nano Lett.* **2011,** *11* (2), 706-711.

152. Taminiau, T. H.; Stefani, F. D.; Segerink, F. B.; van Hulst, N. F., Optical antennas direct single-molecule emission. *Nat. Photonics* **2008,** *2* (4), 234-237.

153. Coenen, T.; Bernal Arango, F.; Femius Koenderink, A.; Polman, A., Directional emission from a single plasmonic scatterer. *Nat. Commun.* **2014,** *5*, 3250.

154. Coenen, T.; Vesseur, E. J.; Polman, A.; Koenderink, A. F., Directional emission from plasmonic Yagi-Uda antennas probed by angle-resolved cathodoluminescence spectroscopy. *Nano Lett.* **2011,** *11* (9), 3779-3784.

155. Kim, J.; Zhao, H.; Hou, S.; Khatoniar, M.; Menon, V.; Forrest, S. R., Using Fourier-Plane Imaging Microscopy for Determining Transition-Dipole-Moment Orientations in Organic Light-Emitting Devices. *Phys. Rev. Applied.* **2020,** *14* (3), 034048.

156. Kim, J.; Hou, S.; Zhao, H.; Forrest, S. R., Nanoscale Mapping of Morphology of Organic Thin Films. *Nano Lett.* **2020,** *20* (11), 8290-8297.

157. Borshchev, O. V.; Skorotetcky, M. S.; Trukhanov, V. A.; Fedorenko, R. S.; Surin, N. M.; Svidchenko, E. A.; Sosorev, A. Y.; Kazantsev, M. S.; Paraschuk, D. Y.; Ponomarenko, S. A., Synthesis, characterization and organic field-effect transistors applications of novel tetrathienoacene derivatives. *Dyes*

Pigments **2021,** *185*.

158. Maslennikov, D. R.; Sosorev, A. Y.; Fedorenko, R. S.; Luponosov, Y. N.; Ponomarenko, S. A.; Bruevich, V. V., Surface-Enhanced Raman Spectroscopy of 2D Organic Semiconductor Crystals. *J. Phys. Chem. C* **2019,** *123* (44), 27242-27250.

159. Bruevich, V. V.; Glushkova, A. V.; Poimanova, O. Y.; Fedorenko, R. S.; Luponosov, Y. N.; Bakirov, A. V.; Shcherbina, M. A.; Chvalun, S. N.; Sosorev, A. Y.; Grodd, L.; Grigorian, S.; Ponomarenko, S. A.; Paraschuk, D. Y., Large-Size Single-Crystal Oligothiophene-Based Monolayers for Field-Effect Transistors. *ACS Appl. Mater. Interfaces* **2019,** *11* (6), 6315-6324.

160. Loi, M. A.; da Como, E.; Dinelli, F.; Murgia, M.; Zamboni, R.; Biscarini, F.; Muccini, M., Supramolecular organization in ultra-thin films of α-sexithiophene on silicon dioxide. *Nat. Mater.* **2004,** *4* (1), 81-85.

Résumé

1. Fondements théoriques

Les techniques de microscopie et de spectroscopie SHG sont devenues un sujet considérable dans les caractérisations structurales des matériaux TMDCs. Le processus SHG a été démontré pour la première fois par Franken et al en 1961. La Figure 1.1 présente un processus SHG, où deux photons incidents à la fréquence optique ω fournis par un laser pulsé ultrarapide sont médiés par les deux états virtuels, puis deux photons sont convertis en un photon émis à la fréquence optique de $\omega_{SHG} = 2\omega$. SHG appartient à un processus de diffusion cohérente non linéaire du second ordre, qui provient de la polarisation induite au lieu de l'absorption des photons. La polarisation induite non linéaire du second ordre $P_{SHG}^{(2)}(2\omega_1)$ s'écrit:

$$P_{SHG}^{(2)}(2\omega_1) = \varepsilon_0 \chi^{(2)} E_1 E_1$$

Ici, le tenseur de susceptibilité du second ordre est représenté par $\chi^{(2)}$, qui est responsable du processus SHG.

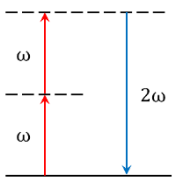

Figure 1.1: Diagramme de niveau d'énergie du processus de génération de deuxième harmonique (SHG).

Les matériaux TMDC ont normalement deux polytypes, à savoir la phase 2H hexagonale et la phase 3R rhomboédrique. Les diagrammes schématiques des

structures cristallines des matériaux TMDC en phase 2H et en phase 3R sont illustrés respectivement sur les Figures 1.2(a) et (b). Pour les TMDC multicouches ou en vrac à phase 2H, les flocons avec des couches paires sont centrosymétriques, où les couches voisines montrent l'orientation inversée et les dipôles de deuxième harmonique (SH) antiparallèles. Au contraire, la multicouche ou la masse des TMDC de phase 3R appartiennent à la symétrie du groupe de points C_{3v}, et la couche individuelle est déterminée comme étant la phase 2H. Les couches adjacentes de flocons de phase 3R sont orientées parallèlement mais se déplacent le long de la direction dans le plan, ce qui conduit à l'interférence constructive de la polarisation SH.

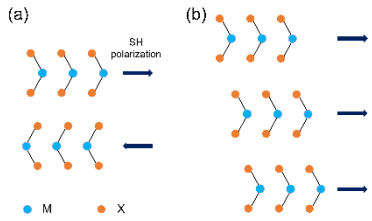

Figure 1.2: Vue latérale de la structure cristalline de la phase 2H hexagonale et de la phase 3R rhomboédrique MX_2.

Le signal 2PPL des ions Eu(Ⅱ) dans CaF_2:Eu excité par le laser à rubis de Maiman a été observé pour la première fois expérimentalement par Kaiser et Garret en 1961, et l'intensité 2PPL est proportionnelle au carré de l'intensité du laser. La Figure 1.3 présente un dessin schématique du processus 2PPL, un phénomène optique non linéaire du troisième ordre qui contient l'absorption simultanée de deux photons à la même fréquence ω via un état virtuel (appelé absorption à deux photons), la relaxation rapide de l'électron excité à l'étape d'équilibre thermique, et enfin la recombinaison radiative d'un électron à l'état émetteur avec un trou à l'état fondamental en terme de photoluminescence (PL).

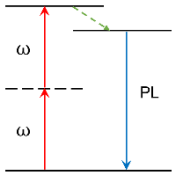

Figure 1.3: Diagramme des niveaux d'énergie du processus de photoluminescence induite par deux photons (2PPL).

Les différents événements optiques peuvent être déclenchés lorsque la lumière laser interagit avec la matière. Ces événements contiennent l'absorption, l'émission et la diffusion, qui sont liées aux transitions avec les états électroniques, vibrationnels et rotationnels du milieu. Les processus de diffusion sont en termes de diffusion élastique et de diffusion inélastique. La diffusion Raman vibrationnelle provient à l'origine de la diffusion inélastique de la lumière par des molécules ou des matériaux, où l'énergie des photons diffusés E_S n'est pas égale à l'énergie des photons incidents E_I. La compréhension de la structure chimique des molécules peut être fournie en étudiant le spectre Raman. La Figure 1.4(a) montre un diagramme de niveau d'énergie illustrant la diffusion Stokes Raman, qui nécessite la relation suivante:

$$E_S = E_I - \hbar\omega_{vib}$$

Les processus de diffusion anti-Stokes Raman, comme le montre la Figure 1.4(b), nécessitent la relation suivante:

$$E_S = E_I + \hbar\omega_{vib}$$

Les décalages Raman sont exprimés en nombres d'onde et notés $\Delta\bar{\nu}_R$, qui est calculé par $\Delta\bar{\nu}_R = \hbar\omega_{vib}/hc$, où h est la constante de Planck, et c est la vitesse de la lumière. De plus, l'effet de la diffusion Raman devient intense lorsque l'énergie du photon incident correspond à l'énergie électronique de la molécule, appelée diffusion Raman par résonance (RRS), comme illustré à la Figure 1.4(c).

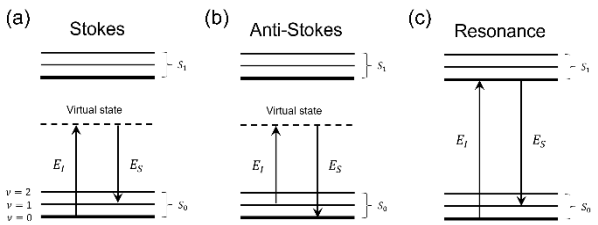

Figure 1.4 Diagrammes des niveaux d'énergie de (a) Stokes Raman, (b) anti-Stokes Raman et (c) des processus de diffusion Raman par résonance.

En général, l'effet SERS résulte de l'amélioration de la diffusion Raman à partir de molécules adsorbées à la surface des substrats SERS tels que les nanoparticules métalliques, les surfaces métalliques rugueuses, le graphène et les matériaux TMDC. Deux effets principaux, dont le mécanisme électromagnétique et le mécanisme chimique, donnent lieu à l'effet SERS. Le mécanisme électromagnétique est généralement lié à l'effet de résonance plasmonique de surface localisée (LSPR) qui est entraîné par l'interaction de la lumière avec les nanoparticules métalliques, et le mécanisme chimique est lié au processus dit de transfert de charge entre les substrats SERS et les molécules adsorbées.

Les diverses propriétés photophysiques, par exemple l'intensité d'émission et la durée de vie de l'état d'émission, d'une molécule individuelle dépendent de manière sensible de l'orientation du moment dipolaire d'émission de la molécule. Dans le passé, l'orientation tridimensionnelle du moment d'émission-dipôle avait été déterminée par plusieurs méthodes telles que l'analyse de polarisation des signaux de fluorescence et la visualisation de l'image de fluorescence défocalisée. Récemment, une approche prometteuse, en plaçant un détecteur de photons au plan focal arrière de l'objectif pour imager le diagramme d'émission radiative, est devenue un point chaud intéressant pour déterminer l'orientation du dipôle d'émission.

Dans un espace libre, un seul dipôle montre un diagramme de rayonnement non isotrope. Les modèles tridimensionnels d'un dipôle individuel avec trois

orientations différentes sont illustrés à la Figure 1.5. L'orientation d'un dipôle individuel est exprimée par une coordonnée sphérique $P(\Phi, \Theta)$, comme illustré sur la Figure 1.5(b). L'axe optique est défini le long de la direction de l'axe z. Selon le modèle d'un dipôle hertzien, un seul dipôle dans un espace libre peut émettre l'intensité la plus élevée dans les angles perpendiculaires au moment dipolaire, comme le montre la Figure 1.5.

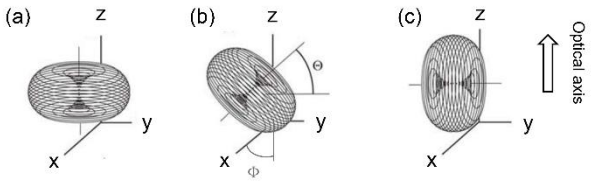

Figure 1.5: Diagramme de rayonnement tridimensionnel d'un seul dipôle. L'axe optique est défini le long de l'axe z. Adapté de Brokmann et al.

2. Méthodes

Le dessin schématique de la microscopie optique confocale est illustré à la Figure 2.1. Dans le trajet du faisceau d'excitation, un nouveau laser, un laser à fibre d'erbium ultra-rapide (pro NIR_02508, Toptica Photonic) avec une longueur d'onde d'excitation de 780 nm (fréquence de répétition de 40 MHz et durée d'impulsion de 89,9 fs), est intégré à la microscopie. Le faisceau laser est purifié via un filtre passe-long de 650 nm et expansé via deux télescopes (T1 et T2). La taille du faisceau laser élargi doit correspondre à la dimension du miroir parabolique (diamètre: 2 cm). Pour obtenir un mode gaussien homogène, la polarisation indésirable et la lumière diffusée sont filtrées en utilisant un filtre spatial de 15 µm positionné au foyer du télescope 2 (T2). Le faisceau laser est réfléchi via un séparateur de faisceau dichroïque passe-court multiphoton non polarisant 50:50 vers le miroir parabolique. Ensuite, le faisceau laser est focalisé jusqu'à un point lumineux à diffraction limitée sur l'échantillon par le miroir parabolique. L'échantillon est fixé sur le porte-échantillon maison qui est placé sur un scanner piézoélectrique XYZ (P-517K008, Physik

Instrumente). Les signaux optiques sont collimatés et collectés par le miroir parabolique puis traversent le séparateur de faisceau. Dans le trajet du faisceau de détection, la taille du faisceau laser est diminuée par le télescope 3 (T3). Un filtre spatial en T3 est utilisé pour filtrer la lumière diffusée. Avec un miroir basculant, les signaux optiques peuvent être dirigés vers un spectromètre couplé à une caméra à dispositif à couplage de charge (CCD) refroidi thermoélectriquement (Acton SP 2500, Princeton Instruments) ou vers des diodes micro-photon (MPD, MPD-PD-100- CTD, Micro Photon Diodes Srl). La fenêtre de détection va de 375 nm à 700 nm. Les signaux optiques sont purifiés par un filtre passe-bas à 720 nm avant d'entrer dans le spectromètre pour la collecte spectrale. Pour obtenir l'image SHG, un filtre passe-bande de 10 nm est placé devant MPD (voir Figure 2.1). Pour obtenir l'image 2PPL, un filtre passe-long de 488 nm et un filtre passe-court de 680 nm sont utilisés pour filtrer le signal SHG et la lumière diffusée élastique.

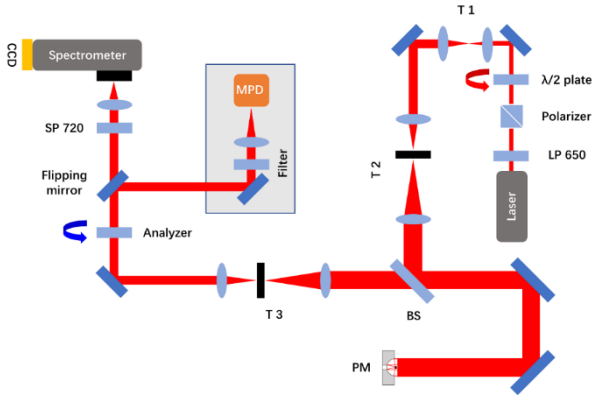

Figure 2.1: Dessin schématique de la microscopie optique confocale assistée par miroir parabolique maison.

Les mesures Raman et PL sont également réalisées avec la microscopie confocale à balayage assistée par miroir parabolique. La configuration optique de cette microscopie est similaire à celle illustrée à la Figure 2.1. Dans ce microscope, un laser à diode de 532 nm (NANO 250-532 max, QIOPTIQ) ou un laser à diode de 636 nm (PDL 800-D, Picoquant) fonctionnant en mode CW est couplé à la microscopie. Le faisceau laser est purifié via un filtre passe-

bande qui est placé directement après la sortie du laser. La lumière diffusée élastique est filtrée à l'aide d'une combinaison de deux filtres coupe-bande qui sont positionnés devant les détecteurs. Avec un miroir basculant à distance, les signaux optiques peuvent être détectés soit par une photodiode à avalanche (APD, SPCM-AQR-14, Perkin Elmer) pour obtenir l'image optique, soit par un spectromètre couplé à une caméra CCD refroidie à l'azote liquide (Acton Research, SpectraPro 300i, Perkin Elmer) pour la collecte des spectres optiques.

Des modes laser d'ordre supérieur, à savoir des modes en anneau polarisés azimutalement et radialement, sont utilisés dans les mesures de dépendance à la polarisation d'excitation. L'esquisse de la conversion de mode est illustrée à la Figure 2.2(a). La ligne pointillée représente l'axe optique du trajet du faisceau. Le faisceau laser en mode gaussien peut être converti en modes polarisés azimutalement ou radialement via le convertisseur de mode. Le faisceau laser est élargi avec un télescope impliquant deux lentilles doublets achromatiques. Le grossissement du faisceau laser doit être pris en compte afin de remplir l'ouverture du miroir parabolique. Pour générer idéalement un mode azimutal ou radial, d'autres modes indésirables et la lumière diffusée seront supprimés en positionnant un trou d'épingle à la position du foyer de la lumière. La Figure 2.2(b) montre la conversion de mode avec un convertisseur de mode maison (MC). Les flèches blanches étiquetées en modes azimutal, radial et gaussien indiquent la direction de polarisation de la lumière. Le convertisseur de mode contient quatre quarts de lames demi-onde. L'axe rapide (ligne blanche) est disposé différemment, comme le montre la Figure 2.2(b). La lumière diffusée de manière aléatoire depuis les bords des plaques demi-onde peut être filtrée par le trou d'épingle. En tournant le convertisseur de mode de 90°, le mode laser généré peut être commuté du mode radial au mode azimutal.

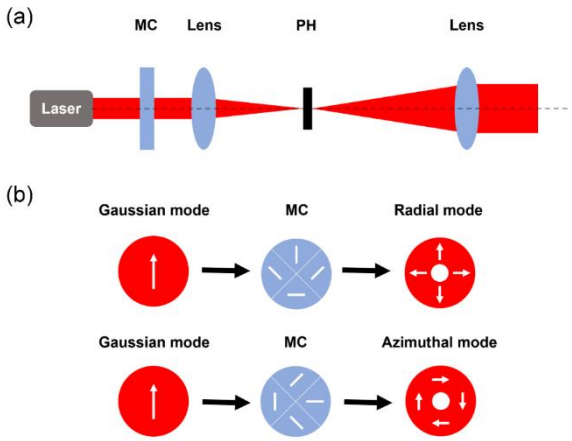

Figure 2.2: (a) Schéma du trajet du faisceau optique pour une conversion de mode du mode gaussien au mode laser d'ordre supérieur. MC: convertisseur de mode; PH: Sténopé. (b) Modes radial et azimutal générés à partir du mode gaussien avec un convertisseur de mode.

Le dessin schématique pour l'imagerie directionnelle du diagramme d'émission est illustré à la Figure 2.3. La microscopie d'imagerie de l'espace k est mise en œuvre dans la microscopie confocale à balayage qui a été introduite dans la Figure 2.1. Le faisceau laser entrant (780 nm, laser pulsé fs) est focalisé sur l'échantillon par le miroir parabolique et les émissions (marquées par des lignes rouges et bleues) sont collectées et également collimatées par le même miroir parabolique, comme le montre la Figure 2.3. Le faisceau collimaté est focalisé par l'objectif 1 et le plan image (IP) est créé à la distance f1 (la distance focale de l'objectif 1). Le diagramme d'émission peut être généré avec la lentille 2, qui projette la transformée de Fourier de l'IP. Le dispositif à couplage de charge multiplicateur d'électrons (EMCCD, Andor, iXon Ultra 888) est placé à la position du plan focal de la lentille 2. Le filtre passe-court est directement monté devant le détecteur pour éliminer la lumière diffusée par le laser. Ainsi, le motif inélastique directionnel peut être projeté à travers le relais de la lentille 1 et de la lentille 2 au EMCCD.

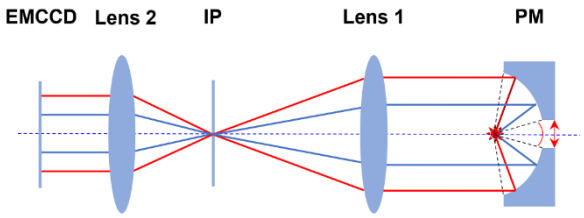

Figure 2.3: Dessin schématique pour l'imagerie des modèles d'émission en utilisant le miroir parabolique (PM) comme élément de focalisation laser et de collecte de signal.

Le maximum d'angle hors plan collecté θ par rapport à l'axe optique est calculé jusqu'à $\sim 87°$ en raison d'un NA de 0.9986 dans l'air. La présence d'une région interdite dans PM est indiquée par une flèche rouge à double extrémité sur la Figure 2.3. La perte de collecte de signal est due au porte-échantillon à un bras et au trou au centre du PM. L'angle minimum θ est calculé à $\sim 27°$. Ainsi, l'angle de collecte autorisé θ est compris entre $\sim 27°$ et $\sim 87°$.

Les propriétés optiques non linéaires des antennes Yagi-Uda (YU) sont mesurées à la microscopie optique d'imagerie de l'espace k à l'aide d'un faisceau laser polarisé linéairement. Des réseaux d'antennes YU sont fabriqués sur un substrat de verre en utilisant la lithographie par faisceau d'électrons. La Figure 2.4(a) montre l'image optique non linéaire d'un réseau d'antennes YU, où la distance d'espacement de 1 µm entre l'antenne YU adjacente est bien observée. L'encart de la Figure 2.4(a) montre la configuration structurelle d'une seule antenne YU. L'antenne comprend trois éléments (un réflecteur d'une longueur de 110 nm, une alimentation d'une longueur de 70 nm et trois directeurs d'une longueur de 50 nm). La Figure 2.4(b) montre la carte d'intensité optique codée par couleur, où les mesures optiales dépendant de la polarisation sont effectuées en faisant tourner la direction de polarisation de la lumière laser à l'aide d'une lame demi-onde. Les maxima d'intensité optique sont obtenus lorsque la lumière laser est polarisée le long de l'axe longitudinal de l'élément (par exemple, réflecteur dans l'antenne YU). La Figure 2.4(c) montre les spectres optiques de l'antenne YU sous deux configurations

expérimentales comme illustré dans l'encart. La réponse optique est à peine visible lorsque la lumière laser est polarisée le long du petit axe du réflecteur dans l'antenne YU; tandis qu'une photoluminescence métallique intense et un faible pic SHG sont observés lorsque la polarisation de la lumière laser est orientée le long de l'axe long du réflecteur dans l'antenne YU. Compte tenu de l'intensité optique dépendante de la polarisation, les mesures du diagramme d'émission sont effectuées lorsque la lumière laser est polarisée le long du grand axe du réflecteur dans l'antenne YU. Le diagramme d'émission obtenu à partir d'une seule antenne YU est presque isotrope, comme le montre la Figure 2.4(d). De plus, le rapport signal sur bruit est adéquat pour visualiser la directionnalité d'émission d'une seule antenne YU. En résumé, la microscopie d'imagerie de l'espace k a été mise en œuvre dans la microscopie optique confocale, qui est sensible pour détecter l'image optique, la réponse spectrale et le modèle d'émission angulaire au niveau de l'émetteur unique.

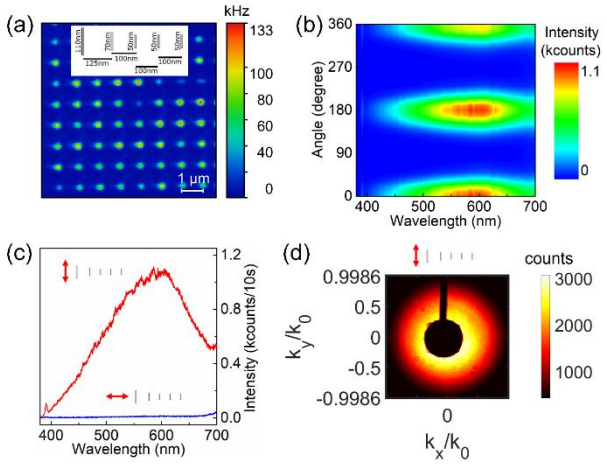

Figure 2.4: (a) Image optique non linéaire d'un réseau d'antennes YU. L'encart est la configuration structurelle d'une antenne YU. (b) La dépendance de l'intensité optique sur la polarisation du faisceau laser de l'antenne YU. (c) Les spectres optiques obtenus à partir de l'antenne YU. (d) Le diagramme d'émission expérimental collecté à partir de l'antenne YU.

3. Émission SHG améliorée par les bords dans la monocouche WS_2

Une image AFM d'un flocon WS_2 monocouche en forme de triangle sur un substrat SiO_2 (épaisseur: 300 nm)/Si est illustrée à la Figure 3.1(a). L'encart de la Figure 3.1(a) représente le profil de hauteur topographique qui est tiré de la position marquée par la ligne blanche en pointillés de la Figure 3.1(a). L'épaisseur de 0.75 nm suggère que le flocon WS_2 mesuré est bien monocouche. Des particules alignées le long des bords du flocon sont observables, ce qui a été déterminé comme étant les produits intermédiaires (WO_xS_y) au cours de la croissance chimique WS_2. La Figure 3.1(b) montre le spectre PL obtenu à partir de la monocouche WS_2, qui est excitée par un laser CW à 532 nm. L'émission à 640 nm provient principalement de la transition excitonique directe entre la bande de conduction la plus basse et la bande de valence la plus élevée.

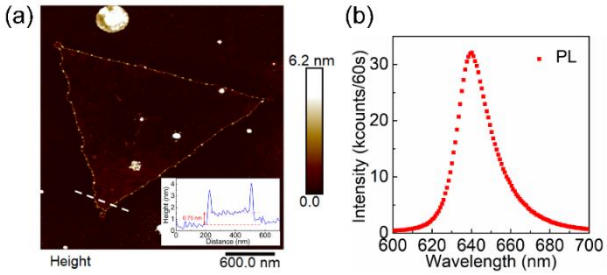

Figure 3.1: Les caractérisations d'un éclat WS_2 monocouche.

Pour étudier les propriétés optiques non linéaires des flocons WS_2, les échantillons sont excités par un laser pulsé femtoseconde avec une longueur d'onde de 780 nm. Les Figures 3.2(a) et (b) montrent les images optiques SHG et 2PPL (taille de balayage: 4 μm × 4 μm) de la même monocouche triangulaire WS_2 étudiée à la Figure 3.2, respectivement. Il est évident que les intensités SHG sont les plus fortes sur les bords, tandis que le signal 2PPL est le plus élevé à l'intérieur de la monocouche WS_2.

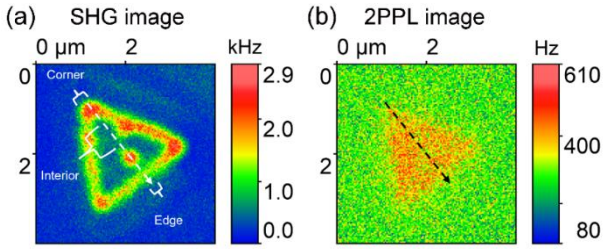

Figure 3.2: Propriétés optiques non linéaires pour le flocon monocouche WS_2.

Pour comparer précisément les intensités optiques SHG et 2PPL à la même position de la monocouche WS_2, les spectres optiques SHG et 2PPL sont mesurés le long des lignes blanches et moirés en pointillés indiquées sur la Figure 3.2(a) et (b), respectivement. Les intensités spectrales SHG et 2PPL codées par couleur sont présentées respectivement dans les panneaux gauche et droit de la Figure 3.3(a). Sur la Figure 3.3(b), les intensités SHG et 2PPL spectralement intégrées en fonction de la séquence spectrale sont également présentées sous forme de courbes bleues et rouges, respectivement. La corrélation entre les intensités SHG et 2PPL intégrées est visualisée. Les comparaisons en (a) et (b) montrent clairement que la plus forte intensité de SHG apparaît au coin du flocon WS_2 est observable, là où se situe le signal 2PPL le plus faible. En particulier, nous montrons l'anticorrélation entre les signaux optiques SHG et 2PPL à l'emplacement marqué par le rectangle vert sur la Figure 3.3(b).

De plus, trois spectres SHG et 2PPL enregistrés au coin, à l'intérieur et au bord de la monocouche WS_2 sont présentés à la Figure 3.3(c). Les positions des coins, de l'intérieur et des bords sont marquées par les flèches orange sur la Figure 3.3(b). L'intensité SHG au coin est jusqu'à deux fois plus forte que celle à l'intérieur; tandis que l'intensité 2PPL au coin est plus faible que celle de la région intérieure. Les tracés dépendant de la puissance d'excitation des intensités intégrées spectralement de 380 nm à 400 nm (SHG, carrés bleus) et de 600 nm à 680 nm (2PPL, cercles rouges) sont illustrés à la Figure 3.3(d).

On peut voir que les signaux SHG et 2PPL montrent des dépendances de puissance quadratiques, ce qui suggère que les deux signaux proviennent de processus optiques non linéaires induits par deux photons.

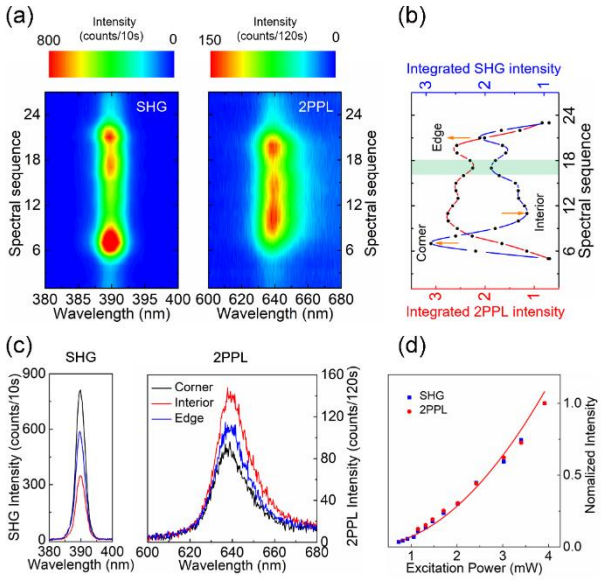

Figure 3.3: La corrélation entre les intensités SHG et 2PPL du même flocon WS_2 monocouche.

Ce n'est que récemment que l'émission SHG améliorée par les bords sur la monocouche MoS_2 a été rapportée par Yin et al et Lin et al. Ils ont attribué le SHG amélioré par les bords observé à la présence d'états électroniques localisés à mi-écart qui ont été calculés à l'aide de la théorie de la fonction de densité (DFT). L'amélioration SHG était très sensible à la longueur d'onde d'excitation ainsi qu'au type de bord, c'est-à-dire bord S-zigzag et bord S-Mo Klein. Ici, nous suivons la même considération pour traiter nos résultats. Dans notre travail, nous observons clairement une émission efficace de bord SHG sur les flocons WS_2 lorsque la longueur d'onde d'excitation de 780 nm est utilisée. Ce phénomène démontre que de nouveaux états d'énergie intermédiaires entre la bande de valence et la bande de conduction se sont probablement formés, en raison de la rupture de la symétrie translationnelle et des défauts structurels aux bords de la monocouche WS_2. Les nouveaux états d'énergie à mi-écart pourraient coïncider presque avec l'un des états virtuels

du processus SHG, donc la susceptibilité non linéaire de second ordre $\chi^{(2)}$ aux bords du flocon WS_2 devient grande selon la mécanique quantique.

La spectroscopie 2PPL à température ambiante est également utilisée pour caractériser les propriétés structurales des flocons WS_2. En raison du processus optique non linéaire de troisième ordre de 2PPL, les intensités de 2PPL sont extrêmement faibles par rapport à celles de la réponse PL, comme le montrent la Figure 3.1(b) et la Figure 3.3(c). Habituellement, la spectroscopie PL est une méthode fiable et rapide pour l'identification des propriétés structurelles. Les défauts structurels d'un matériau agissent comme des canaux de recombinaison non radiatifs pour éteindre les intensités PL. Dans les résultats précédents de la monocouche WS_2 développée par CVD, les caractéristiques PL inhomogènes, c'est-à-dire le décalage de pic et l'assombrissement dans certaines régions, sont attribuées à davantage de défauts structurels (par exemple, les lacunes en S). Dans notre étude, nous observons une trempe 2PPL au bord et au coin de la monocouche WS_2. Ces phénomènes sont probablement provoqués par les défauts structurels tels que développés, c'est-à-dire les défauts de bord et de point. Les diminutions des intensités 2PPL sont principalement dues à la transition de la structure électronique de la bande interdite directe à indirecte et à l'effet des excitons liés aux défauts.

4. Orientation cristalline et joints de grains dans le flocon de $MoSe_2$

Pour démontrer l'orientation cristalline du flocon $MoSe_2$, nous nous concentrons sur la région, où les flocons $MoSe_2$ individuels avec différentes géométries peuvent être vus. Sur la Figure 4.1(a), des flocons de $MoSe_2$ triangulaires et en étoile à six branches peuvent être clairement observés. Comme les propriétés 2PPL sont très sensibles à l'épaisseur des flocons, nous

effectuons d'abord la mesure d'imagerie 2PPL. Dans la Figure 4.1(b), ces flocons de $MoSe_2$ montrent une intensité homogène de 2PPL, ce qui indique que les flocons de $MoSe_2$ dans la zone ont probablement les mêmes épaisseurs. La Figure 4.1(c) montre l'image SHG des mêmes flocons de $MoSe_2$, où les signaux SHG sont collectés sans analyseur placé devant le détecteur lorsque les flocons de $MoSe_2$ sont excités avec un laser à impulsions polarisées linéairement.

Pour illustrer la corrélation entre la réponse SHG et l'orientation cristalline du flocon de $MoSe_2$, un schéma est présenté à la Figure 4.1(d). La direction du fauteuil (AC, flèche orange) du flocon $MoSe_2$ est à un angle θ par rapport au champ électrique laser $\vec{E}(\omega)$ (flèche rouge). Ici, l'angle θ représente l'orientation du cristal par rapport à la direction de polarisation du laser. Comme le flocon de $MoSe_2$ monocouche appartient au groupe ponctuel D_{3h}, la plage d'angle θ est de $0°$ à $60°$. Il est rapporté que le champ électrique SH généré $\vec{E}(2\omega)$ (flèche bleue) est à un angle 3θ (de $0°$ à $180°$) par rapport au champ électrique laser $\vec{E}(\omega)$, comme indiqué dans Figure 4.1(d). Dans les mesures d'imagerie SHG polarisées, la direction de polarisation du laser et l'orientation des flocons sont fixes; tandis que la direction de polarisation du signal SHG généré est analysée par un polariseur linéaire. Dans la Figure 4.1(d), la composante SHG polarisée x (polarisée y) (flèche grise en pointillés) est obtenue dans la configuration expérimentale, où l'axe de transmission du polariseur est positionné parallèlement (perpendiculaire) à la direction de polarisation de la lumière laser. Les Figures 4.1(e) et (f) représentent les images SHG utilisant respectivement la composante polarisée x et polarisée y des signaux SHG pour le flocon $MoSe_2$. Il est clairement observé que certains flocons de $MoSe_2$ brillants dans l'image SHG polarisée x (Figure 4.1(e)) apparaissent sombres dans l'image SHG polarisée y (Figure 4.1(f)). Le champ SH généré $\vec{E}(2\omega)$ peut être estimé à travers le signal SHG du flocon $MoSe_2$

dans les images SHG polarisées. Lorsque l'angle 3θ est compris entre $0°$ et $45°$ ou entre $135°$ et $180°$, les flocons de $MoSe_2$ peuvent être brillants dans l'image SHG polarisée x; tandis que l'angle 3θ est compris entre $45°$ et $135°$, les flocons de $MoSe_2$ sont brillants dans l'image SHG polarisée y.

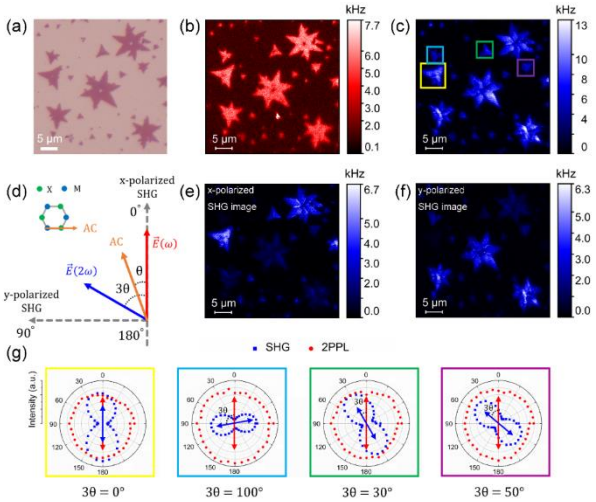

Figure 4.1: Orientation des cristaux déterminée par imagerie SHG polarisée et dépendance angulaire des intensités SHG.

Pour explorer davantage les orientations cristallines sous-jacentes des flocons $MoSe_2$ individuels, une spectroscopie optique SHG dépendante de la polarisation est effectuée. Les flocons de $MoSe_2$ mesurés sont marqués par des carrés bleus, verts, jaunes et violets illustrés à la Figure 4.1(c), et les intensités SHG (intégrées spectralement de 380 nm à 400 nm) collectées à différents angles du polariseur linéaire sont indiquées comme le tracés polaires sur la Figure 4.1(g). La direction de polarisation du laser et la direction de polarisation SHG générée sont représentées respectivement par la flèche rouge à double extrémité et la flèche bleue. On observe clairement que les flocons de $MoSe_2$ mesurés présentent des SHG polarisés linéairement. La direction de polarisation du SHG généré n'est pas identique à celle de la lumière laser. D'après les résultats expérimentaux illustrés à la Figure 4.1(g), on constate que les quatre flocons de $MoSe_2$ mesurés présentent des différences distinctes dans l'angle 3θ entre le champ SH généré $\vec{E}(2\omega)$ et le

champ électrique laser $\vec{E}(\omega)$, qui suggère les différences d'angle θ pour les quatre flocons mesurés. Les résultats sont attribués aux différentes orientations cristallines des flocons de $MoSe_2$ par rapport à la direction de polarisation de la lumière laser. Cependant, l'orientation exacte du cristal (Mo-Se ou Se-Mo) n'a pas pu être déterminée avec succès, ce qui est attribué à la perte d'informations de phase dans les mesures SHG dépendantes de la polarisation. De plus, les intensités 2PPL dépendantes de l'angle intégrées spectralement de 400 nm à 700 nm des quatre flocons de $MoSe_2$ sont également tracées, comme le montre la Figure 4.1(g) sous forme de points rouges. Les signaux 2PPL montrent un modèle d'émission presque parfaitement circulaire, ce qui démontre clairement que le signal 2PPL émis par le flocon $MoSe_2$ n'est pas polarisé. Le motif 2PPL isotrope observé est dû à la forte symétrie de structure dans le plan du flocon de $MoSe_2$, qui conduit à une réponse isotrope dans le plan à la direction de polarisation de la lumière laser.

L'orientation cristalline des grains voisins dans un flocon de $MoSe_2$ est également étudiée par la dépendance à la polarisation de la spectroscopie SHG. L'image SHG d'un flocon de $MoSe_2$ est présentée sur la Figure 4.2(a), qui contient six grains joints. Fait intéressant, des signaux SHG plus brillants le long des frontières entre les grains sont observés par rapport à ceux à l'intérieur des grains individuels. Trois tracés polaires SHG mesurés sur les trois grains voisins du flocon $MoSe_2$ sont présentés sur la Figure 4.2(b). Les positions exactement mesurées marquées par P1, P2 et P3 sont illustrées à la Figure 4.2(a). Les flèches rouges et bleues à double extrémité de la Figure 4.2(b) représentent respectivement la direction de polarisation du laser et la direction de polarisation SHG générée. La direction de polarisation linéaire du SHG généré est clairement visible à partir des trois grains adjacents du flocon de $MoSe_2$. Notamment, les champs SH $\vec{E}(2\omega)$ générés à partir des trois grains voisins (P1, P2 et P3) ont tous à peu près le même angle 3θ (définition vue

sur la Figure 4.2(d)) par rapport au champ électrique laser $\vec{E}(\omega)$ soit environ $30°$. Fait intéressant, aucun type de variation d'intensité de ce type ne peut être observé au niveau de ces lignes adjointes dans l'image 2PPL de ce flocon de $MoSe_2$, comme le montre la Figure 4.2(c). Ces différents phénomènes peuvent être bien visualisés par les spectres SHG et 2PPL collectés le long de la ligne blanche en pointillés qui est marquée sur la Figure 4.2(c). Les cartes d'intensité à code couleur SHG et 2PPL sont illustrées à la Figure 4.2(d), où l'intensité SHG est intégrée spectralement de 380 nm à 400 nm, et l'intensité 2PPL est intégrée spectralement de 400 nm à 700 nm. Alors que les signaux SHG montrent de nettes variations aux adjonctions entre deux grains, l'intensité 2PPL est homogène dans ces régions.

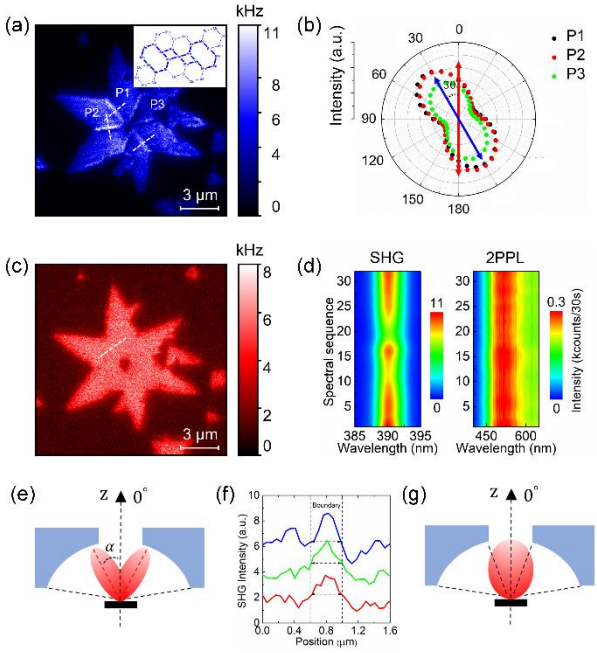

Figure 4.2: Caractérisation des joints de grains et de l'orientation des cristaux dans un flocon de $MoSe_2$ en étoile symétrique à six branches par le signal SHG.

À partir de la Figure 4.2(b), on peut conclure que les orientations cristallines des grains voisins tournent avec un angle relatif dans le plan de $0°$ ou $180°$, ce qui est dû à la perte d'informations de phase dans les mesures SHG. Selon les précédentes études de microscopie électronique à transmission sur fond

noir, le flocon de TMDC en étoile à six branches contient généralement des frontières de miroirs jumeaux. La limite de macle miroir appartient au défaut de ligne impliquant le motif 8-4-4 qui est montré dans l'encart de la Figure 4.2(a), qui est formé par deux grains avec une rotation relative dans le plan de $180°$. En raison de l'interférence destructive des signaux SHG aux limites des macles miroirs, l'intensité SHG est considérablement supprimée aux joints de grains, ce qui est différent de notre observation illustrée à la Figure 4.2(a).

En général, les discontinuités structurelles apparaissent brillantes par microscopie optique linéaire à fond noir (DF), ce qui est dû à la suppression de la lumière diffusée à partir des zones homogènes. Ce n'est que récemment, en utilisant une microscopie DF-SHG, que l'effet de joint de grain brillant sur les flocons de TMDC monocouche a été visualisé. À l'aide d'un modèle à deux dipôles, ils ont souligné que les champs électriques SH déphasés générés à partir des limites du jumeau du miroir peuvent créer une interférence constructive à un grand angle hors plan (par rapport à la normale du plan de l'échantillon), qui peut être détecté par une microscopie DF-SHG. Les émissions SHG des régions homogènes peuvent cependant être bloquées grâce au filtre DF. Ainsi, les joints de grains des TMDC peuvent être visualisés en supprimant les émissions de SHG des régions homogènes. Ici, nous suivons les mêmes considérations pour comprendre notre observation qui est illustrée à la Figure 4.2(a). La Figure 4.2(e) montre le dessin schématique du diagramme de rayonnement SHG à partir des limites du jumeau du miroir. L'angle α permettant une interférence constructive des deux moments dipolaires du rayonnement SH est calculé par: $d \sin \alpha = \lambda/2$, où le λ est la longueur d'onde SHG, le d désigne la distance moyenne entre les deux grains voisins. Dans notre travail, la longueur d'onde SHG λ se situe à 390 nm et la distance d est analysée jusqu'à ~ 400 nm en considérant un profil gaussien comme le montrent les sections efficaces de l'intensité SHG sur la Figure 4.2(f). Ainsi, l'angle α permettant une interférence constructive SHG est estimé à

$\sim 29.5°$. Il se situe dans la plage d'angle de collecte ($\sim 27°$ à $\sim 87°$) du miroir parabolique; par conséquent, le signal SHG généré à partir de la frontière peut toujours être mesuré. D'autre part, étant donné que les moments dipolaires de rayonnement SH dans le plan de l'échantillon sont générés à l'intérieur des grains individuels, la direction de rayonnement SHG à un angle hors plan α de $0°$ ne peut pas être efficacement collectée par le miroir parabolique, qui est en raison de la présence d'une zone de collecte interdite ($0°$ à $\sim 27°$), comme le montre la Figure 4.2(g). Par conséquent, les joints de grains plus brillants peuvent être observés par rapport à ceux à l'intérieur des grains individuels du flocon $MoSe_2$.

5. Propriétés structurales locales à la surface du flocon de $MoSe_2$

La Figure 5.1(a) montre le spectre d'absorption d'un film moléculaire de CuPc de 10 nm qui est déposé sur la surface d'un substrat en verre en utilisant le dépôt thermique en phase vapeur. Le film mince CuPc présente une absorption en bande Q dans le visible de 500 nm à 800 nm. Un pic d'absorption situé à 627 nm et un autre pic d'absorption situé à 696 nm sont respectivement attribués à la deuxième et à la première transition π-π* du macrocycle phtalocyanine. Par conséquent, les mesures Raman sont effectuées par une microscopie optique confocale couplée à un laser CW 636 nm, car la longueur d'onde du laser est en bonne résonance avec l'absorption moléculaire CuPc. Pour sonder les signaux Raman dépendants de la polarisation sur CuPc/$MoSe_2$, des modes laser d'ordre supérieur, à savoir des modes beignets polarisés azimutalement et radialement, sont utilisés. Les Figures 5.1(b) et (c) montrent la distribution calculée de l'intensité du champ électrique dans le plan x-y au foyer de polarisation radiale et azimutale, respectivement. Le faisceau de polarisation radiale focalisé montre principalement la composante $|E_z|^2$, qui est

environ 14 fois plus forte que la composante $|E_{x,y}|^2$. En revanche, la polarisation azimutale dans le foyer n'a que la composante $|E_{x,y}|^2$.

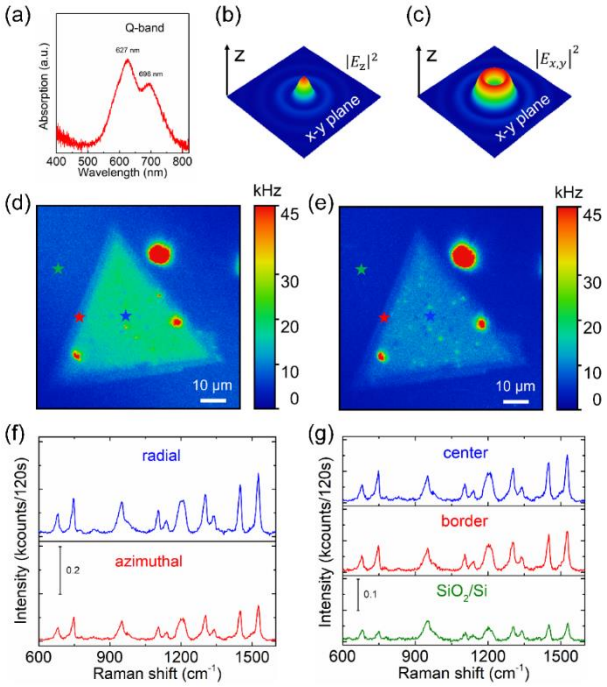

Figure 5.1: Le rehaussement Raman sur le flocon de $MoSe_2$ en forme de triangle.

Les Figures 5.1(d) et (e) montrent les images optiques de CuPc/$MoSe_2$ sous un faisceau laser polarisé radialement et azimutalement, respectivement. Les intensités optiques dans l'image de la Figure 5.1(d) et (e) contiennent le signal PL du flocon $MoSe_2$ et le signal de diffusion Raman des molécules CuPc. Le CuPc / $MoSe_2$ excité sous polarisation radiale donne une intensité optique plus forte que celle sous polarisation azimutale, et l'intensité optique à la frontière du flocon $MoSe_2$ est plus faible que celle au centre du flocon $MoSe_2$. La Figure 5.1(f) montre les spectres Raman qui sont mesurés dans la région centrale de CuPc/$MoSe_2$ sous un faisceau laser polarisé radialement et azimutal. La Figure 5.1(g) illustre les spectres Raman obtenus dans trois régions différentes du substrat CuPc/$MoSe_2$, et les positions exactes marquées par des étoiles bleues, rouges et vertes sont visibles sur les Figures 5.1(d) et (e). Le bruit de fond des

spectres Raman a été soustrait. L'intensité CuPc Raman sous polarisation radiale est plus forte que celle sous polarisation azimutale, comme le montre la Figure 5.1(f). En prenant le mode Raman 1527 cm^{-1} comme exemple, l'intensité Raman intégrée utilisant la polarisation radiale est presque 1.75 fois plus forte que celle utilisant la polarisation azimutale. Comme le montre la Figure 5.1(g), l'intensité Raman intégrée du mode CuPc Raman (1527 cm^{-1}) collectée dans la région centrale de CuPc/$MoSe_2$ est la plus forte, soit près de 3 fois plus élevée que sur le substrat SiO_2/Si. De plus, l'intensité Raman obtenue au centre de CuPc/$MoSe_2$ est légèrement supérieure à celle à la frontière de CuPc/$MoSe_2$.

La Figure 5.2 montre le facteur d'amélioration Raman relatif sur la monocouche $MoSe_2$ sous polarisation radiale et azimutale. Le facteur d'amélioration est calculé en comparant l'intensité Raman (intégration de la surface du pic Raman) de la molécule CuPc dans la région centrale de CuPc/$MoSe_2$ avec celle sur le substrat SiO_2/Si. Les facteurs d'amélioration Raman des différents modes Raman sont différents, allant de 1.1 à 3.5, excités à la fois par la polarisation radiale et azimutale. Bien que l'intensité CuPc Raman à travers une excitation de la polarisation radiale soit plus forte (par exemple, mode Raman à 1527 cml^{-1}) par rapport à celle en utilisant la polarisation azimutale, le facteur d'amélioration de chaque mode Raman sous polarisation azimutale est supérieur à celui sous polarisation radiale.

Comme indiqué dans la littérature précédente, en utilisant le graphène comme plate-forme SERS, les modes Raman à 1342 cm^{-1}, 1452 cm^{-1} et 1531 cm^{-1} de la monocouche CuPc ont le plus grand facteur d'amélioration Raman par rapport aux autres modes Raman, ce qui est dû au processus de transfert de charge prononcé entre la molécule de CuPc et le graphène. D'autre part, les modes Raman situés à 749 cm^{-1} et 1143 cm^{-1} de la molécule CuPc sont considérablement améliorés en utilisant le nitrure de bore hexagonal (h-BN) comme substrat, qui bénéficie de ces modes Raman montrant de grands

dipôles, conduisant en outre à une interaction dipôle-dipôle efficace avec le substrat h-BN. Ici, dans notre travail, les modes CuPc Raman de 746 cm^{-1}, 1138 cm^{-1}, 1339 cm^{-1}, 1449 cm^{-1} et 1527 cm^{-1} sur la monocouche $MoSe_2$ sont tous améliorés par rapport à ceux sur le substrat SiO_2/Si, et la monocouche $MoSe_2$ est un semi-conducteur à bande interdite directe et possède une liaison covalente polaire (Mo-Se). Par conséquent, le processus de transfert de charge et l'interaction dipôle-dipôle dans l'hétérostructure CuPc/$MoSe_2$ peuvent éventuellement se produire.

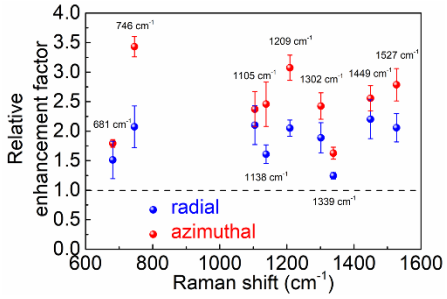

Figure 5.2: La comparaison du facteur d'amélioration Raman relatif sur une monocouche de $MoSe_2$ sous un mode laser polarisé radialement et azimutalement.

De plus, ces interactions sur l'hétérostructure CuPc/$MoSe_2$ peuvent être plus efficaces lorsque la composante $|E_{x,y}|^2$ de la polarisation azimutale est utilisée. Pour expliquer ce résultat, l'orientation moléculaire de CuPc à la surface de $MoSe_2$ sera considérée. La molécule CuPc qui est déposée à la surface de MoS_2 par dépôt thermique en phase vapeur montre une orientation de face, car le centre métallique Cu pourrait se lier à l'atome de soufre de MoS_2 via une coordination axiale. Nous attribuons l'amélioration élevée du SERS avec la polarisation azimutale à l'effet de première couche, où le processus de transfert de charge peut être plus prononcé entre la molécule de CuPc orientée face à la première couche et la surface $MoSe_2$. Au fur et à mesure que l'épaisseur de la couche de CuPc augmente, l'orientation moléculaire de CuPc peut changer, comme la molécule de CuPc montrant un angle d'inclinaison par rapport à la

surface de l'échantillon. Une telle évolution de l'orientation moléculaire de CuPc est observée dans le film mince de phtalocyanine de fer (FePc) déposé sur une surface cristalline de MoS_2, où la molécule de FePc repose principalement sur la surface de MoS_2 et avec l'augmentation de l'épaisseur du film (plus de 4.5 nm), le FePc les molécules adoptent un petit angle d'inclinaison par rapport au plan de l'échantillon. Ici, dans cette étude, les molécules de CuPc donnent une intensité Raman plus élevée sous polarisation radiale que sous polarisation azimutale, car les molécules de CuPc inclinées sont excitées sous polarisation radiale, où elles montrent principalement la composante $|E_z|^2$ dans le foyer laser.

Les spectres optiques 16 × 16 de la région correspondante de CuPc/$MoSe_2$ sont réalisés en utilisant la technique de cartographie hyperspectrale. Les Figures 5.3(a) et (b) montrent les cartographies d'intensités optiques intégrées spectralement de 750 nm à 850 nm et la zone de pic CuPc Raman à 1527 cm^{-1}, respectivement. Trois régions à la frontière (R1), la frontière au centre (R2) et le centre (R3) sont marquées par les cercles noirs en pointillés illustrés à la Figure 5.3(a) et (b). De plus, une série de spectres optiques PL et Raman sont obtenus à partir des trois régions (R1, R2 et R3) représentées sur la Figure 5.3(c) et (d), respectivement. On observe que l'intensité PL augmente progressivement de la région R1 à R3 sur la Figure 5.3(a) et (c). De plus, un décalage vers le rouge de 3 à 6 nm de la position du pic de photoluminescence de la région R2 est observable par rapport à celui des régions R1 et R3. D'autre part, l'intensité Raman de la région R2 est plus forte que celle des régions R1 et R3 sur la Figure 5.3(b) et (d). Sur la base des résultats ci-dessus, nous démontrons que l'intensité SHG, l'intensité de la photoluminescence et la position du pic, ainsi que l'amélioration Raman sont sensibles aux propriétés de la structure locale du flocon $MoSe_2$.

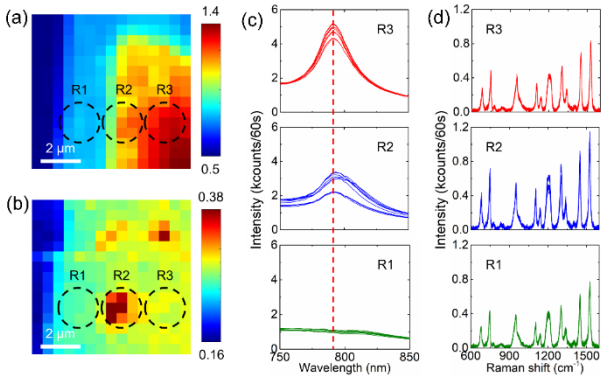

Figure 5.3: Amélioration Raman liée à la structure locale sur un éclat de $MoSe_2$.

6. Émission directionnelle dans un film mince moléculaire DH-P-TTA

La Figure 6.1(a) montre l'image optique non linéaire d'un film mince DH-P-TTA qui contient deux domaines individuels. Les mesures AFM sont également réalisées pour comparer leurs épaisseurs. Les résultats montrent que le domaine supérieur a une épaisseur d'environ ~5.22 nm et que le domaine inférieur a une épaisseur d'environ ~6.47 nm. Les réponses spectrales de ces deux domaines sont sondées, comme le montre la Figure 6.1(b). Pour chaque domaine, cinq spectres optiques 2PPL sont collectés à différentes positions (a1-5 et b1-5). Nous observons deux maxima de pic 2PPL pour tous les spectres et aucun changement de la position du pic 2PPL dans un domaine. Cependant, un décalage du pic 2 est observé lorsque l'on compare les spectres pris dans les domaines supérieur et inférieur. La position maximale du pic 2 mesurée à partir du domaine inférieur est décalée vers une longueur d'onde supérieure de ~ 552 nm par rapport à celle obtenue à partir du domaine supérieur (pic maximum à ~ 544 nm), alors qu'aucun décalage de la position maximale du pic 1 n'est observé. Le décalage vers le rouge du pic 2PPL est peut-être attribué au comportement d'empilement moléculaire différent (par exemple, l'orientation et l'ordre) dans le film mince DH-P-TTA. Pour traiter ce phénomène, les diagrammes d'émission angulaire des deux domaines sont

mesurés et les résultats expérimentaux sont présentés sur la Figure 6.2.

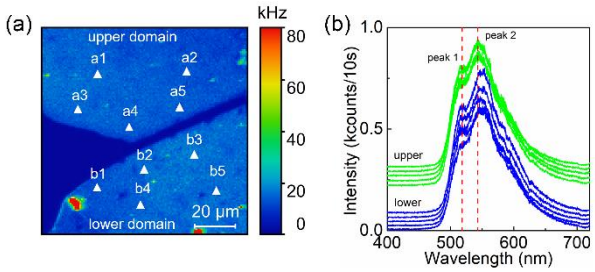

Figure 6.1: Caractérisation optique non linéaire du film mince DH-P-TTA.

Pour chaque domaine, nous mesurons cinq diagrammes d'émission à différentes positions (a1-5 et b1-5). Pour comparer précisément la différence de directionnalité d'émission, l'intensité optique en fonction de l'angle dans le plan ϕ_{em} et de l'angle hors du plan θ_{em} est également tracée sur la Figure 6.2(a) et (b). Comme le montre la Figure 6.2(a), aucune différence significative dans la distribution de l'intensité optique dans les cinq modèles d'émission expérimentaux n'est visible. La même observation est également montrée dans le domaine inférieur de la Figure 6.2(b). Fait intéressant, les diagrammes d'émission obtenus à partir des deux domaines semblent se refléter lorsque l'on compare les domaines supérieur et inférieur. En détail, pour l'angle dans le plan ϕ_{em}, le signal optique issu du domaine supérieur pointe vers la gauche à $\phi_{em} = 200°$; tandis que le signal optique prélevé dans le domaine inférieur émet vers la droite à $\phi_{em} = 345°$. Pour l'angle hors plan θ_{em}, une direction d'émission proéminente à $|\theta_{em}| = \sim 36°$ du domaine supérieur sont observés, qui apparaissent à $|\theta_{em}| = \sim 42°$ du domaine inférieur. Les propriétés de directionnalité distinctes entre les deux domaines séparés du film mince DH-P-TTA indiquent l'orientation moléculaire différente dans la structure cristalline.

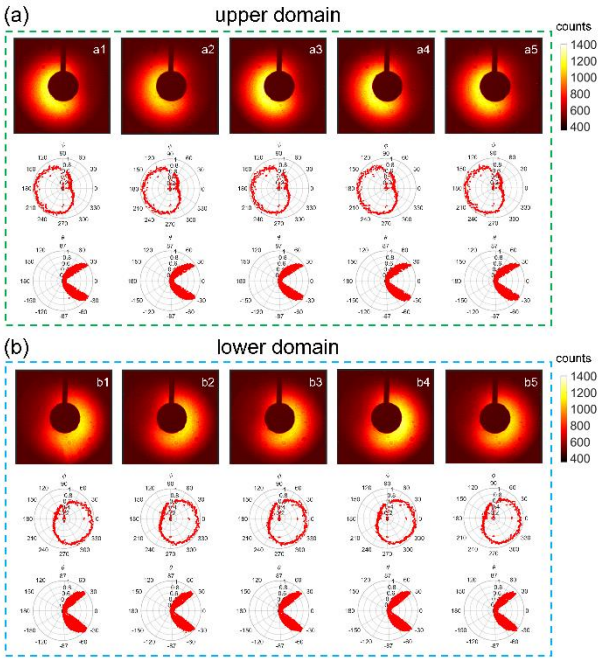

Figure 6.2: Le comportement de directivité obtenu à partir de deux domaines individuels du film DH-P-TTA.

Les dessins schématiques pour ajuster l'orientation dans le plan (illustrée par la ‘vue de dessus’) et l'orientation hors du plan (illustrée par la ‘vue latérale’) du substrat de l'échantillon sont illustrés à la Figure 6.3. Les deux domaines DH-P-TTA sont représentés en bleu et les sens de rotation du substrat sont indiqués par les flèches vertes. Après une rotation dans le plan du substrat de l'échantillon, les diagrammes d'émission angulaires et les tracés polaires correspondants (intensité optique en fonction de l'angle dans le plan ϕ_{em}) des domaines supérieur et inférieur sont présentés sur la Figure 6.3(a). Les signaux optiques des domaines supérieur et inférieur émettent à des angles dans le plan à $\phi_{em} = 150°$ et à $\phi_{em} = 300°$, respectivement. En comparant avec les résultats de la Figure 6.2, nous concluons que le substrat de l'échantillon est tourné approximativement d'un angle dans le plan de $50°$. De plus, nous inclinons le substrat de l'échantillon avec un certain angle hors du plan par rapport à l'axe optique (représenté par l'axe z) et les modèles d'émission résultants des deux domaines sont affichés sur la Figure 6.3(b). On observe la direction d'émission depuis le domaine supérieur à l'angle hors plan $|\theta_{em}| <$

36°. Cependant, nous ne pouvons pas estimer la direction exacte en raison de la présence d'une région de collecte interdite (-27 degrés à 27 degrés) dans le miroir parabolique. De plus, le domaine inférieur présente une direction d'émission à $|\theta_{em}| = \sim 50°$, plus grand que l'angle hors plan $|\theta_{em}| = \sim 42°|$ montré sur la Figure 6.2(a), suggérant clairement les influences de l'échantillon incliné sur la direction d'émission. En résumé, la Figure 6.2 et la Figure 6.3 démontrent que la directionnalité d'émission du film mince DH-P-TTA est fortement liée à l'orientation moléculaire, qui est en outre prouvée en modifiant l'orientation de l'échantillon.

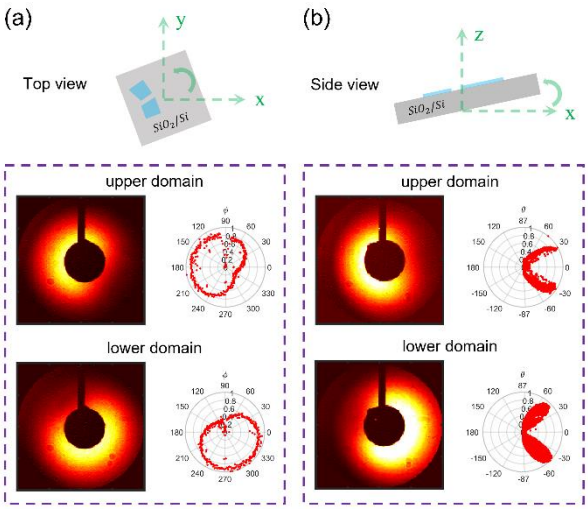

Figure 6.3: La directionnalité d'émission du film mince DH-P-TTA à différentes orientations de substrat.

Les images optiques non linéaires de trois régions du film DH-P-TTA sont présentées sur la Figure 6.4. Les carrés blancs en pointillés R1, R2 et R3 marqués sur la Figure 6.4(a)-(c) représentent les trois domaines d'épaisseurs différentes. D'après les mesures AFM, l'épaisseur de couche de R1, R2 et R3 est d'environ ~0.87 nm, d'environ ~33.0 nm et d'environ ~58.18 nm, respectivement. La Figure 6.4(d) montre les réponses spectrales enregistrées à partir de R1, R2 et R3. Deux pics 2PPL sont observables à partir des trois domaines. La moyenne des intensités 2PPL intégrées spectralement de 450 nm à 700 nm pour trois domaines est illustrée à la Figure 6.4(e). L'intensité la

plus forte apparaît dans le domaine R3 et la plus faible dans le domaine R1, indiquant une intensité 2PPL claire en fonction de l'épaisseur du film.

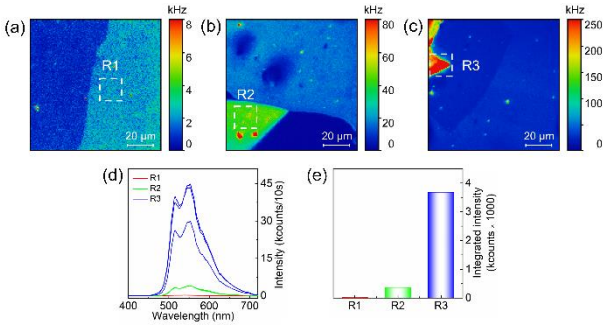

Figure 6.4: Dépendance à l'épaisseur des signaux 2PPL du film mince DH-P-TTA.

Les Figures 6.5(a), (b) et (c) montrent les diagrammes d'émission angulaires ainsi que les tracés polaires correspondants (intensité 2PPL en fonction de l'angle dans le plan ϕ_{em} et en fonction de l'angle hors du plan θ_{em}), qui sont mesurés à partir des domaines R1, R2 et R3. Dans le domaine R1 qui a une épaisseur d'environ ~0.87 nm, l'intensité 2PPL se répartit principalement sur le côté gauche du diagramme d'émission, comme le montre la Figure 6.5(a). Ce modèle est similaire à la direction d'émission des domaines avec une épaisseur allant de ~5 nm à ~10 nm. A partir des tracés polaires correspondants en fonction de l'angle dans le plan ϕ_{em} et de l'angle hors du plan θ_{em}, on peut voir que la direction d'émission pointe vers $\phi_{em} = 180°$ et $|\theta_{em}| = \sim 36°$. En revanche, avec l'augmentation de l'épaisseur de la couche comme dans les domaines R2 et R3, les diagrammes angulaires d'émission sont presque isotropes. Considérant maintenant l'angle hors du plan θ_{em}, nous trouvons que le domaine R2 présente une direction d'émission à $|\theta_{em}| = \sim 45°$. Par rapport au domaine R2, l'émission du domaine plus épais R3 pointe vers un angle allant jusqu'à $|\theta_{em}| = \sim 55°$, ce qui est nettement différent de l'angle d'émission hors du plan ($|\theta_{em}| = \sim 36°$) observé dans le domaine ultrafin R1. Les données observées démontrent évidemment que les propriétés de rayonnement angulaire sont fortement corrélées à l'épaisseur du film DH-P-TTA.

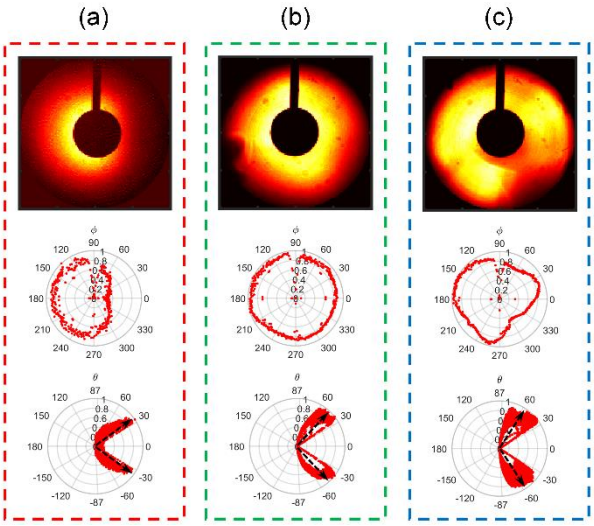

Figure 6.5: La dépendance à l'épaisseur de la directionnalité des émissions.

7. Sommaire

La dépendance des propriétés structurelles des propriétés optiques linéaires et non linéaires des couches semi-conductrices bidimensionnelles est systématiquement étudiée dans cette thèse. Les matériaux stratifiés étudiés dans la thèse contiennent des flocons de TMDCs et des couches minces organiques. La microscopie optique confocale à balayage maison assistée par un miroir parabolique est utilisée pour effectuer toutes les caractérisations optiques. Au cours de mes travaux de thèse, la microscopie optique confocale à balayage combinée à un laser pulsé femtoseconde a été reconstruite, corrigée et également développée. Les nouvelles fonctions, telles que l'imagerie SHG, l'imagerie 2PPL, l'imagerie du motif radiatif angulaire et la dépendance angulaire des signaux SHG et 2PPL, sont mises en œuvre. La microcopie confocale développée nous permet de déterminer les irrégularités structurelles, la symétrie structurelle et l'orientation cristalline ainsi que l'orientation moléculaire des matériaux optiques.

Abstrakt

Optische Charakterisierungstechniken als ultraempfindliche und zerstörungsfreie Werkzeuge, die den Einfluss der lokalen Struktur auf die optischen Eigenschaften von zweidimensionalen Halbleiterschichten aufzeigen, haben große Aufmerksamkeit erregt. In dieser Arbeit wird nichtlineare optische Mikroskopie in Kombination mit Raman-Mikroskopie verwendet, um die strukturellen Eigenschaften wie etwa strukturelle Unregelmäßigkeiten, kristalline Orientierung, strukturelle Symmetrie sowie molekulare Orientierung von Schichtmaterialien zu charakterisieren und zu verstehen.

Zunächst wird durch die Verwendung von konfokaler Rastermikroskopie in Verbindung mit einem gepulsten Femtosekundenlaser eine effiziente Emission der ersten Oberschwingung (SHG) an den Kanten einzelner Schichten von Wolframdisulfid-Flocken (WS_2) deutlich beobachtet, was auf das Vorhandensein von gebrochener Translationssymmetrie und mehr Strukturfehlern an den Rändern zurückzuführen ist. Interessanterweise zeigt sich die durch zwei Photonen induzierte Photolumineszenz (2PPL) bei Raumtemperatur an den Flockenrändern am schwächsten, was eine Antikorrelation mit dem SHG-Signal in der Einzelschicht von WS_2 aufweist. Die erhaltenen Ergebnisse sind wahrscheinlich auf das Vorhandensein elektronischer Zustände als Zwischenniveaus in der Bandlücke zwischen den Valenz- und Leitungsbändern an den Flockenrändern zurückzuführen. Außerdem nimmt die SHG-Intensität mit zunehmender Schichtdicke zu, während das optische 2PPL-Signal nur in der Einzelschicht von WS_2 sichtbar ist. Das polarisationsabhängige SHG-Signal zeigt ein sechsfaches Rotationsmuster, was auf die dreifache Rotationssymmetrie der WS_2-Flocke hinweist.

Anschließend werden die strukturellen Unregelmäßigkeitseigenschaften von atomar dünnen Molybdändiselenid ($MoSe_2$)-Flocken durch SHG- und 2PPL-Signale weiter untersucht. Die 2PPL-Peaks bei ~2,30 eV und ~2,38 eV konnten den A'-Exziton- bzw. B'-Exziton-Übergängen der $MoSe_2$-Flocke zugeordnet werden. Die Kristallorientierungen von diskreten $MoSe_2$-Flocken werden mit der polarisierten SHG-Bildgebung und der winkelabhängigen SHG-Spektroskopie bestimmt. Wir beobachteten die Unterschiede im Winkel 3θ, der als Winkel zwischen dem erzeugten elektrischen SHG-Feld und dem elektrischen Feld des Lasers definiert ist, was experimentell die unterschiedlichen Kristallorientierungen diskreter $MoSe_2$-Flocken anzeigt. Darüber hinaus ist das starke SHG-Signal an den Korngrenzen und Kanten innerhalb einer einzelnen $MoSe_2$-Flocke deutlich sichtbar.

Die Verwendung von konfokaler Mikroskopie in Kombination mit Lasermoden höherer Ordnung zur Raman-Verstärkung auf $MoSe_2$-Flocken durch Verwendung von Kupferphthalocyanin (CuPc)-Molekülen als Raman-aktive Substanz wird demonstriert. Sowohl die Photolumineszenz- als auch die SHG-Spektroskopie werden verwendet, um die lokalen strukturellen Eigenschaften der $MoSe_2$-Flocke aufzudecken. Die Raman-Verstärkung auf einer $MoSe_2$-Einzelschicht bei einer azimutal polarisierten Anregung ist größer als die Verstärkung bei einer radial polarisierten Anregung. Dieses Ergebnis weist darauf hin, dass die face-on-orientierten CuPc-Moleküle durch den Ladungstransfer im Grundzustand und die Dipol-Dipol-Wechselwirkung stark mit der $MoSe_2$-Einzelschicht wechselwirken können. Darüber hinaus zeigen die Raman-Streuungskarten auf der unregelmäßigen $MoSe_2$-Oberfläche eine gute Korrelation mit den SHG- und PL-Bildern, was auf die Beziehung zwischen lokaler Struktur und optischen Eigenschaften der $MoSe_2$-Flocke hindeutet.

Schließlich wird eine k-Raum-Bildgebungsmikroskopie zum Untersuchen der Winkelemissionsmuster basierend auf der konfokalen Mikroskopie

implementiert, die mit einem gepulsten Femtosekundenlaser gekoppelt ist. Die Probenort- und Dickenabhängigkeiten der Emissionsmuster von 2PPL-Signalen, die von einem einkristallinen DH-P-TTA-Molekülfilm ausgehen, werden demonstriert. In Kombination mit berechneten Emissionsmustern wurde die mögliche molekulare Orientierung innerhalb des DH-P-TTA-Films diskutiert. Auf dem Film werden zwei 2PPL-Peakmaxima unterschieden, die bei ~516 nm und ~552 nm liegen. Wir beobachten das anisotrope Emissionsmuster auf dem ultradünnen Film, was darauf hindeutet, dass die Moleküle einen Neigungswinkel einnehmen und innerhalb einer Domäne einen hohen Ordnungsgrad aufweisen. Darüber hinaus wird auch eine starke Korrelation zwischen dem erzeugten 2PPL-Signal und der Schichtdicke des DH-P-TTA-Films demonstriert. Die nahezu isotropen Strahlungsmuster werden auf den dicken Filmen mit einer Dicke von ~33.0 nm und ~58.18 nm sichtbar gemacht, was auf die vertikale Ausrichtung der DH-P-TTA-Moleküle in den Filmen zurückzuführen ist.

Acknowledgements

I am sincerely grateful to Prof. Dr. Pierre-Michel Adam and PD. Dr. Dai Zhang for the supervision of my doctoral thesis and the opportunity to work in nano-optics field.

I am thankful to Prof. Dr. Alfred J. Meixner for providing the access to his lab and the amazing facilities. I sincerely thank Dr. Anke Horneber for the excellent guidance in optical microscopy. I am thankful to all of the collaborators for the fantastic materials.

I am sincerely thankful to all of my colleagues in Tübingen and in Troyes. I thank my colleagues Dr. Quan Liu, Dr. Yu-Ting Chen, Dr. Peng Miao, Achim Junginger, and Dr. Kai Braun for the introduction of relevant techniques. I am also thankful for the professional guidance from many engineers like Dr. Sergei Kostcheev, Dr. Jérémie Beal, and Dr. Ronny Loeffler.

I sincerely acknowledge the financial support by China Scholarship Council for my doctoral study. I am thankful for the financial support by Franco-German University.

Finally, I would like to thank my family and my partner Xuexue for their support, encouragement, and love.

Université franco-allemande
Deutsch-Französische Hochschule

https://www.dfh-ufa.org/en/

国家留学基金管理委员会 CHINA SCHOLARSHIP COUNCIL

https://www.csc.edu.cn